

**DEVELOPMENT OF TIME DOMAIN CHARACTERIZATION METHODS
FOR PACKAGING STRUCTURES**

A Thesis
Presented to
The Academic Faculty
by
Sreemala Pannala

In Partial Fulfillment
of the Requirements for the Degree
Doctor of Philosophy in Electrical Engineering

Georgia Institute of Technology
August, 1999

Copyright © 1999 by Sreemala Pannala

Dedicated to
my mother Chandrakala, my father Narayan Reddy
and
my brothers Sreedhar and Sreekanth
for their constant support and encouragement

ACKNOWLEDGMENTS

I would like to thank several people who helped me to complete this thesis. Dr. Madhavan Swaminathan was very enthusiastic about this research project, and allowed me to work on "real world" problems. My sincere thanks for all the guidance he has provided me over the course of my study. Dr. Andrew Peterson, Dr. Mark Allen, Dr. David Keezer, Dr. Michael Young, and Dr. Dave Hertling, who served on my various committees provided invaluable suggestions and recommendations which gave me new perspectives on my research.

Anand, Christine, Jaya, Josh, Anisha, Rajgopal, Alberto, Kwang, Nanju, Sungjun - members of High Performance Package Design Lab of the Packaging Research Center (PRC) at Georgia Tech, who worked with me on various projects and made my work days interesting. Manoj Nachanani, Manager, National Semiconductor gave me a glimpse of what it would be like to work in industry, by giving me an opportunity to work on package characterization on a summer internship. Special thanks to the faculty and students of the PRC for introducing me to the wonderful area of electronic packaging and to PRC for supporting my research.

My family has been a constant source of support and encouragement. Special thanks to Sreekanth, my brother, who was with me every step of this journey and made my stay at Georgia Tech comfortable. Last but not the least, I would like to thank all my friends who have helped me at various stages. I will remember times spent with them fondly.

TABLE OF CONTENTS

ACKNOWLEDGMENTS	iii
TABLE OF CONTENTS	iv
LIST OF TABLES	vii
LIST OF ILLUSTRATIONS	ix
SUMMARY	xiv
I Introduction	1
1.1 Time Domain Measurements	2
1.2 Need for Extracting Models from Time Domain Measurements	3
1.3 Measurement System	5
1.4 Limitations of TDR/TDT Measurements	7
1.5 Advantages and Disadvantages of TDNA	10
1.6 Review of Time Domain Characterization Methods	10
1.6.1 Short Pulse Technique	12
1.6.2 Dynamic Deconvolution Procedure	13
1.6.3 Frequency Domain Mapping Method	16
1.6.4 Exponential Approximation	18
1.6.5 Model Optimization	19
1.7 Problem Statement	21
1.8 Dissertation Outline	23
II Lumped Equivalent Circuit Modeling	25
2.1 Extraction of Electrical Parameters	29
2.1.1 Bare Board Measurement	30
2.1.2 Stand-alone Measurement	30
2.1.3 Even Mode Excitation	31
2.1.4 Odd Mode Excitation	32
2.2 Board Design	33
2.3 Test Vehicle	35
2.4 Measurements	36
2.4.1 Validity of Lumped Element Model for the Connector	39

2.4.2	Equivalent Model of the Connector Pins	40
2.5	Model Validation Using Crosstalk	47
III	Characterization of RF Packages Using Open-Short Calibration	52
3.1	Time Reference	53
3.2	Package Measurements	54
3.2.1	Time Window	57
3.2.2	Calculation of Self Inductance Value	57
3.2.3	Calculation of Self Capacitance Value	59
3.2.4	Extension to Distributed Equivalent Circuits	60
3.3	Extracted L, C Values	61
IV	Extraction of Broad Band Rational Function Models from Transient Data	65
4.1	Available Pole-Residue Extraction Methods from Transient Data	66
4.2	Extraction of Poles	68
4.3	Deconvolution of Input Waveform - Extraction of Device Residues	70
4.4	Extraction of Poles and Residues from Simulated TDT/TDR Data	73
4.5	Sensitivity of the Method to Noise	84
V	Extraction of Rational Functions from TDR/TDT Measurements	89
5.1	Measurement Set-up	90
5.2	Rise Time Measurement	91
5.3	Timing Reference Measurement	92
5.4	TDT Measurement	94
5.4.1	Measurements for S_{21} Model	94
5.4.2	Measurements for S_{12} Model	96
5.5	TDR Measurements for S_{11} & S_{22} Model	96
5.6	Extraction of Poles	98
5.7	Extraction of Residues	101
5.8	Extracted Rational Functions	103
5.9	Extracted Frequency Response vs Network Analyzer Measurements	105
5.10	Reconstruction in Time	110
5.11	Calculation of Error	111
VI	Measurement Parameters	115
6.1	Number of Data Points Required	116
6.2	Sampling Interval	117
6.3	Time Window	123

VII Error Sources	128
7.1 Random and Drift Errors	128
7.2 Error Limits	129
7.2.1 Vertical Noise	130
7.2.2 Timing Jitter	134
7.3 Systematic Errors	138
7.4 Equipment Specifications and Related Limitations	138
VIII Rational Function Models for Lossy Thin Film Planes	140
8.1 Pulse Propagation on a Low Impedance Thin Film Plane Structure	141
8.2 Extraction of Rational Function Model	146
8.3 Rational Function Model vs. Π Model for the Thin Film Plane	150
8.4 Measurement to SONNET Based Modeling Correlation	152
8.4.1 Analysis Using the System Poles and Residues	158
IX Conclusions	163
9.1 Application of the Rational Function Method	164
9.2 Future Work	168
REFERENCES	170
VITA	177

LIST OF TABLES

2.1 Connector Parameters	42
2.2 Comparison of Peak Near End and Far End Noise	51
3.1 L, C Values for PQFP_48	62
3.2 L, C Values for SOP_20	62
3.3 L, C Values for PQFP_80	63
3.4 L, C Values for MDIP_24	63
3.5 L, C Values for SSOP_56	64
4.1 Poles and Residues of the Original Macromodel	75
4.2 Singular Values of the D Matrix	78
4.3 Extracted Poles and Residues from Simulated TDT Data	80
4.4 Effect of White Noise	87
5.1 Reflection Coefficient at the Falling Edge	93
5.2 Extraction Procedure Parameters	99
5.3 Poles and Residues of the Extracted S_{21} Model from TDT Measurement	104
6.1 Error Due to Resolution Calculated for S_{21}	119
6.2 Error Due to Resolution Calculated for S_{11}	119
6.3 Extracted Frequency Components	122
6.4 Error Due to Window Length Calculated for S_{21}	125
6.5 Error Due to Window Length Calculated for S_{11}	125

7.1 Error Due to Averaging	134
7.2 Error Due to Jitter - Different Reference Waveforms	137
7.3 Error Due to Jitter - Same Reference Waveform	137
8.1 Poles and Residues Extracted for the Thin Film Plane	148
8.2 Resonant Frequencies for the Various Test Cases	158
9.1 Comparison of Time Domain Characterization Methods	166

LIST OF ILLUSTRATIONS

1.1	Flow Chart for Circuit Modeling of Components, Interconnections, and Packages	5
1.2	Experimental System for Transient Measurements	6
1.3	Interconnect Structures - Transmission Lines, Bends, Steps, Vias, and Pads	12
1.4	(a) Scattering Parameters of a Two-port Device	14
	(b) Cascaded Piecewise Uniform Transmission Lines	14
2.1	Connector Pins	28
2.2	Even Mode Excitation	31
2.3	Odd Mode Excitation	32
2.4	Schematic of the Measurement Set-up	34
2.5	PCB Cross Section	34
2.6	Top View of the Male Card (CAD Drawing)	35
2.7	Signal and Ground Assignments	36
2.8	Measurement Set-up	37
2.9	TDR Measurement of the Connector Pin	38
2.10	Equivalent Circuit for the Bare Board	41
2.11	(a) Measurement to Simulation Correlation of Pin 1	43
	(b) Equivalent Circuit for Pin 1	43

2.12	(a) Measurement to Simulation Correlation of Pin 2	44
	(b) Equivalent Circuit for Pin 2	44
2.13	(a) Response Due to Even Mode Excitation	45
	(b) Equivalent Circuit with M_{12}	45
2.14	(a) Response Due to Odd Mode Excitation Measured on Pin 1	46
	(b) Equivalent Circuit with C_{12}	46
2.15	Near End Crosstalk for the Pin Configuration in Figure 2.7 (a)	47
2.16	Far End Crosstalk for the Pin Configuration in Figure 2.7 (a)	48
3.1	RF-IC Packages Characterized	55
3.2	Block Diagram of Measurement Set-up	56
3.3	The Fixture Used and the Digital Sampling Oscilloscope	56
3.4	Equivalent Circuit for the Stand-alone Pins	58
3.5	(a) Reference Short Measurement	59
	(b) Measurement vs. Simulation of the Reference Short	59
	(c) Reference Short Measurement Compared to the Shorted Pin	59
	(d) Measurement vs. Simulation of the Pin Response	59
3.6	(a) Reference Open Measurement Compared to the Open Ended Pin	60
	(b) Measurement vs. Simulation	60
3.7	Pins Represented by Transmission Lines	61
4.1	Top View and the Layer Information of the PCB Plane Structure	74
4.2	Device and Reference Waveform Used for Extracting S_{21} Model	77
4.3	Comparison of Reconstructed and Actual S_{21} (a) Magnitude (b) Phase	81

4.4	Device and Reference Waveform used for Extracting S_{11} Model	82
4.5	Comparison of Reconstructed and Actual S_{11} Magnitude	83
4.6	Comparison of Reconstructed and Actual S_{11} Phase	84
4.7	Error Due to White Noise	88
5.1	The Fabricated Test Vehicle	90
5.2	Measurement Set-up for S_{21} Device Measurement	91
5.3	Rise Time Determination Using a Short Standard Measurement	92
5.4	Short Standard Measurement	93
5.5	Device Response (Output) and the Reference Waveform (Input) Used for Extracting S_{21} Model	95
5.6	Device Response (Output) and the Reference Waveform (Input) Used for Extracting S_{11} Model	98
5.7	S_{21} Response due to Different Orders of the Rational Function Model (a) Magnitude (b) Phase	100
5.8	S_{21} Response for Different Cut-off Values for the Residues (a) Magnitude (b) Phase	102
5.9	Comparison of Reconstructed S_{21} Rational Function Model Response with Network Analyzer Measurement (a) Magnitude (b) Phase	106
5.10	Comparison of Reconstructed S_{11} Rational Function Model Response with Network Analyzer Measurement (a) Magnitude (b) Phase	107
5.11	Comparison of Reconstructed S_{12} Rational Function Model Response with Network Analyzer Measurement (a) Magnitude (b) Phase	108
5.12	Comparison of Reconstructed S_{22} Rational Function Model Response with Network Analyzer Measurement (a) Magnitude (b) Phase	109
5.13	Reconstructed TDT Response and the Actual Response	110
5.14	Reconstructed TDR Response and the Actual Response	111

5.15	Comparison of S_{21} Magnitude from Simulation and Measurements	113
5.16	Comparison of S_{21} Phase from Simulation and Measurements	114
6.1	Effect of Resolution on S_{21} (a) Magnitude (b) Phase	120
6.2	Effect of Resolution on S_{11} (a) Magnitude (b) Phase	121
6.3	Effect of Time Window on S_{21} (a) Magnitude (b) Phase	126
6.4	Effect of Time Window on S_{11} (a) Magnitude (b) Phase	127
7.1	Effect of Averaging	131
7.2	Effect of Averaging (a) S_{21} Magnitude (b) S_{21} Phase	133
7.3	Effect of Jitter on Time Reference Waveform	135
7.4	Effect of Jitter (a) S_{21} Magnitude (b) S_{21} Phase	136
8.1	Physical Dimensions and Cross Section of the Thin Film Plane	141
8.2	1 cm x 1 cm Fabricated Meshed Plane Structure	142
8.3	Measurement Using Probes	142
8.4	Block Diagram of TDR/TDT Measurement Set-up	144
8.5	TDR Response	144
8.6	TDT Response	145
8.7	Initial Transient Waveform	145
8.8	The Device and the Reference Waveform	146
8.9	The S_{21} Rational Function Model Response Compared with Network Analyzer Measurements and SONNET Simulation (a) Magnitude (b) Phase	149
8.10	Π Model	151
8.11	Steady State Waveform	151

8.12	Initial Transient	152
8.13	S_{21} Macromodel Comparison with SONNET Simulation (a) Magnitude (b) Phase	155
8.14	TDT Measurement and Simulation Comparison of the Transient Response for the Diagonal Port Location	156
8.15	TDT Measurement and Simulation Comparison of the Transient Response for the Edge Port Location	157
8.16	Simulation of Ground Bounce for Lossless Test Case Compared with Lossy Test Cases	162
9.1	Methodology for Parametric Fault Diagnosis	169

SUMMARY

Packaging structures at the various levels of a system are characterized using software tools and/or network analyzer measurements. With the increasing clock frequencies for digital systems and the evolving trend towards mixed signal packages, time domain characterization methods and the development of models using time domain measurements are becoming increasingly useful. The measurements and analysis depend on the type and size of the structure, the frequency bandwidth, and the type of calibration required. The purpose of this research was to develop accurate characterization methods for packaging structures using Time Domain Reflectometry (TDR) and Time Domain Transmission (TDT) measurements. Two categories of models, namely the low frequency, narrow bandwidth lumped element models and high frequency, large bandwidth rational function models have been studied. These models are SPICE compatible and can be used in a transient simulation.

A systematic procedure for extracting equivalent circuits for a coupled line system directly from the transient response has been developed. This requires a careful construction of the fixture on which the Device Under Test (DUT) is mounted and the design of suitable calibrating structures. Since error correction is difficult in the time domain, the measured transient response is often calibrated in the frequency domain which requires short, open, through and load standards. After calibration, the corrected

frequency domain response is reconverted to the time domain. However, it is not always possible to have these standards. The proposed method does not require the time-frequency-time translation and uses only open and short standards to develop low frequency models. The error associated with this approximation has been quantified. This type of characterization is suitable for intrasystem connectors, short interconnects such as vias and RF leaded frame packages.

Rational function models compatible with a circuit simulator such as SPICE are developed using the system poles and residues. The extraction algorithm uses a novel method for deconvolution and this is possible because of the rational function representation of the model. These models capture the broad-band frequency response of the DUT and have been used for both low loss and lossy plane structures. The effect of resolution, time window, jitter and noise on the models has been studied.

Ground bounce was captured on thin film plane structures and broad band models were developed using the measured transient response. The ground bounce is caused by the resonances in the structure. Due to the lossy behavior, a small time window is available to capture the response. This problem is enhanced due to the very small amplitude of the transient response which requires a major modification in the conventional TDR/TDT setup. A measurement set-up for characterizing the contribution of resonance to ground bounce on lossy thin film planes has been developed. The rational function models developed from the measured transient response are accurate and include the effect of loss in the structure. The ground bounce has been analyzed using macromodels and compared against the response for typical PCB planes.

CHAPTER I

INTRODUCTION

Accurate characterization of packaging structures such as interconnects, coupled lines, connectors, RF packages, planes, integrated passive devices, etc., is essential for successful high performance system design. The values of the manufactured components vary considerably with the processing parameters and the materials used, therefore, analytical expressions and simple models may not be accurate enough to satisfy the design requirements. Consequently, the characterization and modeling of these structures through precise experimental techniques is a viable option.

Microwave measurement techniques for component characterization and modeling can be categorized as Frequency Domain Measurement Techniques (FDMT) and Time Domain Measurement Techniques (TDMT). Frequency domain measurement techniques allow for a full and accurate characterization of microelectronic devices and interconnections in terms of scattering parameters. A conventional implementation, the Frequency Domain Network Analyzer (FDNA), uses a swept frequency source and a set of phase sensitive receivers. Ordinarily these measurements cannot be localized to the network under test, but give global information about the network including the connecting cables and the adaptors. Various calibration techniques are then applied to

extract the device characteristics. The instrumentation is expensive and typically limited to two test ports. In FDNA, error correction is essential and automatic. Computer controlled calibration and data processing are recognized as mandatory components of a successful FDNA instrument [1].

Time Domain Network Analysis (TDNA) has unique characteristic features that provide a useful alternative to FDNA, particularly at high frequencies. TDNA systems are less complex than the normal FDNA system, with only a portion of the system using microwave components. In the digital electronics industry, network analyzers are uncommon, but fast sampling oscilloscopes which offer many possible channels with fast response times are routinely available. When configured for TDR/TDT measurements, they measure signals collected in response to a transient source. A combined pulse source and sampling head can be located remotely from the TDNA system with all interconnects being either low frequency or slow logic. It is conceivable that this portion could be integrated with a microwave probe, making extremely high frequency measurements possible since the cable and connector losses, as well as the losses associated with the FDNA test set, are eliminated [2].

1.1 Time Domain Measurements

In the time domain, a microwave network can be characterized by either one or a combination of two methods, namely, the Time Domain Reflection (TDR) and the Time Domain Transmission (TDT). TDR measurements can be used to determine the return

loss, the standing wave ratio, the reflection coefficient, and the scattering parameters S_{11} and S_{22} of a Device Under Test (DUT). TDT measurements can be used to determine the propagation time, the length, the gain or loss, the crosstalk, the transmission coefficient, and the scattering parameters S_{21} and S_{12} of a two-port DUT.

Unfortunately, error correction is difficult to apply directly in the time domain and is often insufficient to fully characterize all types of devices. Depending on the digital sampling oscilloscope, the sampling head and the measurement environment, time domain measurements may not be suitable for characterizing devices with very small dimensions or over a wide bandwidth. The major disadvantages of TDNA are error correction and deconvolution of the device response from the overall set-up response when closely spaced discontinuities are involved.

1.2 Need for Extracting Models from Time Domain Measurements

Frequency domain analysis of circuits has a long tradition and has its roots in analog system design. For GHz frequencies, characterization in the frequency domain is most accurate using FDNA. Time domain analysis using oscilloscopes on the other hand is more suitable for digital-IC design. The multiple channel capability of oscilloscopes and the possibility of viewing the waveforms in the time domain are convenient for testing wide busses. Due to the trend towards a mixed signal environment, increasing questions arise as to the adaptability of the existing FDNA and TDNA to the analysis of mixed signal circuits. TDNA is not as accurate as FDNA for measuring a frequency

domain response. In a mixed signal environment, where we have to deal with both wide busses and high frequencies, a combination of FDNA and TDNA techniques is the best solution. But there is a possibility of using either FDNA or TDNA for mixed signal circuits. Conversion of frequency domain data to the time domain and vice versa is common using Fast Fourier Transform (FFT) and inverse FFT techniques, as it also is using high resolution spectrum estimation techniques. FDNA equipment is expensive and limited mostly to two channels. This factor plays a major role in choosing TDNA for characterizing packaging structures. Due to the lower costs of TDR/TDT instruments, TDNA may find significant application in competitive industries like wireless communications, where amortizing the cost of expensive test equipment can significantly increase component price [3].

The task of developing models from measurements (either frequency domain or time domain) needs accurate measurements as well as robust algorithms to extract the required parameters. The modeling process (Figure 1.1) is outlined in [4]. Several modeling algorithms have been developed in recent years, especially for non-uniform interconnections and packages. Most designers prefer models with lumped and distributed elements describing interconnections, packages, and components. These models can be handled without conversions by classical circuit simulators [4]. Of late, mathematical models like rational function models are also being incorporated into classical circuit simulators. Among the modeling algorithms, the ones based on time domain measurements have been reasonably popular.

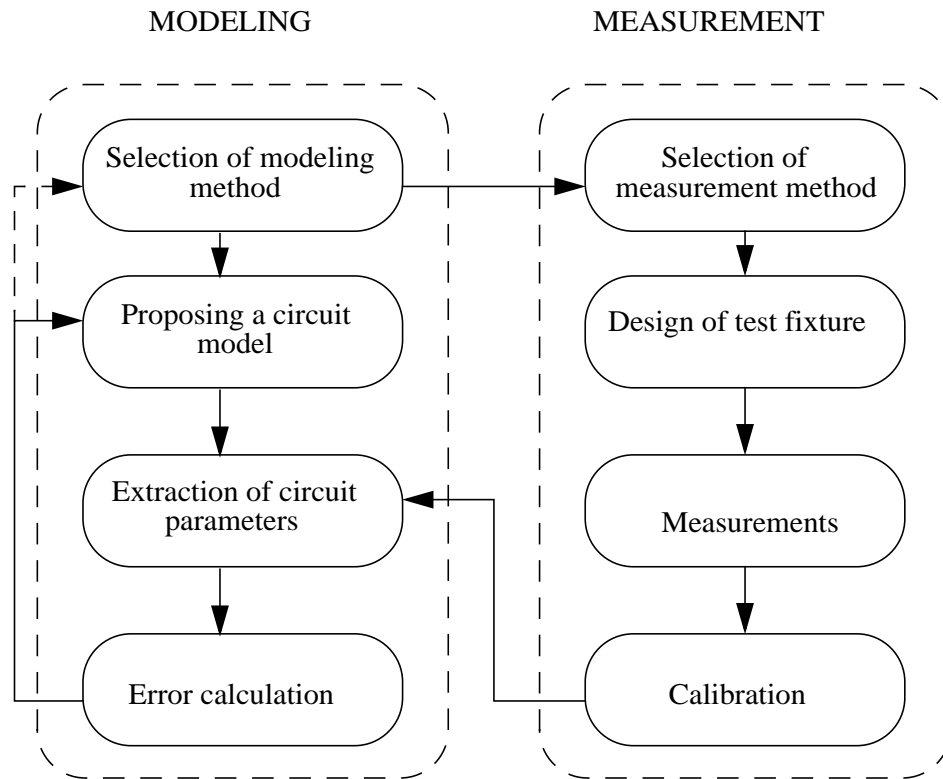


Figure 1.1 Flow Chart for Circuit Modeling of Components, Interconnections, and Packages

1.3 Measurement System

A practical system for measuring both transmission and reflection scattering coefficients is shown in Figure 1.2 [5]. A pulse generator sends a pulse down a transmission line to the DUT. The pulse shape may be either a step or a smoothed impulse. If higher frequency results are required, the impulse waveform is chosen, since for the same voltage amplitude, the impulse has a higher spectral amplitude than the step.

If information is required over only an octave or smaller bandwidths, other pulse shapes, like the doublet or several RF cycles, will provide larger spectral amplitudes over a limited range. A trigger signal may also be generated to trigger the waveform recorder. A pickoff probe, usually a high impedance voltage probe of sufficient bandwidth for the timing accuracy needed, is used to sample the incident and reflected waveforms. The sampling head contains a high performance amplifier for capturing the incoming signal of a channel. An oscilloscope is used as a sample-and-hold circuit with an exceptionally narrow sample gate, typically a few tens of picoseconds, and a hold period equal to the period of the pulse generator. The sampled waveform is subjected to signal processing and converted to the frequency domain to extract the desired frequency information.

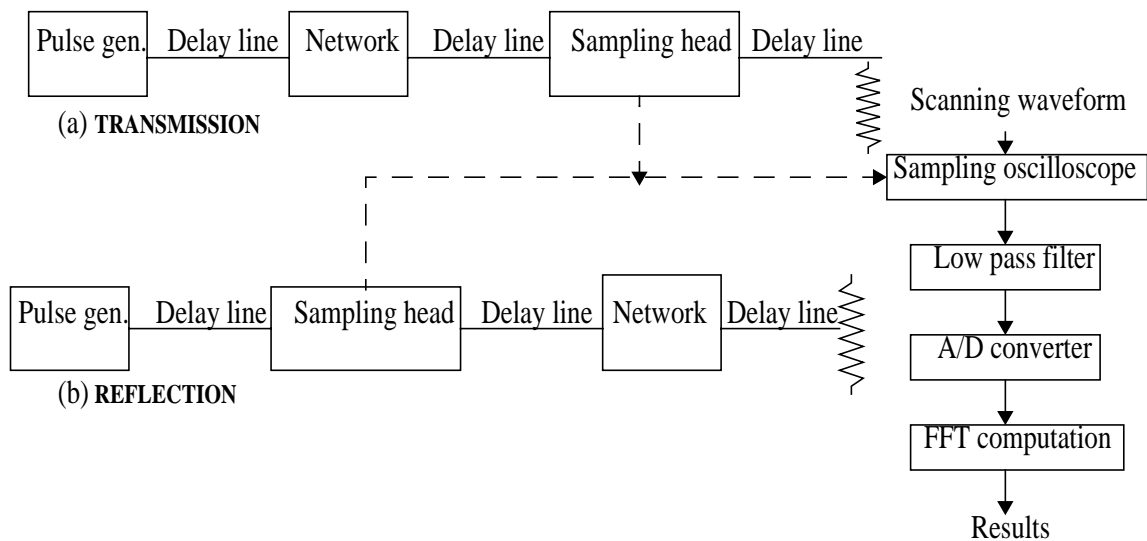


Figure 1.2 Experimental System for Transient Measurements

Measurements require a different set-up for different types of devices and the following additions are common:

- * The size of the components determines the type of probing. If the DUT is large and the device characteristics are not altered much using a SMA type of connector, the measurement is much easier. If the device is small we need wafer probing. This can be done using commercially available coplanar probes.
- * Sometimes, the reflected or transmitted pulse from the device can be very small ($\sim 2\text{-}3\text{ mV}$) for an input pulse of amplitude $\sim 250\text{ mV}$. In such cases we need an external source of much larger amplitude to capture the device behavior for which the measurement set-up has to be modified.
- * The frequency bandwidth of the model obtained depends on the rise time of the input pulse and is discussed in the next section. The standard internal DSO source has a 35 ps rise time which could be degraded to $\sim 100\text{ ps}$ due to the cables, etc. This translates to a frequency bandwidth of 3.5 GHz. If larger bandwidths are required, small rise time external sources have to be considered.
- * The effect of the cables and the probe tips have to be calibrated out, so we need calibrating structures which are made in the same process conditions as the device. So the devices to be characterized need to have calibrating structures on the same substrate for improved accuracy.

1.4 Limitations of TDR/TDT Measurements

Depending on the digital sampling oscilloscope, the sampling head, and the measurement environment, time domain measurements may not be suitable for characterizing devices with very small dimensions or over a wide bandwidth. Five effects that may limit the resolution and usefulness of TDR/TDT measurements are

- (1) **System rise time:** Any practical system will have a multitude of closely spaced components in the returned signal. The ability of TDR equipment to resolve these depend on the response time of the overall combination of step generator and sampling head. The rate of rise of the interrogating pulse is a major factor in determining the overall response of the system. The overall criterion for a choice of the generator also depends on the largest ratio of spectral amplitude to system noise level over the frequency range of interest. In the time domain, the rise time, T_r , of the signal determines the bandwidth, BW, and are related by Eq. 1.1 [6].

$$BW = \frac{0.35}{T_r} \quad (1.1)$$

The minimum temporal resolution is the system rise time, T_r . The finite rate of rise of the interrogating pulse sets a limit to the magnitude of the reactive component of an impedance that can be distinguished. The minimum spatial resolution (Δx) of a TDR measurement can be expressed as Eq. 1.2 [6]

$$\Delta x = \frac{CT_r}{2\sqrt{\epsilon_{\text{eff}}}} \quad (1.2)$$

where C is the speed of light in vacuum, and ϵ_{eff} is the effective dielectric constant of the medium. With a 25 ps generator and 25 ps scope, the TDR system rise time, which will be equal to the square root of the sum of squares of the rise

times of each component, would be 35 ps. Minimum spatial resolution would be 2.5 mm for an ϵ_{eff} of 5. A spatial resolution of 0.4 mm in an air medium and 0.1 mm for high dielectric media has been reported in [7]. Broad band oscilloscopes up to 150 GHz are described in [8].

- (2) **Loss effects:** For low loss short lines, losses may not be a problem because the effect is too small to distort the rise time. When making measurements over long or lossy cables, the problem becomes significant. The loss on most transmission lines can be attributed to the skin effect caused by the finite conductivity of the electrical conductors. In the frequency domain, the attenuation factor becomes proportional to the square root of the frequency. As a result, the high frequencies become attenuated more than the low, resulting in a rise time degradation of the TDR signal [9]. This places a limit on the characterization of such lossy devices.
- (3) **Excessive noise on the cable:** Most commercial TDR units utilize a step waveform of about 250 mV amplitude and utilize tunnel diode circuitry, hence they are quite sensitive and vulnerable. The solution to the problem of noisy lines is to increase the level of the TDR signal until it is significantly greater than the noise. This noise is not usually significant when measured in a well shielded environment as in a lab.
- (4) **System errors:** Because of the nonideal nature of the equipment used, some random and systematic errors will be introduced into the measurements.
- (5) **Multiple discontinuities:** Discontinuities that may be in front of the discontinuity of interest complicate TDR analysis because of the multiple reflections occurring between them. The effects of these discontinuities can be de-embedded from the DUTs response to a certain extent by using suitable deconvolution techniques.

1.5 Advantages and Disadvantages of TDNA

FDNA and TDNA each has its own advantages. Applicability of either one depends on the device under test. Some advantages and disadvantages of TDNA are as follows [9].

Advantages

- * Clear and natural representation of transient wave phenomena that permits the physics of propagation to be easily grasped and gives a qualitative understanding of transient phenomena.
- * Broadband measurements without limitations imposed on sampling in the frequency domain.
- * Equipment faults are located easily in the time domain. These include bad connectors, cable faults, impedance mismatches, and the like.

Disadvantages

- * Frequency domain results obtained from TDR/TDT measurements can be of limited accuracy.
- * Impedance mismatches produce reflections.
- * Accuracy will be impaired by the nonlinear sweep, nonlinear deflection and inaccuracies in A/D converters.

1.6 Review of Time Domain Characterization Methods

There are basically four approaches for the parameter and parasitic extraction of packaging structures such as transmission lines, vias, discontinuities (bends, taper),

connectors, pins, planes, and integral passives from time domain measurements. Because the time signature due to inductive, capacitive and resistive discontinuities is clearly visible, approximate values for a lumped element equivalent circuit can be adjusted to obtain a good model. The fifth subsection deals with such methods.

The first approach is unique to time domain measurements where natural time windowing is used. The short pulse propagation method can be used to extract the propagation factor and characteristic impedance very accurately for low loss transmission lines without the need for any calibration. The second approach is based on reflection measurements and the basic layer peeling algorithm to extract reactance parameters from the constructed characteristic impedance profile. An extension of this method is used on common mode and differential mode TDR measurements for calculating self/mutual capacitances and inductances of coupled lines. The third approach is suitable for lossy transmission lines or for devices for which the scattering parameters are to be calculated, wherein the TDR/TDT waveforms are transformed to the frequency domain and suitable de-embedding techniques are applied. The fourth method is based on an exponential approximation of the measured time domain waveforms. Extensions to the last three approaches can be used for single and coupled uniform and nonuniform interconnects, including bends and junctions. All these methods are briefly presented in the following sub-sections for characterizing the packaging interconnect structures shown in Figure 1.3 [10].

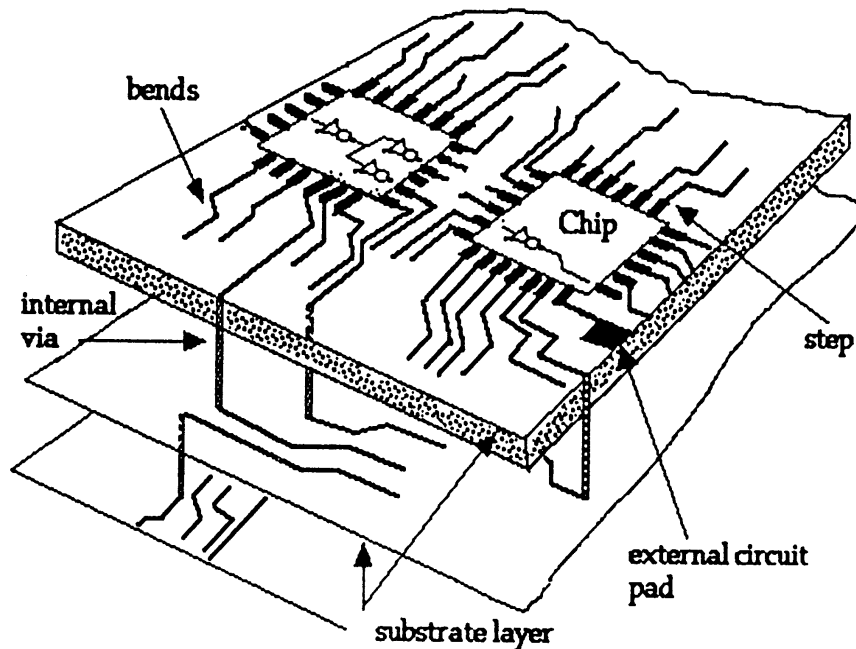


Figure 1.3 Interconnect Structures - Transmission Lines, Bends, Steps, Vias, and Pads

1.6.1 Short Pulse Technique

A simple short pulse technique for completely characterizing the frequency dependent electrical properties of resistive interconnections has been described in [11]-[12]. This method is based on calculating the complex propagation constant, $\gamma(f)$, of a wave on a quasi-TEM transmission line from the time domain measurements. Pulses are transmitted on two different lengths of otherwise identical lines and are time windowed to eliminate any unwanted reflections. The Fourier spectra then contains the information about the forward travelling wave only. The ratio of the complex spectra yields the

propagation constant

$$\alpha(f) + j\beta(f) = -\frac{1}{l_1 - l_2} \ln \frac{A_1(f)}{A_2(f)} + j \frac{\Phi_1(f) - \Phi_2(f)}{l_1 - l_2} \quad (1.3)$$

where $\alpha(f)$ and $\beta(f)$ are the frequency dependent attenuation coefficient and phase constant, respectively. $A_i(f)$ and $\Phi_i(f)$ are the amplitude and phase of the transforms corresponding to lines of lengths l_1 and l_2 , respectively, with $l_1 > l_2$. No de-embedding or calibration is required since the effect of interface discontinuities cancels out. This method has been successfully applied to thin film transmission lines with a loss tangent of 0.013 and the worst discrepancy reported in the calculation of attenuation was 5.8% [11]. The frequency coverage of this method has been extended to 70 GHz using photoconductive switches for pulse generation and sampling [12].

1.6.2 Dynamic Deconvolution Procedure

For the general case of distributed reflections or multiple discontinuities, the resulting waveform in the time domain can be characterized by a time dependent impedance which is obtained from the TDR measurement as in [10]. This nonuniform impedance profile can be modeled by cascaded uniform transmission line sections using the transfer scattering matrix of the individual sections. The impedances of the piecewise constant cascaded transmission line model consisting of a finite number of sections are

extracted in a sequential order using the reflected waveform for a given incident waveform. The algorithm is based on the basic dynamic deconvolution procedure or the layer peeling algorithm. This procedure includes all the distributed reflections in the entire structure.

For a cascaded two-port network as shown in Figure 1.4, the transfer scattering matrix for each section is given by Eq. 1.4

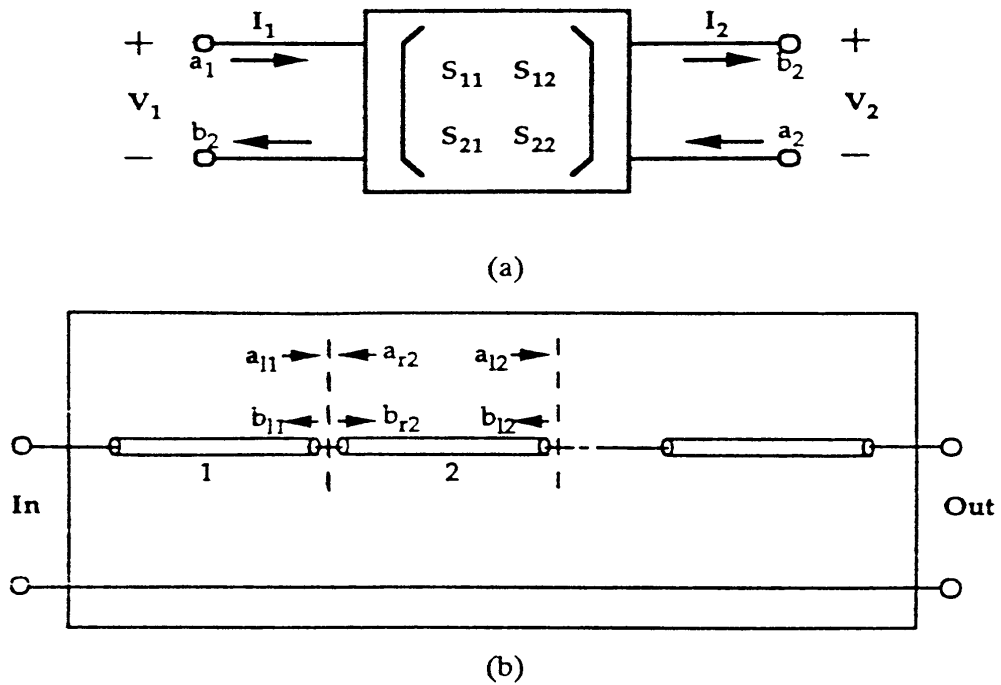


Figure 1.4 (a) Scattering Parameters of a Two-port Device (b) Cascaded Piecewise Uniform Transmission Lines

$$\begin{bmatrix} b_r(i) \\ a_r(i) \end{bmatrix} = \begin{bmatrix} T_{11}(i) & T_{12}(i) \\ T_{21}(i) & T_{22}(i) \end{bmatrix} \begin{bmatrix} e^{-sT_o} & 0 \\ 0 & e^{-sT_o} \end{bmatrix} \begin{bmatrix} b_1(i+1) \\ a_1(i+1) \end{bmatrix} \quad (1.4)$$

where $T(i)$ is shown in Eq. 1.5, ρ is the reflection coefficient and T_o is the delay in each section.

$$[T(i)] = \left(1 - \rho_{i, i+1}\right)^{-\frac{1}{2}} \begin{bmatrix} 1 & \rho_{i, i+1} \\ \rho_{i, i+1} & 1 \end{bmatrix} \quad (1.5)$$

Given an initial condition, which can be that the first section has the same impedance as that of the TDR system, the first layer can be peeled. Eq. 1.4 is iterative and can be used to extract the reflection coefficients and the impedances in a sequential manner. Thus the time domain response of an interconnect system can be represented by a cascaded set of transmission lines, each with characteristic impedance Z_o and delay T_o . The total inductance and capacitance of this transmission line system can be calculated

using the impedance and time delay in each section given by Eq. 1.6.

$$L = \sum_{i=1}^n Z_{oi} T_{oi} \quad C = \sum_{i=1}^n \frac{T_{oi}}{Z_{oi}} \quad (1.6)$$

The one-dimensional peeling algorithm has been extended to the multidimensional peeling algorithm in [14] for the analysis of coupled lines. Multiconductor nonuniform coupled lines have been characterized in terms of cascaded uniform coupled lines whose characteristic parameters are extracted from the multiport time domain reflection measurements in [13]. In these papers, a TDNA type of calibration was used where two-port error correction is done in the frequency domain. The calibrated response is transformed to the time domain for the analysis.

1.6.3 Frequency Domain Mapping Method

The third method is very similar to the post processing done for Vector Network Analyzer (VNA) scattering parameter measurements. The measured transmission terms for the line, S_{21}^L , and the thru, S_{21}^T , are frequency domain parameters obtained from the FFT of the corresponding time domain transmission measurement data. A complex propagation factor γ , is calculated by the frequency domain equivalent to deconvolution,

using

$$\lambda_{\text{est}} \equiv \frac{S_{21}^L}{S_{21}^T} = \lambda \left(\frac{1-d}{1-\lambda^2 d} \right) \quad (1.7)$$

where

$$\lambda = S_{21}^{\Delta l} = e^{-\gamma l} \quad d = S_{22}^A S_{12}^T S_{21}^T S_{22}^B$$

The value of d is derived from the two-port error model. A small error ($d \ll 1$) can be ensured if the measurement system match to the transmission line is adequate. When the measurement system match is inadequate, a round trip thru delay longer than the complete impulse response associated with the difference in line lengths is required to allow determination of transmission line propagation characteristics from the deconvolution of the line and thru measurements [15].

For general lossy systems, two-port Time Domain Network Analysis (TDNA) consists of measurements of known terminations (i.e., open, short, match) to establish a reference plane, analogous to that of a VNA. The time domain waveforms of the calibration standards and the DUT are then converted to the frequency domain for processing and determination of the associated scattering parameters for the DUT [16]-[20]. The error correction procedure for one-port TDNA is described in [21]. This calibration procedure was extended to a two-port TDNA [2]. A frequency domain error

model and the number of standards required is discussed in detail [22]-[23] and calibration standards are well studied [24],[25],[26].

1.6.4 Exponential Approximation

In this technique, approximate step response waveforms of the transmission lines are measured by TDR methods, and are deconvolved to obtain an approximate time-domain scattering matrix for the circuit [27]-[28]. In discrete time, the reflected waves $V_{\text{TDR}}[n]$ are related to incident voltage waves $V_i[n]$ according to Eq. 1.8, for a linear time-invariant network.

$$V_{\text{TDR}}(n) = S_{11}(n) \otimes V_i(n) \quad (1.8)$$

Suboptimal filtering and discrete differentiation have been used to improve the conditioning of the deconvolution of a single element response from the whole response. The impulse response scattering parameters are approximated by a sum of weighted exponentials of the form shown in Eq. 1.9, where the k_i and p_i are the residues and poles, respectively.

$$s(t) = k_1 e^{p_1 t} + k_2 e^{p_2 t} + k_3 e^{p_3 t} + \dots + k_n e^{p_n t} \quad (1.9)$$

In this research, 33 poles were used to approximate a microstrip line. Approximate equivalent models have been incorporated in SPICE to predict the delay and crosstalk. The effect of the input was deconvolved from the TDR/TDT output waveforms by transforming the data into the frequency domain using FFT which requires frequency-time-frequency translation.

Prony's method has been applied to transient data from transmission lines to construct a pole-residue model in [27]-[28]. The problem with the basic Prony's method is that the accuracy of the extracted poles degrades with increasing noise. A procedure which leads to a linear least squares fit to the data, which is closely related to Prony's method and applicable to transient electromagnetic data, is described in [29]. A companion paper discussed the problems associated with Prony's method [30]. Algorithms much more stable compared to Prony's method are available and are discussed in Chapter V.

1.6.5 Model Optimization

A multilayer embedded inductor has been characterized using a TDR waveform by iteratively adjusting approximate initial estimates of small reactive discontinuities [31]. Different sets of equivalent circuits thus developed have been used to obtain the impedance of the inductor. This method works because, once the model component for a discontinuity is fixed, changing the model components of later discontinuities does not affect the response waveform of earlier time epochs. However, the method breaks down for too closely spaced discontinuities. The characterization of the printed inductor,

resistor in [31],[32] is mostly based on tweaking the parameters to fit the simulation to the measurement.

Time domain techniques have been used to characterize and model thick film components. The models have been obtained by iteratively adjusting an initial approximate model until a computer simulation of the experimental set-up yields the same results as that of the experiment. The network under test in [32] is a printed component of approximately 10-20 mils at the center of a 4" long thick film printed coplanar line. In this paper the uniqueness problem has been solved using the Hilbert transform relations to find the minimum-phase transfer function. The transfer function of the approximate model is calculated, and compared with the computed minimum-phase transfer function of the network. The model is iteratively adjusted to yield a transfer function identical to the minimum-phase transfer function.

Another approach which can be included in this section is the causality method [33]. The causality method starts from a hybrid lumped/distributed model. The transmission line to be modeled is divided into many sections. The model for each section consists of lumped elements (R, L, C) representing the discontinuities and transmission lines to account for the delay between the discontinuities. The original model is connected to an inverse model to realize a through connection ($L=0$, $R=0$, and $C=0$). The values for the lumped elements of the discontinuity model are chosen such a way that it realizes a through connection. The element values of the discontinuity model and the characteristic impedance of the transmission line are optimized to obtain a causal response. Inverting the inverse of the optimized model delivers the circuit model for the

first section. The contribution of the first section is de-embedded from the S-parameter data and the algorithm repeated for modeling all the sections of the transmission line. This method is tedious and difficult to automate. Secondly, if a section is not properly modeled, this error will contribute to the modeling errors of the following sections

1.7 Problem Statement

Packaging structures at the various levels of a system are characterized using software tools and/or network analyzer measurements. As discussed earlier, with the increasing clock frequencies for digital systems and the evolving trend towards mixed signal packages, time domain characterization methods and the development of models using time domain measurements are becoming increasingly useful. These models are SPICE compatible and can be used in a transient simulation. The measurements and analysis depend on the type and size of the structure, the frequency bandwidth, and the type of calibration required. The purpose of this research is to develop accurate characterization methods for packaging structures using Time Domain Reflectometry (TDR) and Time Domain Transmission (TDT) measurements. The following areas are addressed, namely,

- (1) Use of calibration structures and algorithms that enable the development of electrical models directly from a transient response. Since error correction is difficult in the time domain, the measured transient response is often calibrated in the frequency domain which requires short, open, thru and load standards. This is

true for the methods reviewed in Section 1.6.2, Section 1.6.3 and Section 1.6.4. After calibration, the corrected frequency domain response is reconverted to the time domain. However, it is not always possible to have these standards. The proposed method does not require the time-frequency-time translation and uses only open and short standards to develop low frequency models. The error associated with this approximation has been quantified.

- (2) Use of thru-short standards to extract the broad band frequency response of a structure from its transient response. This is based on the extraction of rational functions from the time domain data. The proposed method does not require time-frequency-time translation and hence calibration can be done entirely in the time domain. The recursive deconvolution used for removing the effect of the source from the device response is very novel and was made possible by the use of a rational function model.
- (3) Development of measurement methods that enable the characterization of low impedance structures such as thin film planes in high frequency packages. These structures have an impedance in the $\sim 1 \text{ m}\Omega$ range and due to their lossy behavior, have a transient response over a very small time window. These structures pose unique challenges during characterization and are addressed.

The application of these methods to RF packages, connectors, thin film planes, PCB planes and embedded passives has been studied. The objectives of the work are

- (1) Develop a systematic procedure for extracting equivalent circuits for a coupled line system directly from the transient response. This requires a careful construction of the fixture on which the DUT is mounted and the design of suitable calibrating structures. This type of characterization is suitable for intrasystem connectors, short interconnects such as vias, and RF leaded frame packages.
- (2) Develop algorithms and calibrating structures suitable for extracting the rational functions from the transient response of a system. Rational function models are developed using the system poles and residues that are compatible with circuit simulators such as SPICE. These models capture the broad band frequency response of the DUT.
- (3) Use the above algorithms for characterizing packaging structures such as planes and embedded passives. These represent both low loss and lossy structures.
- (4) Measure ground bounce on thin film plane structures and analyze the transient response. The ground bounce is caused by resonances in the structure and due to the lossy behavior, a small time window is available to capture the response. This problem is enhanced due to the very small amplitude of the transient response which requires a major modification in the conventional TDR/TDT set-up.

1.8 Dissertation Outline

Equivalent circuit modeling using time domain measurements is outlined in

Chapter II. Models are extracted for a high density compass connector and validated using crosstalk measurements. Chapter III discusses the characterization of RF packages using open-short calibration. The algorithm used for extracting poles and residues from simulated TDR/TDT waveforms is outlined in Chapter IV. The effect of white noise on the performance of the algorithm is also studied. Chapter V gives the details of the measurements and the modification in the extraction procedure as applied to measured data. The rational function models developed are correlated with network analyzer measurements and the error quantified. The effects of resolution and time window, parameters governed both by the signal processing algorithm as well as the measurement set-up, are discussed in Chapter VI. Chapter VII quantifies the error due to jitter and averaging, which are purely due to the TDR/TDT equipment and cannot be completely eliminated. The measurement set-up for capturing the ground bounce in thin film plane structure and the correlation to rational function model is given in Chapter VIII. Chapter IX has conclusions and suggestions for future work.

CHAPTER II

LUMPED EQUIVALENT CIRCUIT MODELING

Packaging structures can be characterized by developing accurate circuit models from TDR/TDT waveforms incorporating all the crosstalk, distortion, and associated delay. In the time domain, a simple lumped model will describe the electrical behavior of a structure as long as rise times in the source signal are significantly longer than the time of flight for a signal through the structure. For one to be able to simulate the behavior of shorter rise times, a high frequency model composed of a series of lumped element sections is required. The minimum number of sections to use scales with the ratio of the time of flight of the structure being modeled and the rise time. For electrically short structures, a lumped element equivalent circuit is preferred since the SPICE models and simulations are less time consuming.

Two coupled pins can be represented by a lumped equivalent circuit consisting of six parameters, namely, the self inductance (L) per pin, the self capacitance (C) per pin, the mutual inductance (L_m) between pins, and the mutual capacitance (C_m) between pins. These parameters can be extracted using a combination of stand-alone, common mode and differential mode measurements. The usefulness of this method is that all discontinuities associated with pin contacts, fan out on the Printed Circuit Board (PCB),

and pin pads are included in the extracted equivalent circuit, which therefore provides a true picture of the pin performance [34]. The frequency bandwidth of the model is less than ~ 1.0 GHz and is limited by the rise time degradation of the 35 ps TDR pulse source in the cables and the fixture used to mount the Device Under Test (DUT). Hence, this method is applicable to DUT's which are at least a couple of cm's in size, with a value of inductance of at least 1-2 nH, and a value of capacitance of at least 1-2 pF. The practical application of this method could be to characterize interconnects, coupled lines, package pins, connectors, parasitics of leaded frame packages, etc. For such structures it is possible to get an impedance profile from the time domain measurements from which the lumped element/distributed element equivalent circuits can be constructed.

This chapter discusses the parameter extraction and electrical characterization of a high density connector system using time domain measurements [34]-[35]. Connectors play a critical role in high speed digital systems due to the large bandwidth and high density interface required between boards/cards. Due to high speed signal propagation on these connectors, electrical design issues such as signal integrity, delay, crosstalk and operating bandwidth are important. To study these effects, development of accurate equivalent circuits are necessary that are compatible with existing SPICE simulators. Two methods are currently available for extracting the electrical parameters of connectors - use of electromagnetic field solvers that extract parameters from the physical structure by solving Maxwell's equations and the extraction of parameters directly from measurements. The problem with using EM solvers directly the connector pins studied in this investigation is two fold namely:

- * The complex shape of the connector pins (Figure 2.1) and its non-homogenous surrounding, requiring some form of approximation during modeling.
- * The omission of discontinuities associated with pads, contacts and fanout that arise when the pins are included as part of a package.

An alternative method is to use time or frequency domain measurements. Since the connector pins discussed in this paper are being targeted for digital applications, the choice was to use time domain measurements.

A lumped element equivalent circuit is preferred for the connector, since it can be easily integrated into a SPICE model. This form of representation is largely dependent on the bandwidth of the operation which is discussed in Section 2.4.1 for this connector. Lumped equivalent circuits have been extracted for packaging structures from time domain measurements in the past. In [36], the layer-peeling algorithm has been used to extract the inductance (L) and capacitance (C) matrix using TDR measurements. Both L and C matrices were extracted using a combination of stand-alone, common mode and differential mode measurements. Though this produces good results for C, the L matrix can be inaccurate, depending on the type of calibration used. An open measurement has to be combined with a short measurement to obtain the desired accuracy. In this Chapter, a through measurement has been used to extract the L and C matrices of the connector, which is less prone to errors. It is important to note that a through measurement may not be possible for all structures. In such cases, combination of open and short measurements is required as discussed in Chapter III.

SPICE models have been developed for SIPAC connectors using lumped values of resistors, capacitors, and coupled inductors in [37]. The model in [37] was extracted

using an electromagnetic (EM) solver, which was optimized to fit the measurements. This can be time consuming and requires access to an EM solver, which can accurately model the required structures. For the extraction algorithm discussed in Section 2.1, the approximate values of the model are also obtained from TDR measurements (unlike [37]).

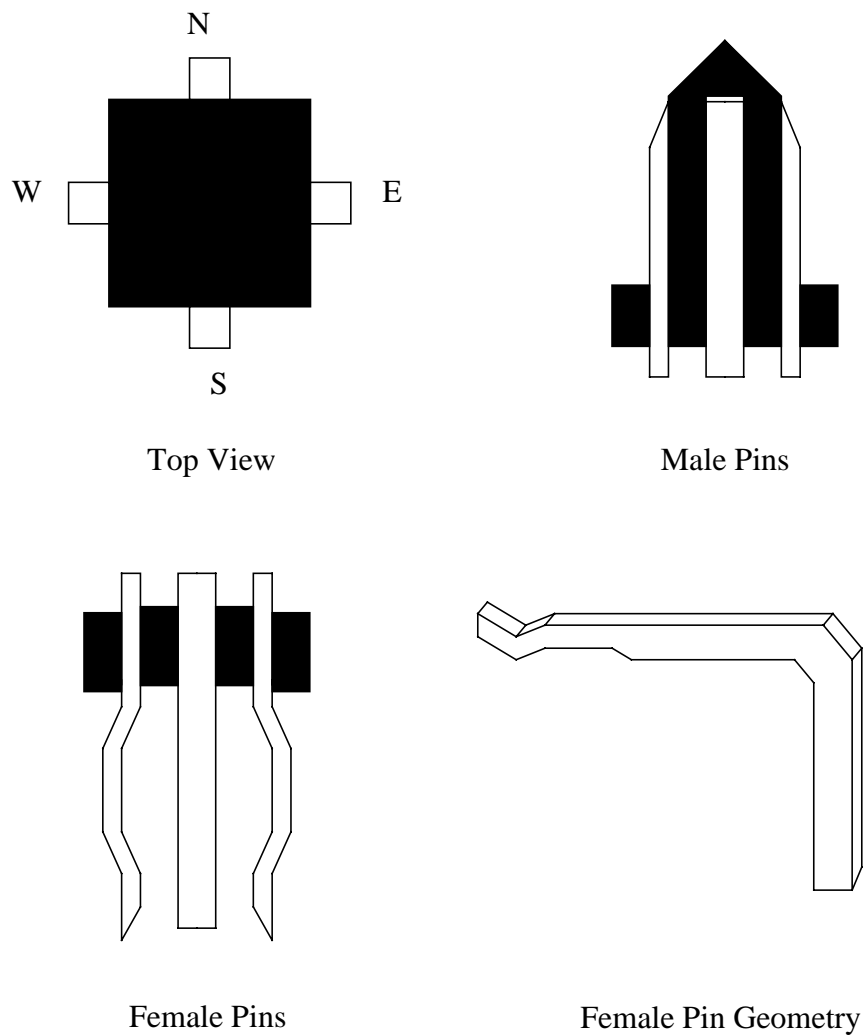


Figure 2.1 Connector Pins

2.1 Extraction of Electrical Parameters

Specific discontinuities have readily identifiable characteristic signatures in a TDR waveform. A small spike in impedance profile is due to inductance and a dip is due to capacitance. A purely resistive load changes the amplitude levels of the impedance. From a continuous TDR waveform, the inductance and capacitance of the pins can be computed as

$$L = \frac{1}{2} \int_{t_{w1}}^{t_{w2}} Z_o(t) dt \quad C = \frac{1}{2} \int_{t_{w1}}^{t_{w2}} \left(\frac{1}{Z_o(t)} \right) dt \quad (2.1)$$

where $Z_o(t)$ is the time variation of the characteristic impedance, t_{w1} and t_{w2} are the time instants corresponding to the time window, and the factor 1/2 is due to the round trip delay associated with TDR measurements [38]. Since the digital sampling oscilloscope provides sampled time intervals, Eq. 2.1 can be rewritten as

$$L = \frac{1}{2} \sum_{i=1}^n Z_{oi} T_{oi} \quad C = \frac{1}{2} \sum_{i=1}^n \frac{T_{oi}}{Z_{oi}} \quad (2.2)$$

where Z_{oi} is the characteristic impedance corresponding to the i^{th} sampling instant T_{oi} and n is the number of samples. Eq. 2.1 and Eq. 2.2 are largely dependent on the time

window and can lead to inaccurate results if the reference time is not chosen properly. Eq. 2.2 has been used for obtaining approximate L and C values from stand-alone measurements. The procedure is described in the following subsections.

2.1.1 Bare Board Measurement

The first step in the extraction of the DUT parameters is the characterization of the bare board to facilitate the representation using an equivalent circuit. TDR measurements on the bare board are used to develop an equivalent circuit for the accessories between the Digital Sampling Oscilloscope (DSO) sampling head and the DUT. This step is fairly straightforward since the parameters of the board, like the characteristic impedance of the lines and the time delays, can be read off the DSO. Little or no optimization of these parameters is required, because the deviation of the characteristic impedance from the designed value of the lines is negligible.

2.1.2 Stand-alone Measurement

The self inductance and self capacitance of the pins are extracted next. Pulses (low to high transition) are propagated onto pins 1 and 2 individually through the transmission lines on the fixture and the reflected waveforms are captured. The impedance/admittance profile extracted from the measured TDR waveform is used to calculate the inductance/capacitance, respectively. An initial guess using Eq. 2.2 is used for the equivalent circuit, which is optimized to obtain good correlation between the measured and simulated waveforms.

2.1.3 Even Mode Excitation

This represents the propagation of identical pulses (both low-high transition) on two adjacent pins. The two channels available on the sampling head can be used for the measurements. Assuming a mutual capacitance exists between the pins, the two identical pulses on the pins will cancel the effect of the mutual capacitance, as shown in Figure 2.2, provided the pulses propagate on the pins at the same time instant. In other words, any change in the time domain response for even mode excitation as compared to stand-alone measurement is due to the mutual inductance between the pins. The mutual inductance between the pins can be varied to fit the simulation with the measured waveform. It is important to note that the mutual inductance is the only parameter to be varied in this step. For the simplification in Figure 2.2 to be possible, the two pulses with identical polarity have to propagate on the two pins at the same time. Hence control of the transmission line lengths on the fixture is critical for this measurement. To simplify the even mode excitation, delay lines can be used.

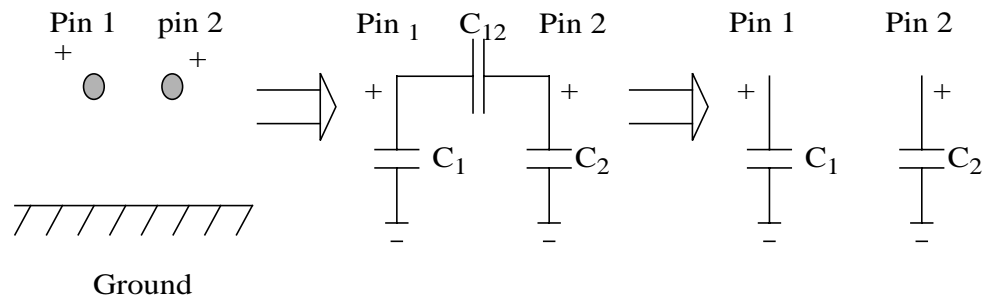


Figure 2.2 Even Mode Excitation

2.1.4 Odd Mode Excitation

This represents the propagation of identical pulses of opposite polarity (one low-high transition and the other high-low transition) on pins 1 and 2. As before, the two channels of the sampling head can be used for the measurement. This results in the increase of mutual capacitance for pins 1 and 2 which is varied by keeping all other parameters constant, so as to obtain good correlation between the simulated and measured waveforms.

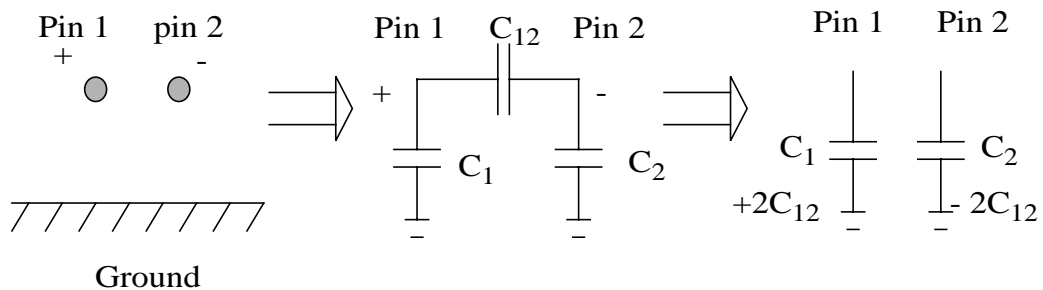


Figure 2.3 Odd Mode Excitation

As before, a necessary condition for realizing the odd mode excitation (Figure 2.3) is that the pulses must propagate on the two pins at the same time instant. This requires careful design of the fixture. These values of the self inductance, self capacitance, mutual inductance and mutual capacitance are substituted into the SPICE circuit to obtain the equivalent SPICE circuit for the entire system.

2.2 Board Design

The board design represents the most important aspect that enables the extraction process. The schematic of the Compass connector mounted on the PCB shown in Figure 2.4, consists of male and female pins mounted on two separate cards mated together. On boards PCB_1 and PCB_2, the embedded transmission lines were designed to have a characteristic impedance of 50Ω to match the oscilloscope output impedance. To achieve this design goal, both PCB's contained a layer of interconnect above a ground plane with adequate cross section, as shown in Figure 2.5. The transmission lines and ground planes were connected to the connector pins using the necessary fanout on the interconnection layer (Figure 2.6). This allowed for the inclusion of the fanout (which could be a critical parameter) and variation in the proximity of the ground pin (signal:ground ratio) in the extraction process. For adjacent interconnects, the transmission lines were adequately decoupled (20 mils spacing) to minimize coupling. This was to ensure that any crosstalk measured was due to the coupling between connector pins and not due to the coupling between transmission lines. SMA connectors were mounted on the PCB to connect the transmission lines to high speed 50Ω cables for TDR and TDT measurements.

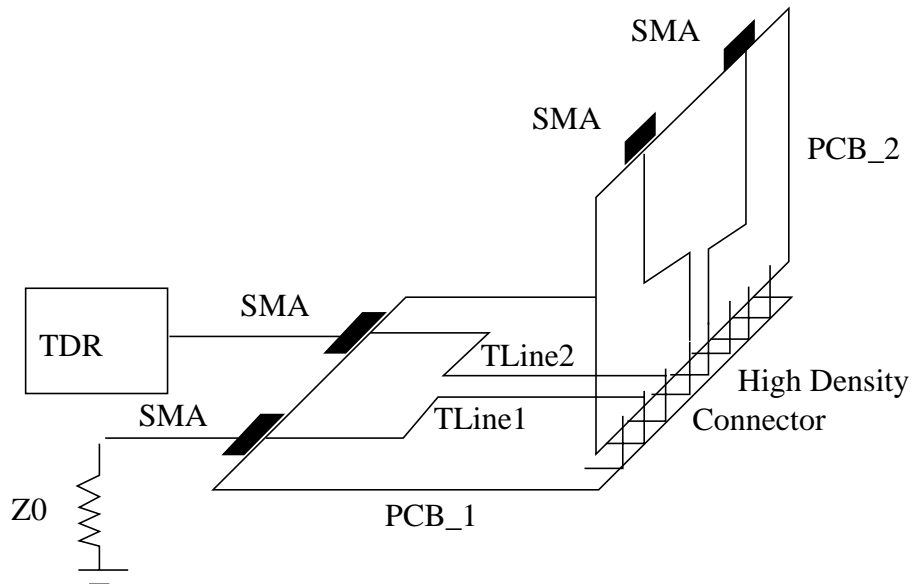


Figure 2.4 Schematic of the Measurement Set-up

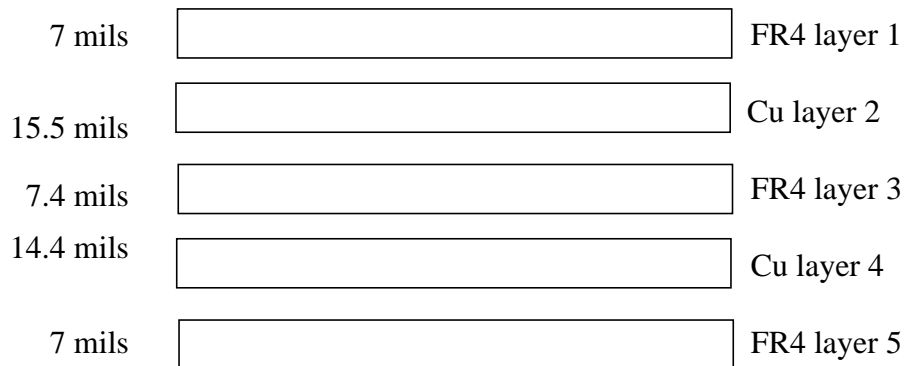


Figure 2.5 PCB Cross Section

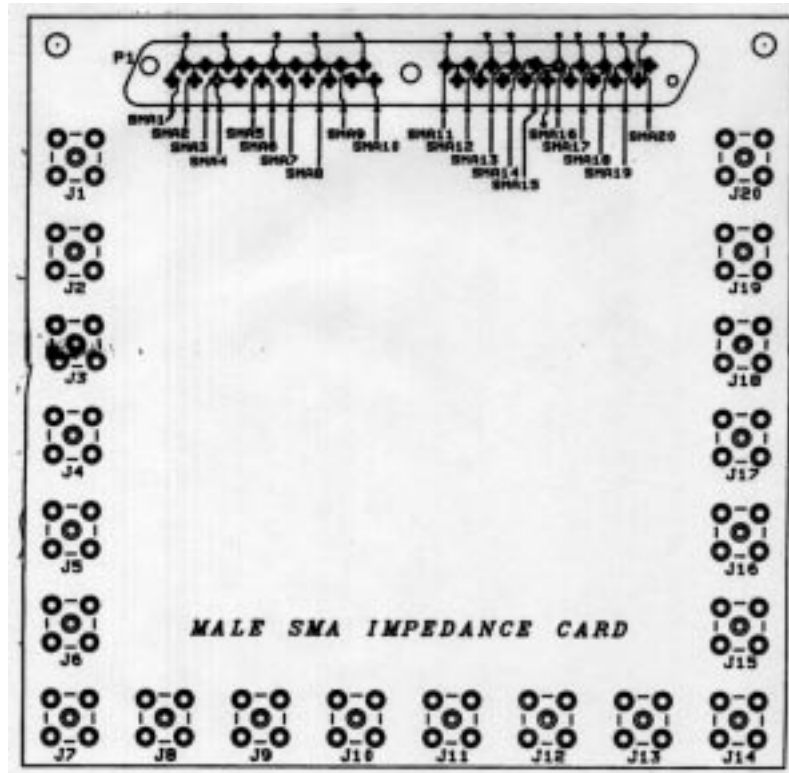


Figure 2.6 Top View of the Male Card (CAD Drawing)

2.3 Test Vehicle

The compass connector is a high density connector which provides 152 connections in sets of four pins in 2.5” space placed in North, South, East and West directions, the details of which are available in [39],[40]. Due to the position of the pins, the coupling between pins is a function of its position and the ground assignment for the surrounding pins, hence crosstalk analysis is critical. As discussed in [40], the electrical parameters of the pins were largely dependent on the ground assignments of the

surrounding pins. Hence two kinds of pin configurations were used to extract the equivalent circuit, as shown in Figure 2.7, which accounts for varying signal:ground ratios and their effect on the pin parameters. These configurations also facilitated the study of the ground:signal ratio required for high speed signal propagation so as to limit the pin inductance and crosstalk. It is also important to note that given a system consisting of ‘n’ connector pins, an ‘nxn’ capacitance and inductance matrix can be extracted using a sequence of steps, which would represent an extension of the method discussed.

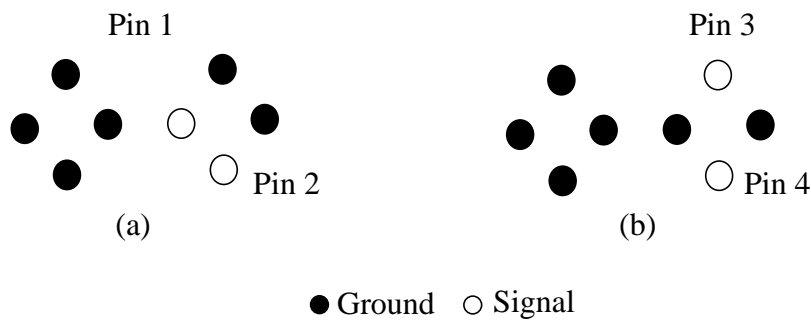


Figure 2.7 Signal and Ground Assignments

2.4 Measurements

A Tektronix 11801B digital sampling oscilloscope with 20 GHz sampling heads, each containing two channels, was used. The two channels allow for common mode and differential mode measurements. SMA connectors were used (instead of probes) to launch the signal with a voltage swing of 250 mV and rise time of 35 ps. The

experimental set-up is shown in Figure 2.8.

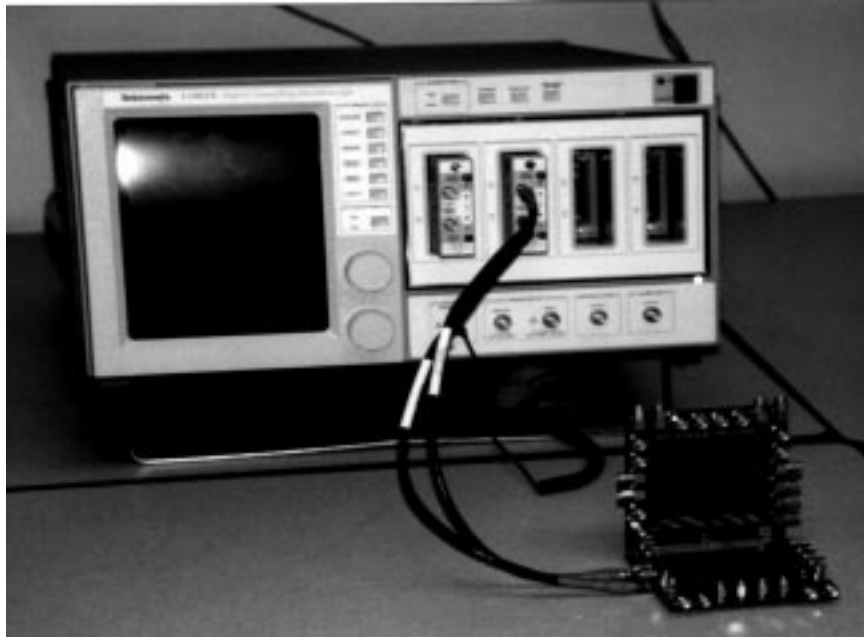


Figure 2.8 Measurement Set-up

The pulse generated by the sampling head propagates through a coaxial cable, through the SMA connector, through the transmission line on the PCB, through the mated connector and reaches the far end of the vertical PCB where it gets reflected or absorbed based on the nature of the termination. Along its path, portions of the pulse get reflected based on the nature of the discontinuity. These reflections are captured at the near end and provide a signature of the interconnect system. A typical TDR waveform is shown in Figure 2.9. As shown in Figure 2.9, the response due to the various elements of the system are separated in time, which allows for the individual analysis of various parts of the system. Moreover, there is a one-to-one correspondence between the measured

waveform and the physical connectivity of the system. The response of the SMA connector exists in between the response of the coaxial cable and PCB_1 which corresponds to the physical connectivity in Figure 2.4. Though the various elements of the system are separated in time and hence can be individually analyzed, an important factor is the method used to truncate the waveform corresponding to the individual elements. In Figure 2.9, since two 50 Ω transmission lines exist on either side of the connector pins, the response of the pins can be easily truncated. This therefore represents a more robust design as compared to [36] wherein the far end of the pin is open-ended resulting in voltage doubling at the pin location.

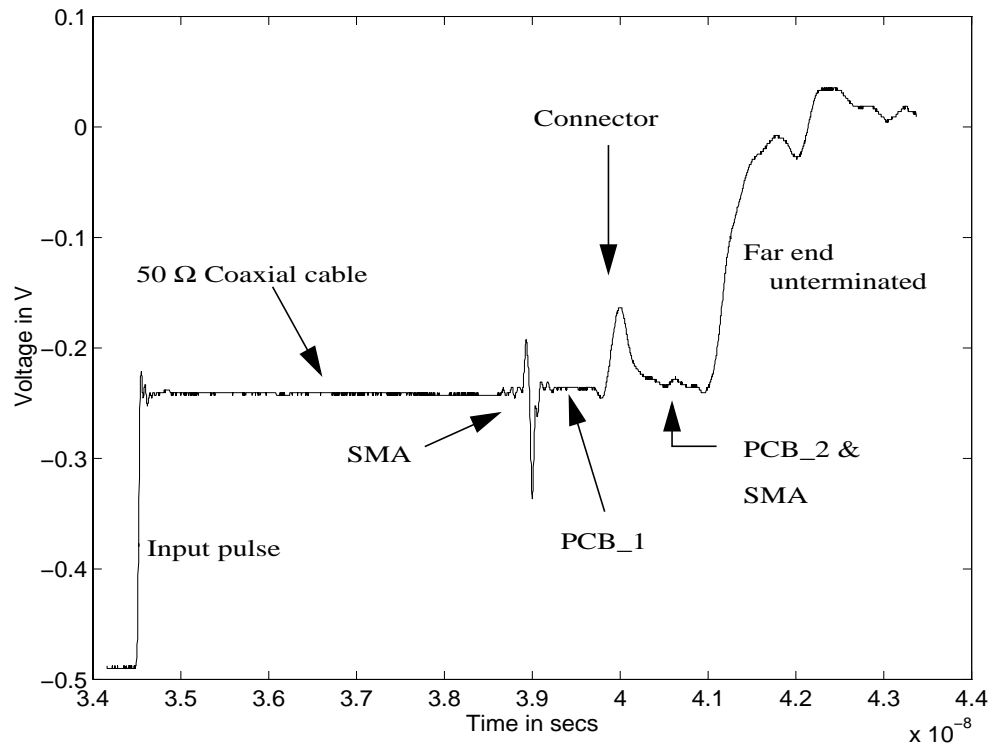


Figure 2.9 TDR Measurement of the Connector Pin

2.4.1 Validity of Lumped Element Model for the Connector

Since high speed signals propagate through the connector pins, a figure of merit for pulse propagation is the degradation in the rise time of the pulse and the additional delay penalty due to the connector. The presence of the cable and bare board between the TDR output port and the connector pin cause rise time degradation. The effective rise time (T_{eff}) is governed by Eq. 2.3 [41] which incorporates the rise time degradation due to the cable, the SMA connectors, and the microstrip lines on the bare board.

$$T_{\text{eff}} = \sqrt{(T_{\text{osc}})^2 + (T_{\text{cable}})^2 + (T_{\text{sma}})^2 + (T_{\text{bareboard}})^2} \quad (2.3)$$

where T_{osc} is the rise time at the TDR output port, and T_{cable} , T_{sma} , and $T_{\text{bareboard}}$ are the rise time degradations in the cable, SMA connector and the bare board respectively.

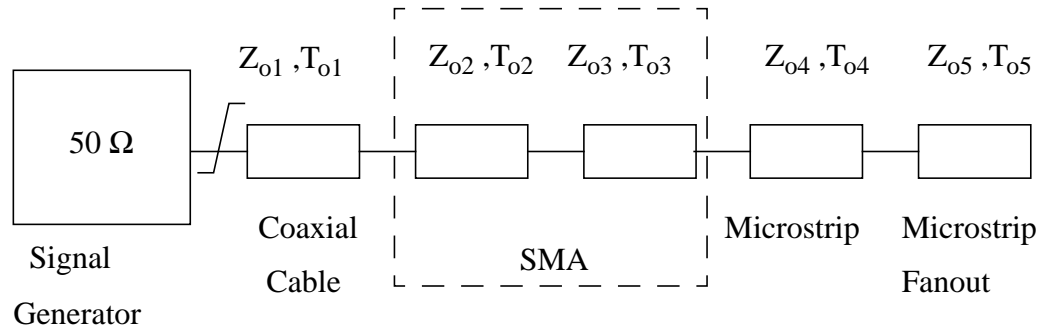
An estimate of the rise time is usually made using a short standard [42]. In this work, short measurement could not be done on the bare board, because of the construction. Hence, an open was used to estimate the rise time degradation. The pulse was launched onto an SMA connector attached to the microstrip line at one end of the board, the other end of the line was left open. A TDR measurement was made to determine the rise time between 5% and 95%. This was approximately 300 ps. For a maximum frequency of 1 GHz, the approximate wavelength in any structure is 30 cm. The approximate bandwidth that can be obtained using this set-up is ~1 GHz, calculated

using Eq. 1.1. The approximate length of the connector pins is ~ 2 cm and is much less than a tenth of the wavelength (i.e., 3 cm). This justifies the use of lumped models for characterizing the pins.

The extraction of the parameters is based on the coupled mode approach wherein any complicated coupled system can be divided up into a number of isolated parts or elements. These elements can then be represented using circuit elements such as capacitors, inductors, resistors and transmission lines which are used to describe the passive behavior. The original complex coupled system is then assumed to be made up of these isolated elements weakly coupled to each other. The coupling that exists within the original complex system is reflected by the mutual inductance and mutual capacitance parameters between the individual isolated components. If this is not a valid approximation, the solutions of the coupled system will be sufficiently different from the uncoupled solutions and hence knowledge of the solutions for the isolated elements will not be useful. This paper assumes that the sub-elements are weakly coupled to each other, which has been validated through crosstalk measurements in Section 2.5.

2.4.2 Equivalent Model of the Connector Pins

The bare board was characterized first as discussed in Section 2.1.1. The equivalent circuit for one path through the bare board (including male and female connectors) is shown in Figure 2.10. A cascaded transmission line model was used to represent the SMA connector. The impedance and timing data of Figure 2.10 were used to represent the bare board in a SPICE circuit.



$$Z_{01} = 49.6 \, \Omega, \quad T_{01} = 2.2 \, \text{ns}$$

$$Z_{04} = 53.02 \, \Omega, \quad T_{04} = 1.57 \, \text{ns}$$

$$Z_{02} = 72.79 \, \Omega, \quad T_{02} = 35 \, \text{ps}$$

$$Z_{05} = 53.02 \, \Omega, \quad T_{05} = 0.15 \, \text{ns}$$

$$Z_{03} = 20.13 \, \Omega, \quad T_{03} = 28 \, \text{ps}$$

Figure 2.10 Equivalent Circuit for the Bare Board

The self inductance/self capacitance of the pins were calculated using Eq. 2.2 from the stand alone measurements. The first set of measurements were made on the pin configuration shown in Figure 2.7(a). Since two 50 Ω transmission lines were used on either side to connect to the connector pins, the response of the pins could be easily extracted from the waveform using time windowing. The approximate values calculated using Eq. 2.2 were incorporated in SPICE netlist and optimized to fit the waveforms. The values obtained were $L_1=10.3 \, \text{nH}$, $C_1=1.25 \, \text{pF}$, $L_2=6.5 \, \text{nH}$, and $C_2=1.15 \, \text{pF}$. The correlation between the simulated and measured waveforms for pin 1/pin 2 are shown in

Figure 2.11/Figure 2.12. The mutual inductance between the pins was varied to fit the simulation with the measured even mode excited waveform and it was computed to be 3.27 nH which was incorporated into the equivalent circuit (Figure 2.13). Mutual capacitance calculated from the odd mode measurement is 0.125 pF and the final equivalent circuit is as shown in Figure 2.14. A similar procedure was used to extract the equivalent circuit for the second pin configuration (Figure 2.7 (b)). The parameters are listed in Table 2.1.

Table 2.1: Connector Parameters

Parameter	Figure 2.7 (a)	Parameter	Figure 2.7 (b)
L_1	10.3 nH (pin 1)	L_3	6.1 nH (pin 3)
L_2	6.5 nH (pin 2)	L_4	6.1 nH (pin 4)
L_{12}	3.27 nH (pin 1 - pin 2)	L_{34}	1.5 nH (pin 3 - pin 4)
C_1	1.25 pF (pin 1)	C_3	1.15 pF (pin 3)
C_2	1.15 pF (pin 2)	C_4	1.15 pF (pin 4)
C_{12}	0.125 pF (pin 1 - pin 2)	C_{34}	0.10 pF (pin 3- pin 4)

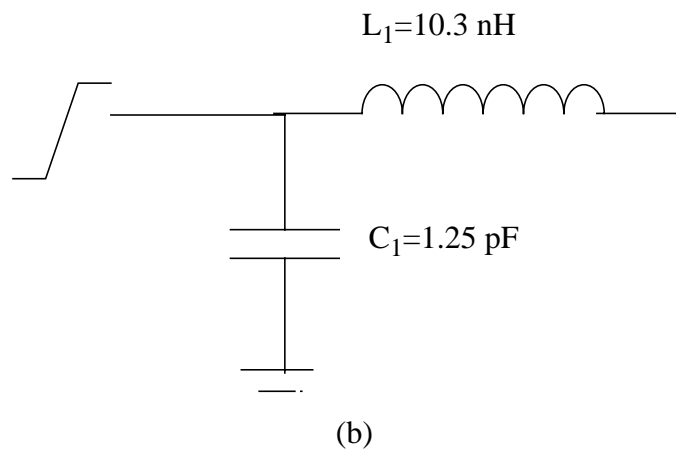
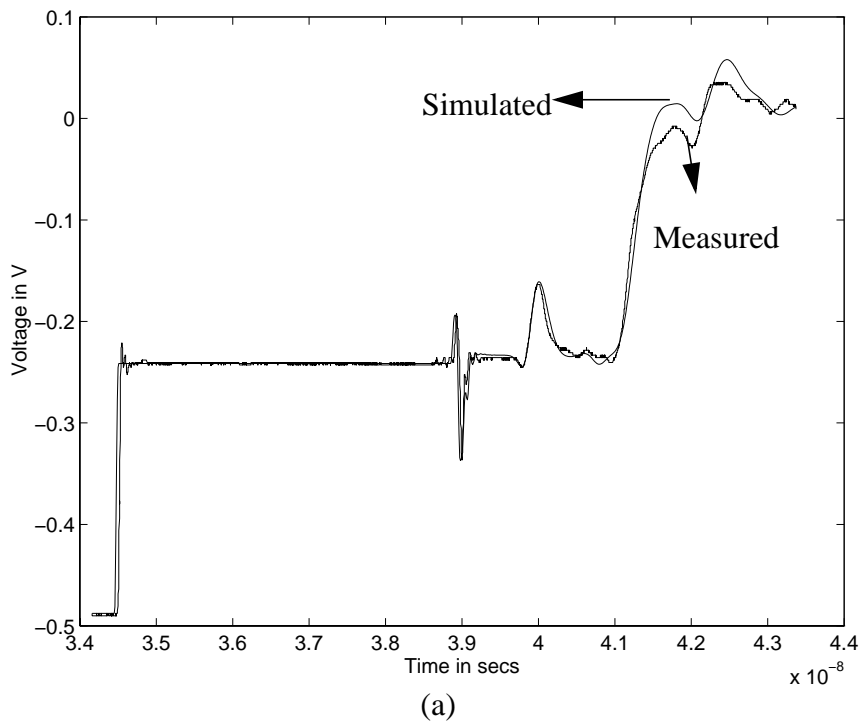
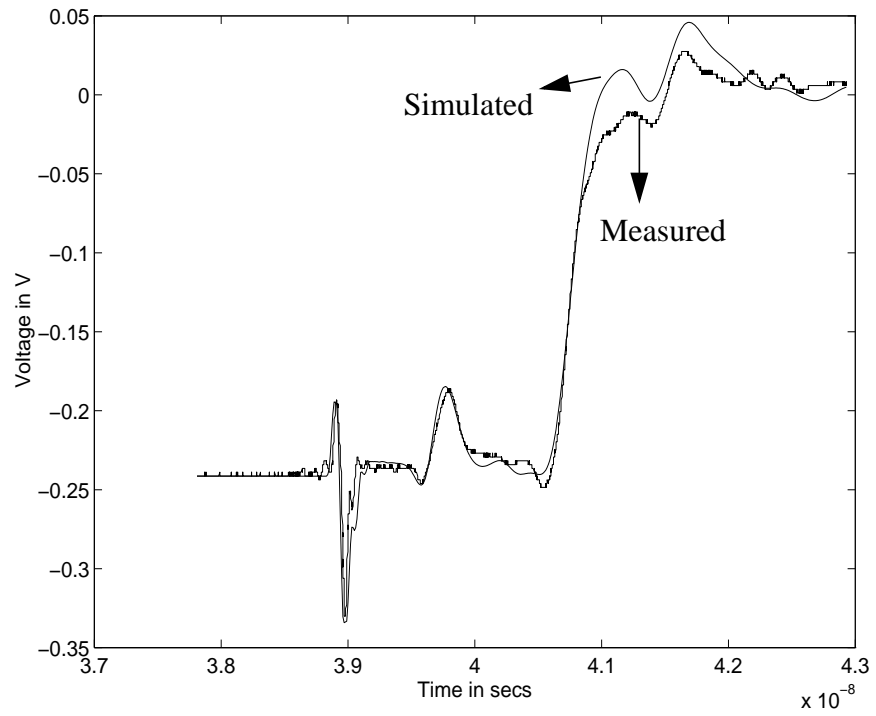
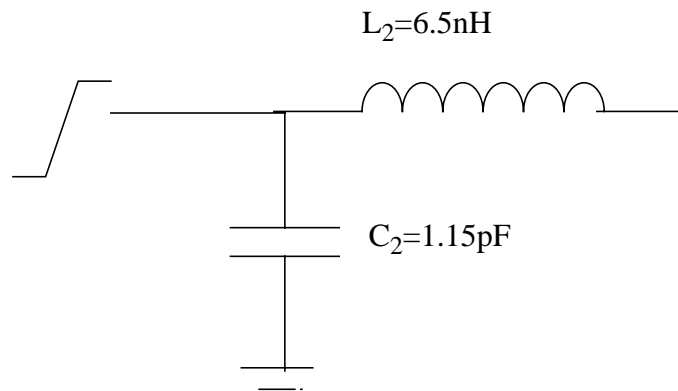


Figure 2.11 (a) Measurement to Simulation Correlation of Pin 1
 (b) Equivalent Circuit for Pin 1

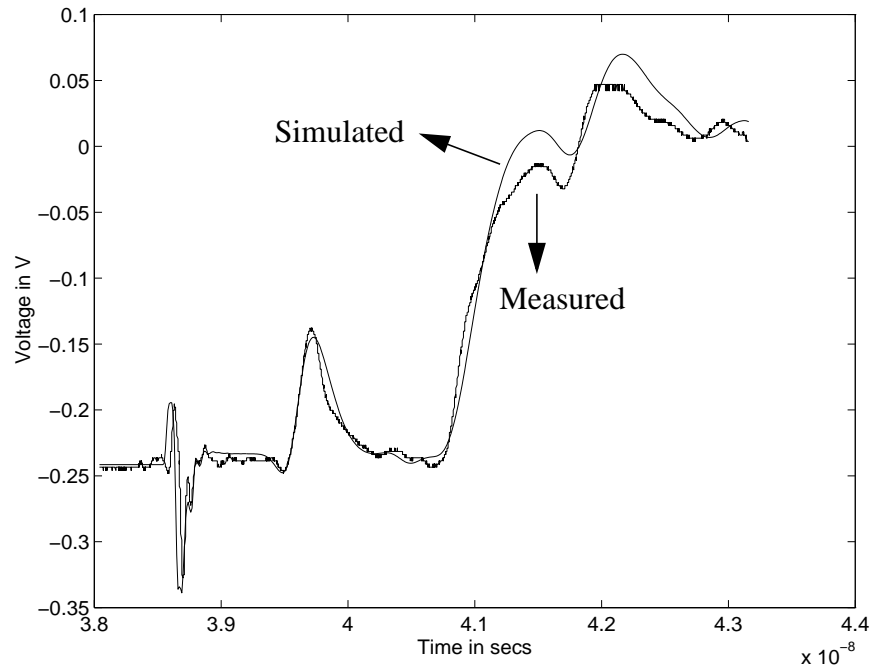


(a)

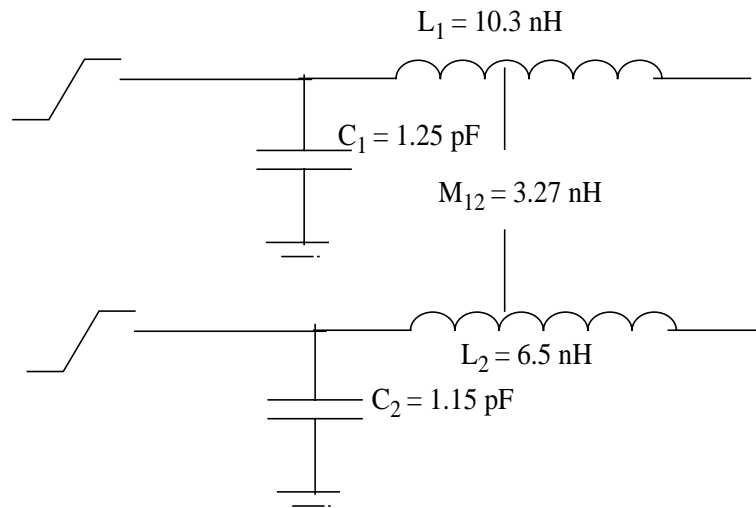


(b)

Figure 2.12 (a) Measurement to Simulation Correlation of Pin 2
(b) Equivalent Circuit for Pin 2

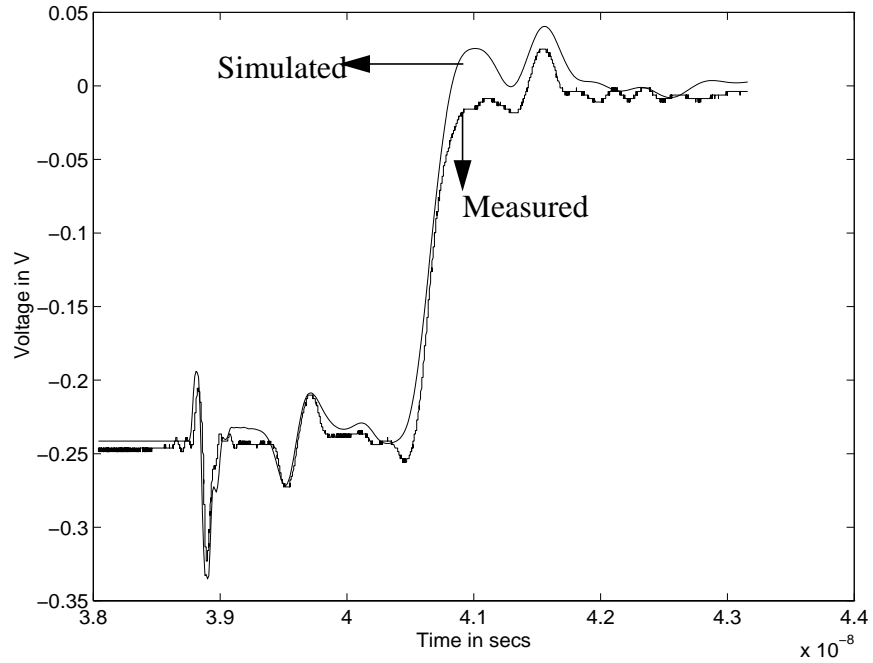


(a)

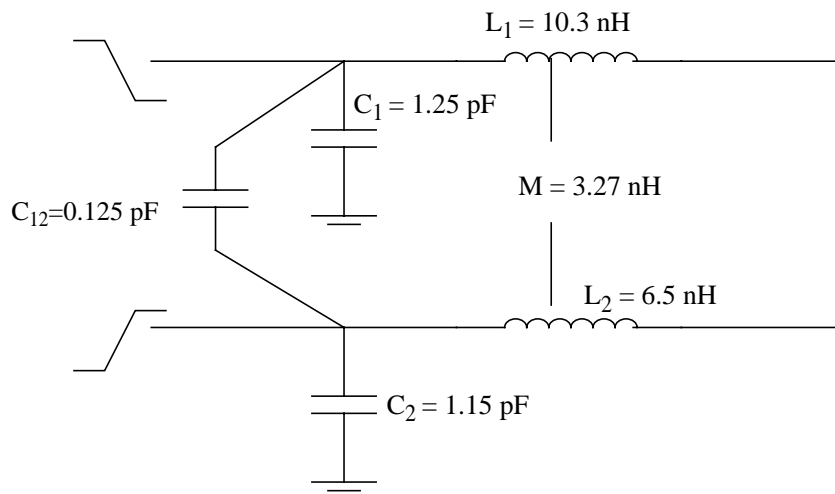


(b)

Figure 2.13 (a) Response Due to Even Mode Excitation
 (b) Equivalent Circuit with M_{12}



(a)



(b)

Figure 2.14 (a) Response Due to Odd Mode Excitation Measured on Pin 1
 (b) Equivalent Circuit with C_{12}

2.5 Model Validation Using Crosstalk

Because of the complex geometry, it was not possible to simulate the response of the connector pins using commercially available EM software. One method to ascertain the accuracy of the extracted parameters is by matching the simulated and the measured near end and far end noise waveforms using the equivalent circuit developed. The far end of both pins were left unterminated to allow for the reflection of the pulses. For the near end crosstalk measurements between two pins, a pulse (low to high transition) was propagated on pin 1 and the noise waveform measured at the near end of pin 2 on PCB_1 (Figure 2.4). The far end noise was measured at the end of Pin 2 on PCB_2. The measured near end/far end noise waveforms are shown in Figure 2.15/Figure 2.16 along with the SPICE simulation of the model developed for pins 1 and 2. As can be seen from the waveforms, the simulated waveform shape is in good agreement with the measured waveform and validates the model developed. The small discrepancy of 3 mV at the first positive peak level can be attributed to the noise between the adjacent transmission lines.

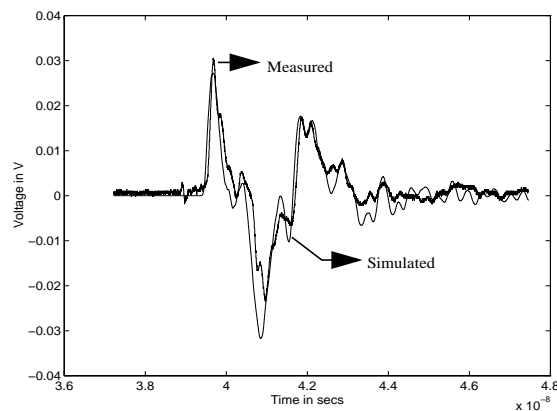


Figure 2.15 Near End Crosstalk for the Pin Configuration in Figure 2.7 (a)

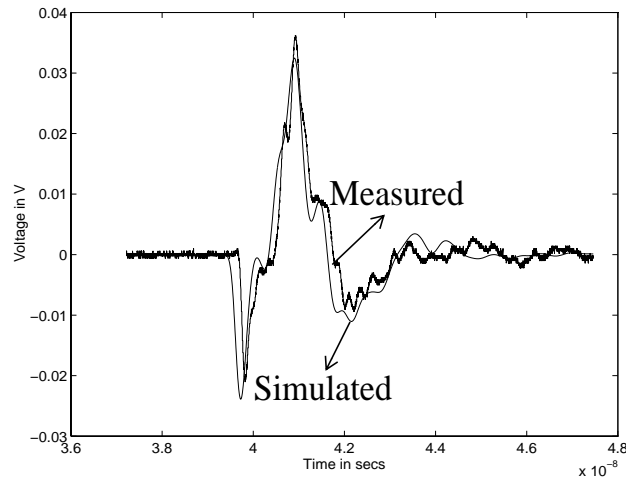


Figure 2.16 Far End Crosstalk for the Pin Configuration in Figure 2.7 (a)

Using the model developed, the peak noise generated by the models can be further confirmed by using analytical expressions for crosstalk developed in [43] and discussed in [44]. These expressions represent simplistic models that do not have the accuracy of a SPICE simulation but are useful for comparing with the measured results. The underlying assumption in the derivation is that the noise coupled on an adjacent pin due to mutual inductive and capacitive components are independent of each other and can be added in phase to obtain the total noise on the quiet pin. Since the ratio of $L_{12}/L_1 \sim 0.3$ and $C_{12}/C_1 \sim 0.1$, simplified crosstalk equations for loosely coupled systems and homogenous media have been used. It is shown through calculations that the values obtained match the measurements closely, which justifies our assumption of loose coupling to obtain the approximate values. The $\sim 50 \Omega$ lines on either side of the connector pins (Figure 2.9) have enough delay so as to avoid the reflections from the unterminated ends to affect the

peak values of the near end and far end noise in time. Hence the approximate peak values have been calculated for the matched case. A SPICE model was generated and simulated with and without the pins to calculate the delay of the connector which is 140 ps (signal surrounded by ground), measured between 50 Ω levels. The connector delay and rise time along with the mutual inductance and capacitance can be used to calculate the near end and far end crosstalk.

Near end noise on pin 2 due to the voltage on pin 1 is given by

$$V_{NE}(t) = \frac{1}{4T_d} \left(\frac{L_{12}}{Z_0} + C_{12}Z_0 \right) \left[V_{in}(t) - V_{in}(t - 2T_d) \right] \quad (2.3)$$

where T_d is the connector delay, L_{12} is the mutual inductance between pins 1 & 2, C_{12} is the corresponding mutual capacitance, V_{in} is the input voltage swing (250 mV), and Z_0 is the impedance of the transmission line. Using $T_d=140$ ps, $L_m=3.27$ nH, $C_m=0.125$ pF, $Z_0=50$ Ω and $V_{in}=250$ mV, the peak value of the far end noise is 31.98 mV. This value of peak near end noise is within 10% of the measured value of 30.2 mV. The peak reflected voltage due to the inductance and capacitance on the active pin (pin 1) can be written as [45]

$$V_{rL} = \frac{V_{in}L_1}{2Z_0T_r} \quad \text{and} \quad V_{rC} = \frac{V_{in}C_1Z_0}{2T_r} \quad (2.4)$$

where L_1 is the inductance, C_1 is the capacitance of pin 1, and T_r is the rise time. Eq. 2.4 is valid for small inductive/small capacitive reactances and large rise time values. This resulted in a rise time of 290 ps for $V_{rL} = 88.7$ mV and $V_{rC} = 26.9$ mV. This confirms the rise time value calculated in Section 2.4.1. With this value of rise time, the far end crosstalk calculated using equation Eq. 2.5 is 25.49 mV compared to the measured value of 24.1 mV. The far end crosstalk is also within 10% error and so the procedure used here for extracting the equivalent circuit is very effective for high density structures.

$$V_{FE}(t) = \frac{1}{2} \left(C_{12} Z_0 - \frac{L_{12}}{Z_0} \right) \frac{d}{dt} [V_{in}(t - T_d)] \quad (2.5)$$

For pin combination 3 and 4, the calculated value of near end noise was 15.61 mV as compared to a measured value of 15.9 mV. The calculated far end noise was 10.775 mV, whereas the measured value was 16.1 mV. This discrepancy was due to the coupling between the transmission lines on the PCB for this configuration. The noise coupled into the transmission lines on the bare board corresponding to pins 3 and 4 was measured to be ~6 mV, whereas the corresponding value for pins 1 and 2 was ~1.5 mV, which explains the increased error. The peak near end, peak far end crosstalk measured for the configurations in Figure 2.7 are listed in Table 2.2 along with the results from the SPICE simulation and analytical expressions. The peak crosstalk measured was 12.1% of the input voltage swing for the worst case configuration shown in Figure 2.7(a).

Table 2.2: Comparison of Peak Near End and Far End Noise

Configuration	Crosstalk	Measured	Simulated	Analytical
(a)	Near end	30.2 mV	27.2 mV	31.98 mV
	Far end	23.1 mV	24.8 mV	25.49 mV
(b)	Near end	15.9 mV	14.3 mV	15.61 mV
	Far end	16.1 mV	8.2 mV	10.78 mV

CHAPTER III

CHARACTERIZATION OF RF PACKAGES USING OPEN-SHORT CALIBRATION

For leaded frame RF packages, the pins are connected to the chip through a wirebond. Thus the pins to be characterized have one end open. The extraction procedure discussed in Chapter II is appropriate for a through type measurement to extract the L and C matrices, because the pin response can be time windowed. But for the RF packages, the voltage doubling due to the open pin occurs immediately after the pin response in time. This could mask the actual response leading to an error in the calculation of the self inductance. For such cases, where a through measurement may not be possible, a combination of open and short measurements can be used. A single pin requires three complex scattering, impedance, or admittance parameters. But for low frequencies and low capacitance values, as in the case of standard lead frame packages, the idea of the circuit topology can be used to reduce the number of required measurements. The method outlined in this chapter using a simple open-short calibration requires only two measurements and is applicable for extracting low frequency models (where "low frequency" refers to frequencies below 500 MHz).

3.1 Time Reference

Calibration is done entirely in the time domain, hence the time reference is an important parameter in the extraction procedure [46]. A slight variation in the start time of the waveform captured increases the inductance/capacitance to a large extent, if the values calculated using Eq. 2.2 were used as actual values instead of approximate values. For a time step of 10 ps, the inductance calculated as a product of impedance and the time interval as in Eq. 2.2 can vary as much as $\sim 50 \Omega \times 10 \text{ ps} = 0.5 \text{ nH}$. A similar variation in capacitance is $\sim 0.2 \text{ pF}$. This could lead to a very large error if the pin values are in the range where $L < 4\text{-}5 \text{ nH}$ and $C < 2\text{-}3 \text{ pF}$. Most of the packages characterized in this section have values of L in the range of $1.66 \text{ nH} - 5.125 \text{ nH}$ and C in the range of 0.1 pF and 0.5 pF . The time step can be reduced depending on the oscilloscope resolution which will lead to better results. The time step can also be reduced by using interpolation and adding additional data to reduce the error, but the accuracy can be very dependent on the interpolation technique. The steps taken to reduce the error are:

- * **Start time:** Leaded frame packages, connectors etc. require the use of special fixtures for mounting in order to make measurements. The fixture provides the transition from the pin to the oscilloscope cable through some type of transmission line and connector. Hence, the required pin response needs to be identified from the response of the fixture and the cables. TDR waveform of a short standard has been used for setting the time reference. The start time of the window is set by observing the reference waveform, when it drops below the impedance of the fixture coplanar line. From the characteristic impedance of the line ($F \Omega$) on the fixture and the characteristic impedance of the TDR/TDT ports (50Ω), the ideal reflection coefficient (ρ) seen on such a line would be $(F - 50$

$\Omega)/(F + 50 \Omega)$. This is the reference to set the start time which demarcates the device response from the accessories. This same start time determined for the reference short is used for other measurements on the pin, under the assumption that there is not much drift. The amount of drift according to the DSO/TDR setup is less than 4 ps for a measurement window greater than 1 ns. All the measurements are made for more than 1ns time window. Hence the error due to jitter can be considered minimal for these measurements.

- * **End time:** Due to the non-ideal nature of the reference short as well as the losses in the pin, there are ripples. The end time of the waveform is taken so as to include only the first data point that touches the $\rho = -1$ point. This produces some error, but considering the pin to be a lumped element, the effect of the discontinuity can be characterized over the selected time window.
- * **Measurements in a short time:** As far as possible, it is advisable to make the pin and the reference measurements in a very short span of time so as to avoid jitter.

3.2 Package Measurements

The packages were provided by National Semiconductor Corporation. The packages analyzed include SOP (20 pin), MDIP (24 pin), PQFP(48 pin), SSOP (56 pin), PQFP (48 Pin), and PQFP (80 pin) as shown in Figure 3.1. Two configurations of each package type have been used for the measurements, namely (i) **Short:** The required pins of the package are shorted to the Die Attach Paddle (DAP) which acts as a ground to the package using wirebonds. (ii) **Open:** The required pins of this package are left open. The fixture provided had six pads, three on each side. The schematic of the measurement setup and the actual setup with the fixture are shown in Figure 3.2 and Figure 3.3. The

pad pitch and the pad size were designed to suit a wide range of packages. The three pads are connected through three coplanar lines to the edge of the fixture, where they are terminated in coaxial connectors. The ground path of the pins is much shorter in the short configuration provided, than would have been the case if only the required pin was short-circuited and the all the other pins left open. Hence, the packages will show slightly lower values of inductance than the ideal case, where only the pin being measured is short-circuited and the surrounding pins are open ended. One way to get around this is to use insulating tape over the fixture to remove the effect of the adjacent pins. The fixture did not have equal delay lines between adjacent pins, so mutual capacitance and mutual inductance values could not be extracted.



Figure 3.1 RF-IC Packages Characterized

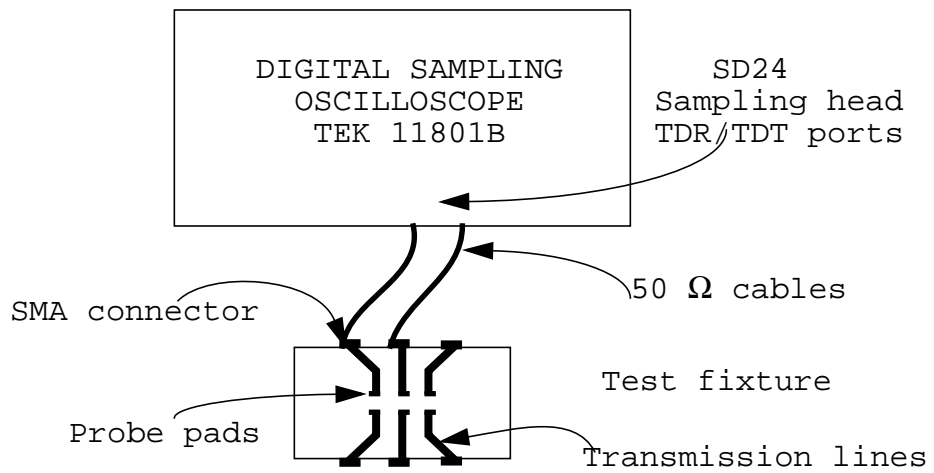


Figure 3.2 Block Diagram of Measurement Set-up

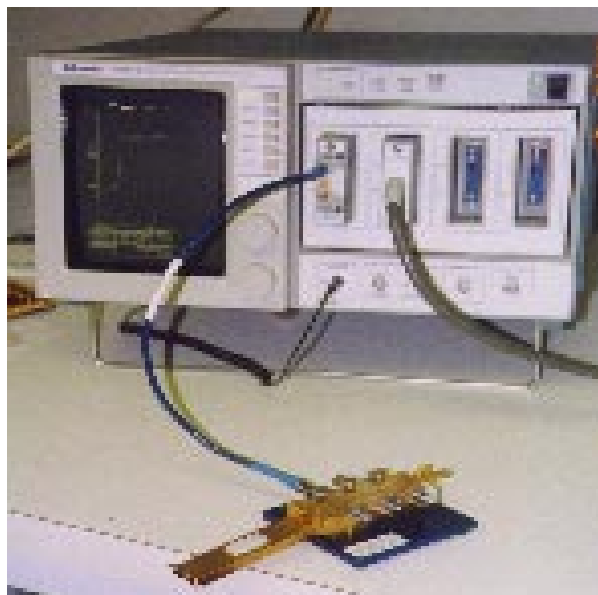


Figure 3.3 The Fixture Used and the Digital Sampling Oscilloscope

3.2.1 Time Window

A short metal strip was used to short the pad on the fixture to set the reference time. From the characteristic impedance of the coplanar line (44.5Ω) on the fixture and the characteristic impedance of the TDR/TDT ports (50Ω), the ideal reflection coefficient seen on such a line would be $(44.5-50)/(44.5+50) = -0.0582$. The reference time has been fixed at the instant the reflection coefficient falls below -0.0582 which is 3.749 ns for this measurement as shown in Figure 3.5(a). This same start time determined for the reference short has been used for the measurements on the pin. Due to the nonideal nature of the reference short as well as the losses in the pin, there are ripples. The end time of the waveform is taken so as to include only the first data point that satisfies the $\rho = -1$ condition.

3.2.2 Calculation of Self Inductance Value

For electrically short pins, the equivalent circuit could be a simple 'L' network with lumped inductance and capacitance values as shown in Figure 3.4. For small values of capacitance, if the output port is grounded, we can consider only the inductance to be in the path of the signal. Positive peaks in TDR measurement can be considered to relate to the inductive discontinuity as described in [45] which is what is seen in the TDR waveform. In other words, only the inductance value can be calculated from the measured short-circuit waveform.

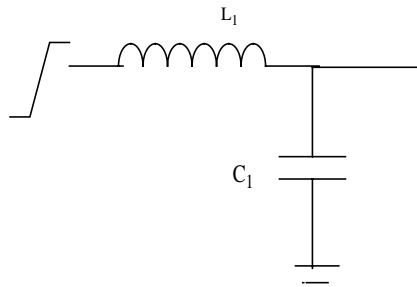


Figure 3.4 Equivalent Circuit for the Stand-alone Pins

The package with the pins short-circuited is mounted onto the fixture, so that the pads on the fixture are in contact with the pins to be measured. A pulse (low to high transition) is propagated onto each pin, one at a time. This measurement includes the inductance due to the pin and the wirebond. Eq. 2.2 is used to calculate the inductance of the pin as well as the reference short. For the reference measurement the inductance calculated was 1.2478 nH; the simulation to measurement correlation is shown in Figure 3.5(b). The effect of the pin inductance compared to the reference short is shown in Figure 3.5(c). The inductance of the pin was calculated to be 3.5634 nH. The estimated inductance is therefore 2.316 nH which is the difference between the pin inductance and the fixture inductance.

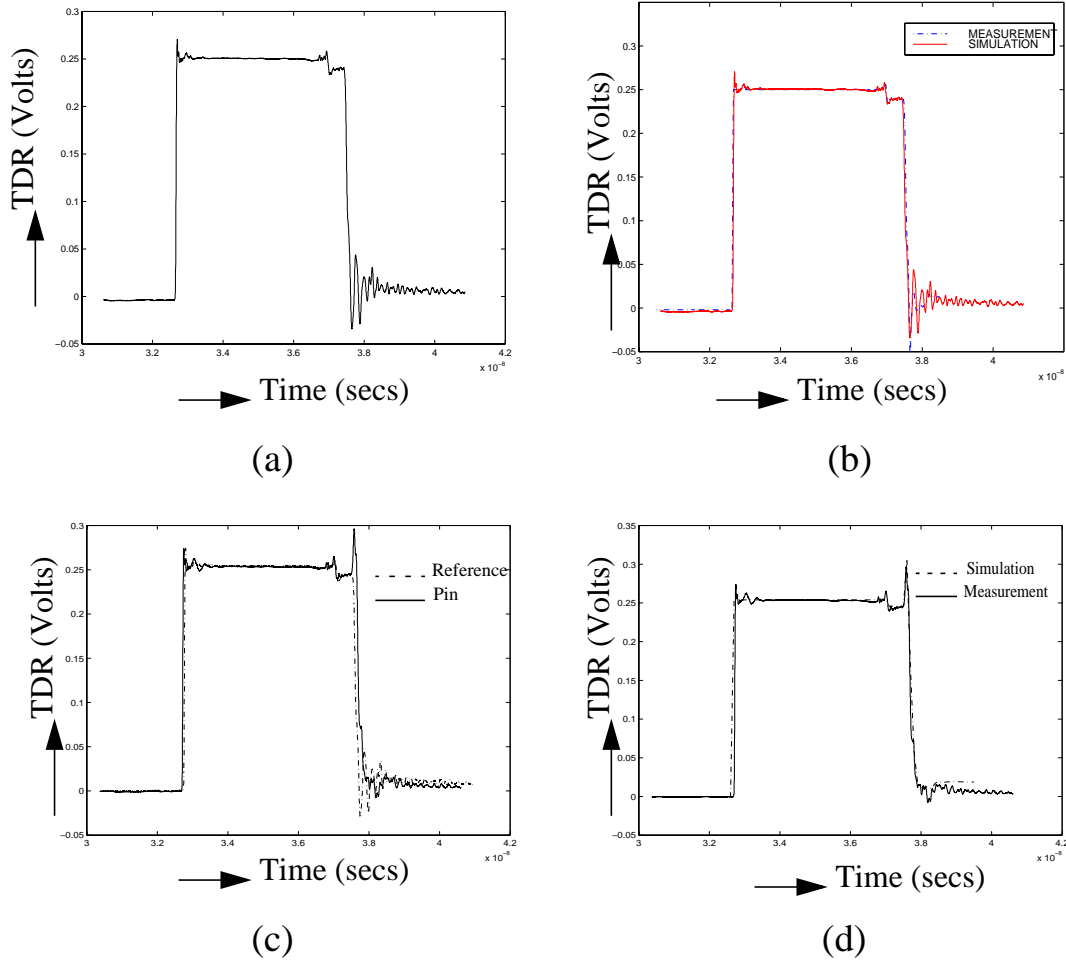


Figure 3.5 (a) Reference Short Measurement (b) Measurement vs. Simulation of the Reference Short (c) Reference Short Measurement Compared to the Shorted Pin (d) Measurement vs. Simulation of the Pin Response

3.2.3 Calculation of Self Capacitance Value

Once the value of L is known from the short-circuit measurement, the capacitance value is extracted from the open-circuit measurement. For low frequencies, the effect of L can be neglected and the TDR measurement can be used for calculating the capacitance

value. TDR measurements were made using the package with open ended pins as well as the reference open on the fixture for calibration (Figure 3.6(a)). Eq. 2.2 was used to calculate the capacitance of the pin as measured, as well as the reference open. For the reference measurement the capacitance was computed to be 0.76206 pF. The capacitance for pin1 of package 1 is 0.99373 pF. The capacitance of the pin with the effect of the fixture removed is 0.2317 pF. The correlation between the measured and simulated waveforms is shown in Figure 3.6(b). The L and C values generated for the packages have been compared to simulated data (provided by National Semiconductor Corp.) and were within 5-10% error.

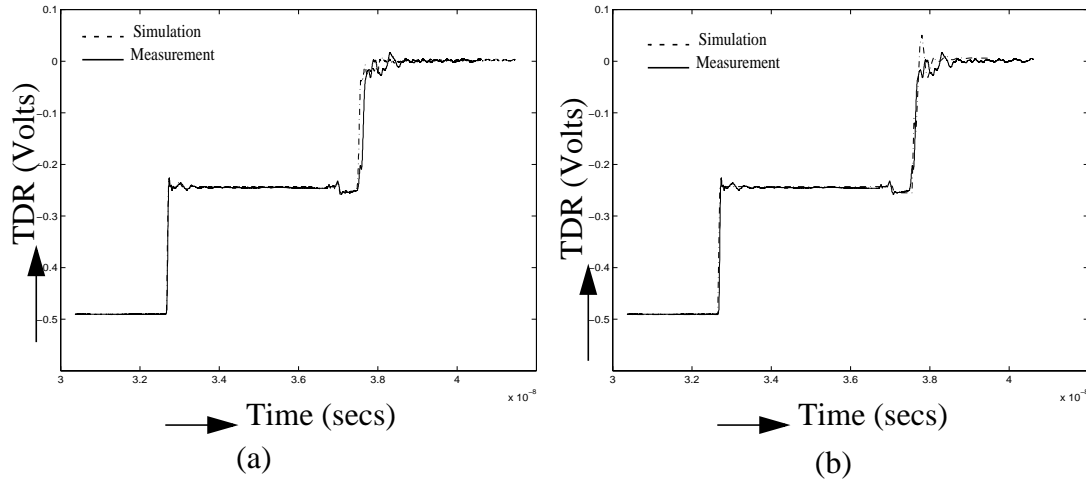


Figure 3.6 (a) Reference Open Measurement Compared to the Open Ended Pin
(b) Measurement vs. Simulation

3.2.4 Extension to Distributed Equivalent Circuits

Some of the packages with electrically long pins cannot be modeled accurately

using lumped elements. These pins are instead modeled using transmission lines with appropriate values of impedance (Z_{oi}) and time delay (T_{oi}), as shown in Figure 3.7.

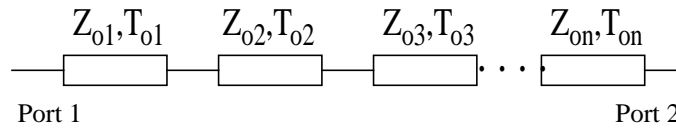


Figure 3.7 Pins Represented by Transmission Lines

The inductance value is calculated from the impedance profile and the capacitance is calculated from the admittance profile, using the calculated values for Z_{oi} and T_{oi} . The time windowing is done exactly the same way as in Section 3.2.1. But a predetermined time step of 20 ps is chosen and the values of impedance calculated. The smallest time step would be the most accurate, but this will require a large number of transmission lines to develop the model. To start with, 6-10 subdivisions are taken. If the simulations do not agree with the measurement for one or two test cases, more divisions are considered.

3.3 Extracted L, C Values

Six packages have been analyzed for the inductance and capacitance values. Depending on the symmetry of the package, measurements have been made on 1/4 of the total number of pins for the SSOP, SOP and MDIP packages. For the PQFP packages,

only 1/8 of the total number of pins have been characterized. The method described in this report gives accurate results for lumped element equivalent models and the simulations in SPICE are not very time consuming.

The values obtained for PQFP_48 are given in Table 3.1.

TABLE 3.1: L, C Values for PQFP_48

Pin	Inductance	Capacitance
	(nH)	(pF)
1	2.2	0.09
2	1.8	0.11
3	1.7	0.10
4	1.6	0.095
5	1.6	0.12
6	1.7	0.09

The values obtained for SOP_20 are given in Table 3.2.

TABLE 3.2: L, C Values for SOP_20

Pin	Inductance	Capacitance
	(nH)	(pF)
1	3.97	0.43
2	3.28	0.35
3	2.74	0.30
4	2.75	0.27
5	2.80	0.27

The values obtained for PQFP_80 are presented in Table 3.3.

TABLE 3.3: L, C Values for PQFP_80

Pin	Inductance	Capacitance
	(nH)	(pF)
1	4.535	0.49
2	4.01	0.40
3	3.79	0.41
4	3.75	0.30
5	3.57	0.31
6	3.22	0.25
7	3.52	0.21
8	3.37	0.2
9	3.41	0.19
10	3.39	0.19

The values obtained for MDIP are given in Table 3.4.

TABLE 3.4: L, C Values for MDIP_24

PIN	Inductance	Capacitance
	(nH)	(pF)
1	12.55	0.60
2	8.65	0.45
3	9.53	0.40
4	6.00	0.45
5	6.875	0.45
6	7.30	0.40

The values obtained for SSOP_56 are presented in Table 3.5.

TABLE 3.5: L, C Values for SSOP_56

Pin	Inductance	Capacitance
	(nH)	(pF)
1	5.125	0.48
2	4.485	0.40
3	3.645	0.40
4	3.515	0.39
5	2.87	0.36
6	3.03	0.32
7	2.97	0.32
8	2.58	0.25
9	2.75	0.25
10	2.95	0.23
11	2.90	0.21
12	2.98	0.23
13	2.86	0.18
14	2.87	0.18

CHAPTER IV

EXTRACTION OF BROAD BAND RATIONAL FUNCTION MODELS FROM TRANSIENT DATA

Simple equivalent circuits for connectors and RF packages have been constructed from TDR measurements in Chapter II and Chapter III. This was possible because the transient response of inductive, capacitive and resistive discontinuities could be identified from their time signatures. Planes and integrated components such as capacitors, inductors and resistors cannot be represented using simple equivalent circuits due to their complex behavior. One of the options would be to use rational functions to model these components. A pole is the most common type of singularity and its location in the complex plane with respect to other poles of the system can be used to understand the time domain response of the system. The resonant frequencies which cause oscillations can be shown explicitly using a rational function model or a macromodel. One of the objectives of the model to be developed is to capture the response of the planes using the dominant poles, so that the simulation time is minimal with the required accuracy.

Rational functions were used for modeling integrated passive devices and have been shown to be accurate up to 10 GHz [47]. Macromodels have also been used to characterize lossy thin film structures [48] and incorporated into SPICE-like tools [49]. Other methods such as Asymptotic Waveform Evaluation [50], Multipoint Pade

Approximation [51], Complex Frequency Hopping [52], and the Cauchy Method [53] have also been used to obtain dominant pole-zero (pole-residue) approximations for microwave circuits and interconnects. Except [53], the rest use simulated data. All of these methods use frequency domain data and have been quite successful in accurate modeling. Use of time domain data for extraction of mathematical models in the area of packaging has not been studied to a great extent, except for the work reported in [27]-[28]. Prony's method has been applied to transient data of transmission lines to construct a pole-residue model in [27]-[28]. Prony's method is not very stable for noisy data. The method used in this thesis is a pole extraction procedure that is much more stable than the Prony's. The effect of noise on the various pole extraction algorithms is discussed in Section 4.5.

The method used for the extraction of a pole-residue model is outlined in this chapter. As is well known, all pole-residue estimation methods are very sensitive to noise. To start with, the method is applied to simulated data to check the results for noiseless data. Next, white noise is introduced and the degradation in the performance is studied for varying Signal-to-Noise Ratios (SNR). The implementation of this algorithm on measured transient data is discussed in Chapter V.

4.1 Available Pole-Residue (Pole-Zero) Extraction Methods from Transient Data

The extraction of signal parameters from transient waveforms is a very old problem. The signals could be undamped sinusoids, closely spaced in frequency

compared to the reciprocal of the observation interval. This is the so called spectral resolution problem and has received considerable attention in signal processing and statistical time series analysis literature. When the spectrum estimation problem is primarily concerned with extracting sinusoids in noise, some recent methods based on the eigen-decomposition of the covariance matrix are among the best for high SNR situations [54]. These methods have also been popularized for Angle-of-Arrival (AoA) estimation in array processing. In this case the direction of an arriving plane wave gives a sinusoidal variation across the array, so the measurement of this "spatial" frequency amounts to direction finding.

Using Fourier techniques, frequencies closer than the reciprocal of time window cannot be resolved even with infinite SNR and the situation is worse if the signals are exponentially damped. Whereas in parameter estimation methods, such as the Prony and Generalized Pencil-of-Function (GPOF) methods, the resolution of closely spaced poles is limited primarily by the SNR in the data [55]. If the SNR is high enough, arbitrarily closely spaced poles can be resolved or accurately defined and can be used for parameter extraction from measured data.

A procedure for extracting sinusoids from transient electromagnetic data, involving a linear least squares fit to the data, which is closely related to Prony's method is described in [29]. A companion paper discussed the problems associated with Prony's method [30]. The problem with the basic Prony's method is that the accuracy of the poles extracted degrades with increasing noise. The improvement in performance of the SVD Prony method in the presence of noise is shown in [55]. Even better performance in the presence of noise is shown using the GPOF method in [56].

4.2 Extraction of Poles

Poles and residues are extracted from the transient output data using the Generalized Pencil of Function (GPOF) method. The GPOF approach directly finds the signal poles from the generalized eigenvalues of a matrix pencil instead of the conventional two step process where the first step involves the solution of a matrix equation, and the second step entails finding the roots of a polynomial as in the case of generalized Prony method [57].

An electromagnetic transient signal can be described by

$$y_n = \sum_{k=1}^M a_k e^{s_k \delta t n} \quad (4.1)$$

where $n=0,1,\dots,N-1$, a_k are the complex residues, s_k are the complex poles, M is the number of poles, and δt is the sampling interval. The data vector (y_n) , which is the TDR/TDT response of the DUT, is used to form matrices Y_1 and Y_2 as shown in Eq. 4.2.

$$Y_1 = [yy_0, yy_1, \dots, yy_{L-1}] \quad \text{and} \quad Y_2 = [yy_1, yy_2, \dots, yy_L] \quad (4.2)$$

where

$$yy_n = [y_n, y_{n+1}, \dots, y_{n+N-L-1}]^T$$

Y_1 and Y_2 are rewritten as

$$Y_1 = Z_1 A Z_2 \quad \text{and} \quad Y_2 = Z_1 A Z_0 Z_2$$

where

$$Z_1 = \begin{bmatrix} 1 & 1 & \dots & 1 \\ z_1 & z_2 & \dots & z_M \\ & & \dots & \\ z_1^{N-L-1} & z_2^{N-L-1} & \dots & z_M^{N-L-1} \end{bmatrix} \quad \text{and} \quad Z_2 = \begin{bmatrix} 1 & z_1 & \dots & z_1^{L-1} \\ 1 & z_2 & \dots & z_2^{L-1} \\ & & \dots & \\ 1 & z_M & \dots & z_M^{L-1} \end{bmatrix} \quad (4.3)$$

$$Z_0 = \text{diag}[z_1, z_2, \dots, z_M] \quad \text{and} \quad A = \text{diag}[a_1, a_2, \dots, a_M]$$

Based on the above decomposition of Y_1 and Y_2 , if Eq. 4.4 is satisfied, the poles are generalized eigenvalues of the matrix pencil $Y_2 - zY_1$. Here, z are the eigenvalues of the Z matrix in Eq. 4.6.

$$M \leq L \leq N - M \quad (4.4)$$

The SVD and pseudo-inverse (Y_1^+) of Y_1 are calculated as

$$Y_1 = U D V^H \quad \text{and} \quad Y_1^+ = V D^{-1} U^H \quad (4.5)$$

where U is unitary matrix consisting of the left hand singular values, V consists of the right hand singular values, and D is the diagonal matrix of singular values. Using the pseudo-inverse of Y_1 , Z matrix is calculated as shown in Eq. 4.6. Based on the M largest singular values of D , the poles are calculated as the eigenvalues of the Z matrix. The value of M is determined by the sudden drop in the magnitude of the singular value and is further explained in Section 4.4. Eq. 4.1 is solved in least squares sense to calculate the residues from the known DUT response and the poles extracted.

$$Z = D^{-1}U^H Y_2 V \quad (4.6)$$

4.3 Deconvolution of Input Waveform - Extraction of Device Residues

Poles and residues extracted in the previous section correspond to the step response of the DUT. Under the assumption that the poles of the device and the input do not cancel each other, all the required device poles will be extracted. But the residues thus extracted are not the residues of the device. This is because the TDR/TDT data represents the step response of the device and not its impulse response. The deconvolution of the input step source is therefore necessary.

The time domain technique's main handicap is deconvolution. This is due to the ill-conditioning of the deconvolution problem, which allows measurement noise to dominate the solution [9]. The accuracy of the extraction method depends on the

deconvolution method used.

Prony's method has been applied to transient data of transmission lines to construct a pole-residue model in [27] and deconvolution was carried out according to Eq. 4.7

$$S_{11}(j\Omega) = \frac{\text{FFT}(\text{diff}(V_{\text{TDR}}[n]))}{\text{FFT}(\text{diff}(V_i[n]))} H(j\Omega) \quad (4.7)$$

where V_{TDR} and V_i are the device response and the input source respectively. The difference function (diff) was applied to each of the signals to obtain a time-limited signal to which the FFT could be applied. The smoothing filter $H(j\Omega)$ was used to window out noise, because both spectra could be close to zero causing the ratio of the two signals to vary unpredictably. The main disadvantage of this deconvolution process is the availability of an appropriate smoothing filter, just to filter out noise and not the signal itself. These filters would be dependent on the DUT.

In this research, deconvolution is performed recursively using the poles obtained using GPOF, the DUT response, and the input. This method has not been applied for deconvolution in the available literature. No filtering or stabilization function has been found necessary. The results obtained are subjected to error analysis with varying parameters such as the time interval and the time window and the method consistently produced good results.

The convolution integration at time t_{n+1} as shown in Eq. 4.8 can be written as Eq. 4.9 where the impulse response is estimated using poles and residues. Using trapezoidal rule for integration, the recursive convolution formulation is shown in Eq. 4.10 [58].

$$y_s(t_{n+1}) = v_s(t) \otimes h(t) \Big|_{t=t_{n+1}} = \int_0^{t_{n+1}} v(\tau)h(t-\tau)d\tau \quad (4.8)$$

where $y(t)$ is the step response, $v_s(t)$ is the step input and $h(t)$ is the impulse response

$$y_s(t) = \int_0^{t_{n+1}} v(\tau) \left[\sum_{k=1}^M a_k e^{s_k(t_{n+1}-\tau)} \right] d\tau \quad (4.9)$$

where a_k are the residues and s_k are the poles of the impulse response, M is the number of poles.

$$y_s(t) = \sum_{k=1}^M \left[a_k e^{s_k h_n} \int_0^{t_n} v(\tau) e^{s_k(t_n-\tau)} d\tau + \frac{h_n}{2} a_k \left[v(t_n) e^{s_k h_n} + v(t_{n+1}) \right] \right] \quad (4.10)$$

where $h_n = t_{n+1} - t_n$ is the time step.

The device poles (s_k) are extracted using GPOF, we have the measured data for the device response ($y(t)$) and input waveform ($v(t)$). The only unknowns are a_k . So we can rewrite Eq. 4.10 as

$$\mathbf{R} = \mathbf{A}^{-1} \mathbf{Y}^T \quad (4.11)$$

where $\mathbf{R} = [a_1, a_2, \dots, a_M]$, $\mathbf{Y} = [y(t_1), y(t_2), \dots, y(t_n)]$ and

$$\mathbf{A} = \sum_{n=1}^{N-1} \sum_{k=1}^M \left[e^{s_k h_n} A(n, k) + \frac{h_n}{2} \left[v(t_n) e^{s_k h_n} + v(t_{n+1}) \right] \right] \quad (4.12)$$

Using this procedure, correct device poles and residues can be calculated from the transient data.

4.4 Extraction of Poles and Residues from Simulated TDT/TDR Data

The GPOF method and recursive deconvolution have been used to extract the rational function models from simulated data in this section. The test case used here is a 6 layered, 5.3” x 5.3” Printed Circuit Board (PCB) plane as shown in Figure 4.1 [63]. The second layer is a plane that is referenced to the fifth layer which acts as a ground plane

for the measurements discussed. The structure has multiple SMA connectors mounted for pulse propagation on the signal layers. It has been characterized as a two-port device, with the diagonal port location (Port 1 & Port 2). The first resonance is observed at ~500 MHz. This plane can be of practical use up to this frequency. For modeling purposes, the macromodel developed for 2 GHz has been used [63]. Based on the effective dielectric constant of this board of ~4.5, 2 GHz frequency bandwidth translated to approximately 2 times the wavelength. This frequency is wide enough to include many resonances and hence is an ideal case to check to see if the required poles are extracted.

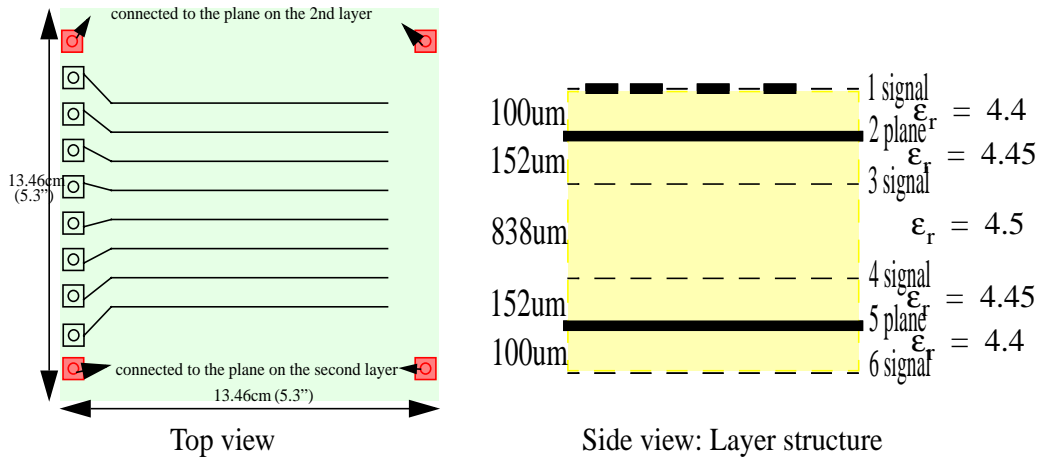


Figure 4.1 Top View and the Layer Information of the PCB Plane Structure

The PCB plane structure has been analyzed using analytical expressions and the two-port rational functional model has been developed in [63]. The coefficients of the 20th order model have been used to get information about the poles and residues of the DUT using partial fractions and are listed in Table 4.1.

Table 4.1: Poles and Residues of the Original Macromodel

	Real(Pole)	Imag(pole)	Real(residue)	Imag(residue)
1	-7.3852379e+01	0.0000000e+00	-4.4882791e-01	0.0000000e+00
2	-2.4102337e-01	1.3626434e+01	5.4934060e-02	-1.4131943e-02
3	-2.4102337e-01	-1.3626434e+01	5.4934060e-02	1.4131943e-02
4	-1.3027768e-01	1.1964157e+01	-1.2437242e-01	8.9757455e-03
5	-1.3027768e-01	-1.1964157e+01	-1.2437242e-01	-8.9757455e-03
6	-1.5828050e-01	1.0484690e+01	1.5139377e-01	1.5014055e-02
7	-1.5828050e-01	-1.0484690e+01	1.5139377e-01	-1.5014055e-02
8	-6.1211348e-02	9.9673836e+00	-6.2906336e-02	6.6924025e-03
9	-6.1211348e-02	-9.9673836e+00	-6.2906336e-02	-6.6924025e-03
10	-8.1535128e-02	9.3968150e+00	8.2119229e-02	-3.0975715e-02
11	-8.1535128e-02	-9.3968150e+00	8.2119229e-02	3.0975715e-02
12	-1.8338221e-01	7.4305743e+00	-1.8121942e-01	1.6891444e-02
13	-1.8338221e-01	-7.4305743e+00	-1.8121942e-01	-1.6891444e-02
14	-1.0006729e-01	6.6389733e+00	9.9108060e-02	-1.0341387e-02
15	-1.0006729e-01	-6.6389733e+00	9.9108060e-02	1.0341387e-02
16	-1.1636520e-01	4.7020339e+00	1.1426692e-01	-2.1696957e-02
17	-1.1636520e-01	-4.7020339e+00	1.1426692e-01	2.1696957e-02
18	-1.2606043e-01	3.3207962e+00	-1.2278344e-01	1.1040737e-02
19	-1.2606043e-01	-3.3207962e+00	-1.2278344e-01	-1.1040737e-02
20	-6.5663043e-02	0.0000000e+00	6.4952199e-02	0.0000000e+00

The poles and residues listed in Table 4.1 were then used for simulating the transient response. The propagated pulse can be represented as [27]

$$V_{\text{TDT}}(n) = S_{21}(n) \otimes V_i(n) \quad (4.13)$$

where $V_{\text{TDT}}(n)$ is the transmitted voltage and $V_i(n)$ is the input. The recursive convolution formulation using Eq. 4.10 is

$$V_{\text{TDT}}(t_{n+1}) = \sum_{k=1}^M \left[e^{s_{21k} h_n} V_{\text{TDT}k}(t_n) + \frac{h_n}{2} a_{21k} \left[V_i(t_n) e^{s_{21k} h_n} + V_i(t_{n+1}) \right] \right] \quad (4.14)$$

where

$$V_{\text{TDT}k}(t_n) = \int_0^{t_n} a_{21k} V_i(\tau) e^{s_k(t_n - \tau)} d\tau \quad (4.15)$$

is the output value due to each pole calculated in the previous time step. Hence the time domain response can be computed using past history, bypassing the explicit convolution, which significantly saves computational time [58]-[59].

The standard input of 11801B DSO and the SD24 sampling head is a 250 mV, 35 ps step input. Considering the rise time degradation, the effective rise time was 60 ps and

is discussed in Section 5.2. A step input with the same amplitude and 60 ps rise time was convolved with the poles and residues to obtain the step response of the device. The input step pulse and the macromodel response are shown in Figure 4.2.

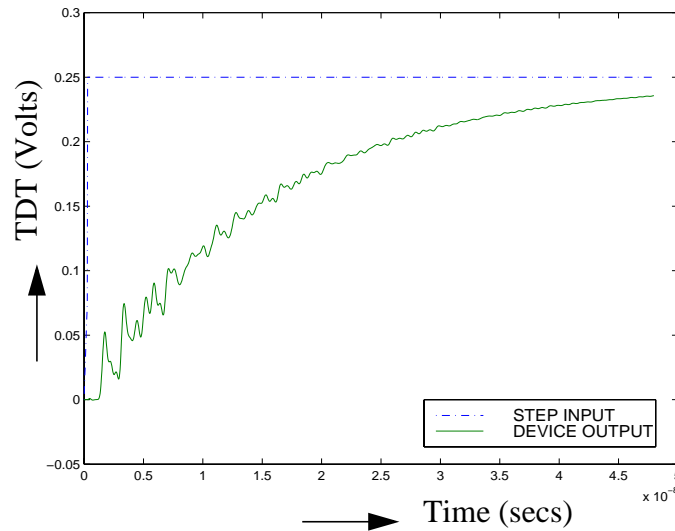


Figure 4.2 Device and Reference Waveform Used for Extracting S_{21} Model

The transient response is processed for poles using GPOF. The number of poles required to approximate the given output waveform is determined by the sudden decrease in the singular values of the diagonal matrix, D computed in Eq. 4.5. For the calculation of poles from the TDT waveform, the singular values are as listed in Table 4.2. The magnitude of the 32nd element is less than the 31st element by an order of 1000. This clearly demarcates that the poles calculated from 32nd value onwards are not very dominant and can be neglected with a small error. Therefore, 31 poles are taken and a least square fit is used to calculate the residues corresponding to the step input.

Table 4.2: Singular Values of the D Matrix

Number	Singular value
<i>1</i>	<i>149.2449224241</i>
<i>2</i>	<i>13.41670927210</i>
<i>3</i>	<i>1.28835348915</i>
<i>4</i>	<i>1.270584899667</i>
<i>5</i>	<i>0.826325544383</i>
<i>6</i>	<i>0.771308461265</i>
<i>7</i>	<i>0.658695677275</i>
<i>8</i>	<i>0.654593707644</i>
<i>9</i>	<i>0.442098456275</i>
<i>10</i>	<i>0.441138057886</i>
<i>11</i>	<i>0.399470460560</i>
<i>12</i>	<i>0.395158267445</i>
<i>13</i>	<i>0.312885549193</i>
<i>14</i>	<i>0.298898327011</i>
<i>15</i>	<i>0.231069815456</i>
<i>16</i>	<i>0.228826009304</i>
<i>17</i>	<i>0.163110744010</i>
<i>18</i>	<i>0.162434773744</i>
<i>19</i>	<i>0.046467904110</i>
<i>20</i>	<i>0.045047324315</i>
<i>21</i>	<i>0.005686916127</i>
<i>22</i>	<i>0.003211127730</i>
<i>23</i>	<i>0.001719126384</i>
<i>24</i>	<i>0.001002435939</i>
<i>25</i>	<i>0.000689477046</i>
<i>26</i>	<i>0.000543332858</i>
<i>27</i>	<i>0.000444759500</i>
<i>28</i>	<i>0.000388433848</i>
<i>29</i>	<i>0.000347705987</i>
<i>30</i>	<i>0.000323976892</i>
<i>31</i>	<i>0.000309988752</i>
<i>32</i>	<i>0.000000185404</i>
<i>33</i>	<i>0.000000185328</i>

Recursive deconvolution is used next to calculate the actual residues of the DUT. Not all the poles extracted using GPOF are required to have negative real parts to assure that the system is passive. The way the positive poles are taken out is by checking for the magnitude and calculating the residues only for the poles with negative real parts. This is done using Eq. 4.11. The order of the system to start with was 20. A clear cut demarcation of the eigenvalue gives 31 poles. This model can be good up to a much higher frequency. Because of our interest in a model up to 2 GHz, poles which correspond to higher frequencies are eliminated. If carefully checked, there is a order of magnitude difference between 20th and 21st eigenvalue. These poles were then eliminated and the 20 pole model response compared with 31 pole model response which resulted in less than 0.1 % rms error. Thus the order of the rational function model can be approximated to 20 and the corresponding poles and residues are listed in Table 4.3.

The poles and residues thus obtained are plotted in frequency domain using the following equation

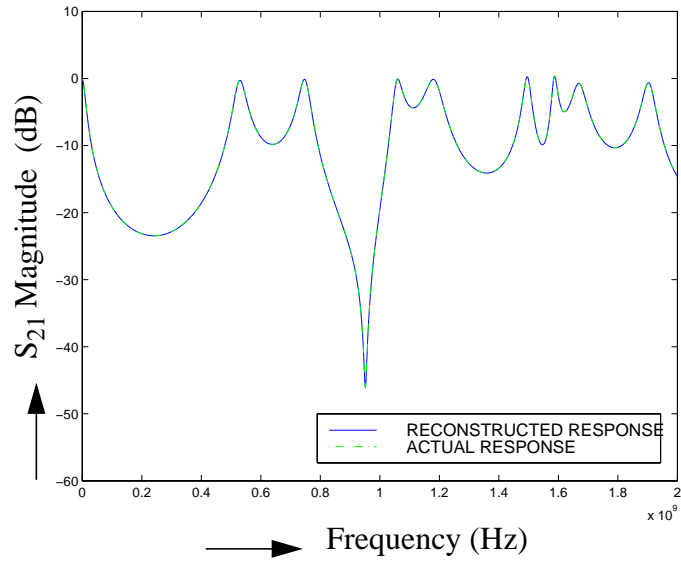
$$S_{21}(f) = \sum_{k=1}^M \frac{a_k}{2\pi f - s_k} \quad (4.16)$$

where f is the frequency, a_k are the residues, s_k are the poles and M is the number of poles used for the approximation. The results obtained for S_{21} are shown in Figure 4.3, where the reconstructed S_{21} magnitude and phase is compared with the macromodel. The

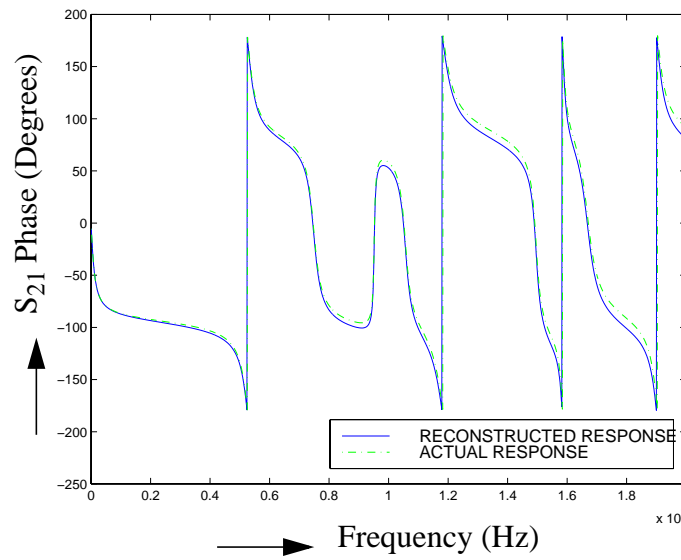
rms error between the reconstructed response and original response is ~0.15 %.

Table 4.3: Extracted Poles and Residues from Simulated TDT Data

	real(pole)	imag(pole)	real(residue)	imag(residue)
1	-2.4045656e-01	1.3626881e+01	4.4483775e-02	-1.3545612e-02
2	-2.4045656e-01	-1.3626881e+01	4.4483775e-02	1.3545612e-02
3	-1.3034467e-01	1.1964122e+01	-1.2183034e-01	3.6471737e-02
4	-1.3034467e-01	-1.1964122e+01	-1.2183034e-01	-3.6471737e-02
5	-1.8716507e-07	0.0000000e+00	8.4877691e-06	-7.8514618e-18
6	-6.5661877e-02	0.0000000e+00	6.4972903e-02	3.7932531e-17
7	-1.2604938e-01	3.3207965e+00	-1.2206784e-01	1.8034280e-02
8	-1.2604938e-01	-3.3207965e+00	-1.2206784e-01	-1.8034280e-02
9	-1.1637847e-01	4.7020358e+00	1.1265415e-01	-2.8505379e-02
10	-1.1637847e-01	-4.7020358e+00	1.1265415e-01	2.8505379e-02
11	-1.0006257e-01	6.6389900e+00	9.8303013e-02	-1.8603577e-02
12	-1.0006257e-01	-6.6389900e+00	9.8303013e-02	1.8603577e-02
13	-1.8336604e-01	7.4305384e+00	-1.7875922e-01	4.0700694e-02
14	-1.8336604e-01	-7.4305384e+00	-1.7875922e-01	-4.0700694e-02
15	-1.5823558e-01	1.0484754e+01	1.4970593e-01	-3.3259623e-03
16	-1.5823558e-01	-1.0484754e+01	1.4970593e-01	3.3259623e-03
17	-6.1236866e-02	9.9673791e+00	-6.0536830e-02	1.7950497e-02
18	-6.1236866e-02	-9.9673791e+00	-6.0536830e-02	-1.7950497e-02
19	-8.1513813e-02	9.3968268e+00	7.7533357e-02	-3.9858337e-02
20	-8.1513813e-02	-9.3968268e+00	7.7533357e-02	3.9858337e-02



(a)



(b)

Figure 4.3 Comparison of Reconstructed and Actual S_{21} (a) Magnitude (b) Phase

The procedure for extracting a model for S_{11} is similar to S_{21} . The reflected waveform (Figure 4.4) is simulated using the recursive convolution formulation of Eq. 4.17,

$$V_R(n) = S_{11}(n) \otimes V_i(n) \quad (4.17)$$

where V_R is the reflected voltage, S_{11} is the macromodel and V_i is the input.

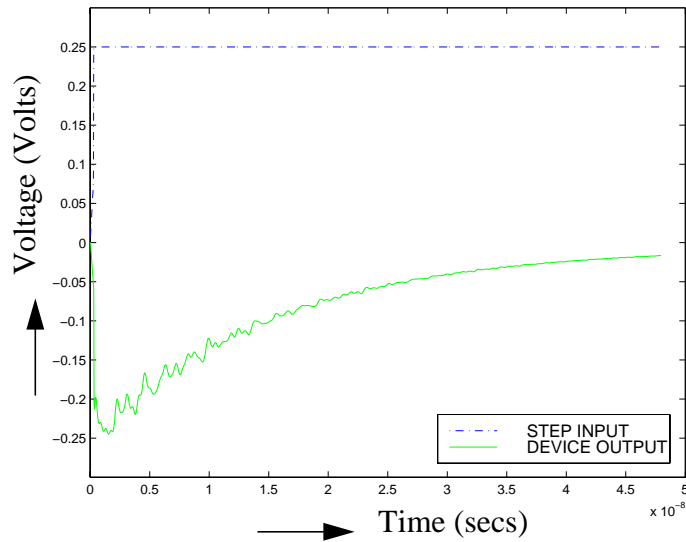


Figure 4.4 Device and Reference Waveform used for Extracting S_{11} Model

Using GPOF for extracting S_{11} poles from the TDR waveform, 31st singular value is 0.0000055374 and 32nd singular value is 0.00000003061, which is less by two

orders of magnitude. Thus 31 poles were taken and recursive deconvolution was used to calculate residues. The order was further reduced to 20, following the same procedure as S_{21} model. These poles and residues were used for plotting S_{11} magnitude (Figure 4.5) and S_{11} phase (Figure 4.6). Both the plots are compared with the macromodel results and the error is less than $\sim 1\%$. The error is slightly higher for S_{11} compared to S_{21} . This was found to be the result of time resolution limitations. When the time step was reduced to 5ps from 10ps, the error was reduced to $\sim 0.2\%$. This could be because of the falling edge in the reflected waveform which has to be modeled for the case of S_{11} . This tells us that more points are needed to capture the fall time. But we are limited to 10 ps in this research because of the equipment set-up, as is discussed in Section 6.2.

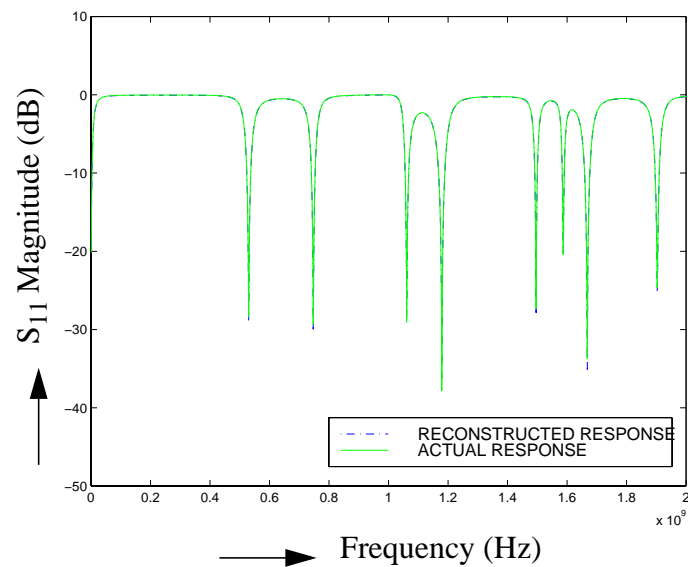


Figure 4.5 Comparison of Reconstructed and Actual S_{11} Magnitude

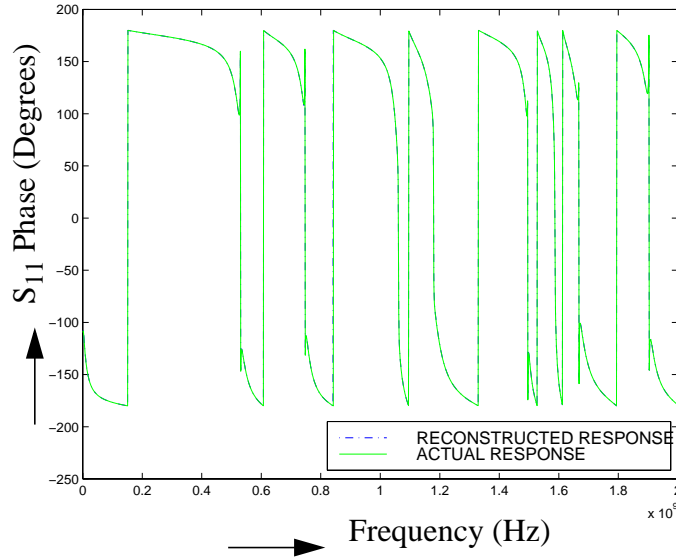


Figure 4.6 Comparison of Reconstructed and Actual S_{11} Phase

4.5 Sensitivity of the Method to Noise

The performance algorithms used for the estimation of poles and residues of a transient waveform, such as Maximum Likelihood (ML) method, the Backward Linear Prediction (BLP) Method, the Modified Prony (MP) Method, the Tufts-Kumaresan (TK) method, and the Improved Pisarenko (IP) method have been compared to the Cramer Rao (CR) bound in [55]. The waveform used for the extraction of poles and residues was a transient generated using two sinusoids and the SNR was varied from 30 dB to 0 dB. The mean square estimation error for the frequencies of the two sinusoids, their damping factors, and their amplitudes were compared. The ML method was not found advantageous for damped sinusoids but worked much better than the TK or IP methods

for undamped sinusoids. For exponentially damped sinusoids BLP methods did not give good estimates, even at 40 dB SNR. The TK and IP methods perform slightly better than the MP method [55]. We are interested in exponentially damped sinusoids in this work and hence the TK or IP methods are more suited.

Extensive perturbation analysis has been done for Polynomial approach and the pencil approach [56]. TK and IP methods are referred to as the polynomial approach. Only the case where the noise is sufficiently low, for which the first order perturbation approximation is valid, has been considered. The transient under analysis consisted of two sinusoids as before. Variances in the values of the two frequencies, associated damping factor, and the amplitudes have been tabulated. It has been shown that the pencil approach tolerates much more SNR than polynomial approach.

The GPOF method has been compared to the CR bound [57]. Around $L=N/2$, the performance of the GPOF method is very close to the optimal bound, i.e., the Cramer-Rao Bound. Ref [57] has shown that GPOF performs better than the least square Prony method. The SVD Prony method performs better than the LS Prony and the TLS Prony method. GPOF method is less sensitive to noise than the SVD Prony method [57].

Theoretically GPOF has been proven to perform better than the other methods for the case of two sinusoids. We are concerned here with estimation of ~ 20 sinusoids. Even though the poles and residues can be estimated for the step response, our main intention is to get the device impulse response which includes the recursive deconvolution procedure too. A simple study of the effect of the noise on the combination of GPOF and recursive convolution has been done in terms of root mean square error.

To test the signal-noise subspace method, white noise was generated and added to the TDR/TDT data, according to Eq. 4.18 [54]

$$V_{\text{noise}} = V_{\text{TDT}} + \frac{\sigma_n}{\sqrt{2}}[W_{\text{noise}}] \quad (4.18)$$

where V_{noise} is the corrupted data to be analyzed, V_{TDT} is the simulated device response, W_{noise} is random noise with zero mean and variance of one, and σ_n determines the SNR.

The SNR is quantified using

$$\text{SNR}_{\text{dB}} = 20 \cdot \log_{10} \left(\frac{a_i}{\sigma_n} \right) \quad (4.19)$$

where a_i is the amplitude of the sinusoid being determined.

Because V_{TDT} is being estimated by M poles and residues, there is no method of identifying which pole gets affected the most. The best method is to study the error in each of the poles and the corresponding residues. To get an approximate idea, the residue with the smallest value has been studied. The effect of the same value of σ_n would translate to a larger value of SNR for relatively larger residues. The residue with the smallest value would be the worst case analysis. The residues being considered are the ones calculated using least square approximation from the device step response.

Considering the fact that the smallest residue need not correspond to a dominant pole, a quick comparison was done. The pole corresponding to this residue was removed from the set of poles and S_{21} remapped in frequency, resulting in an rms error of ~10.26% compared to the actual response. With this pole included the error in S_{21} response was 0.15%. This tells us that the pole-residue pair is indeed dominant and is required to get the correct device response. This smallest residue value of 0.00329 was used as a measure for the white noise being introduced.

Eq. 4.19 was used to calculate SNR values shown in Table 4.4 for the a_i value of 0.00329. The rms error in reconstructing S_{21} without any noise introduced was ~0.15 %. Beyond 10 dB SNR the error deteriorates.

Table 4.4: Effect of White Noise

SNR (dB)	RMS error
50	0.0046334452302
40	0.00464927442124
30	0.00467213388042
25	0.00415591416176
20	0.00570460413990
15	0.01581700153816
10	0.07786722719278
8	0.11974619718804
5	0.28725089512918

The error due to the introduction of white noise in the transient waveform is shown in Figure 4.7. From the above simulations, it is clear that the error gets worse for a SNR of 10 dB or less. This behavior is very similar to the error performance of SVD Prony [55] and GPOF [56].

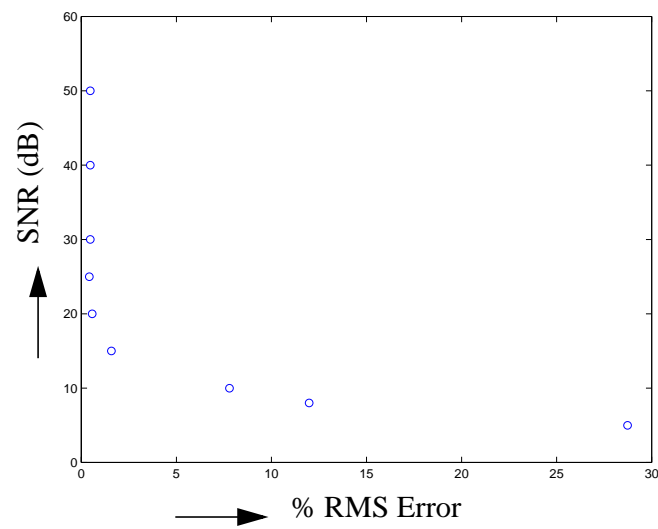


Figure 4.7 Error Due to White Noise

CHAPTER V

EXTRACTION OF RATIONAL FUNCTIONS FROM TDR/TDT MEASUREMENTS

Poles and residues have been extracted from the transient data using Prony's method [29]-[30], SVD Prony method [55], and the GPOF method [56]. The transient data used was simulated data and the applicability of the methods for actual measured data is not discussed. In this thesis, we are interested in extracting macromodels directly from Time Domain Reflectometry (TDR) and Time Domain Transmission (TDT) measurements. The primary distinction between previously reported work and the results reported here is that the data were obtained by measurements as opposed to theoretical analysis or computer simulation. This is an important distinction since one generally makes assumptions in the mathematical model which are not completely realized in an experimental implementation. The results obtained from simulated results discussed in Section 4.4 are different from measured data for the test vehicle considered and are discussed in Section 5.11. Hence no attempt has been made to compare the values of the poles or the simulated response with the results obtained from experiments. All comparisons have been made between the extracted response from time domain measurements and frequency domain measurements.

5.1 Measurement Set-up

The design of the test vehicle was discussed in Section 4.4. The fabricated test vehicle is shown in Figure 5.1. The two ports are defined on the diagonal of the 5.3" x 5.3" PCB board (Figure 5.1). The reference planes for the measurement are set at the edge of SMA connectors for all the measurements. The standard set-up using the internal 250 mV step source of 11801B digital sampling oscilloscope with a SD-24 sampling heads has been used for the TDT/TDR measurements (Figure 5.2).

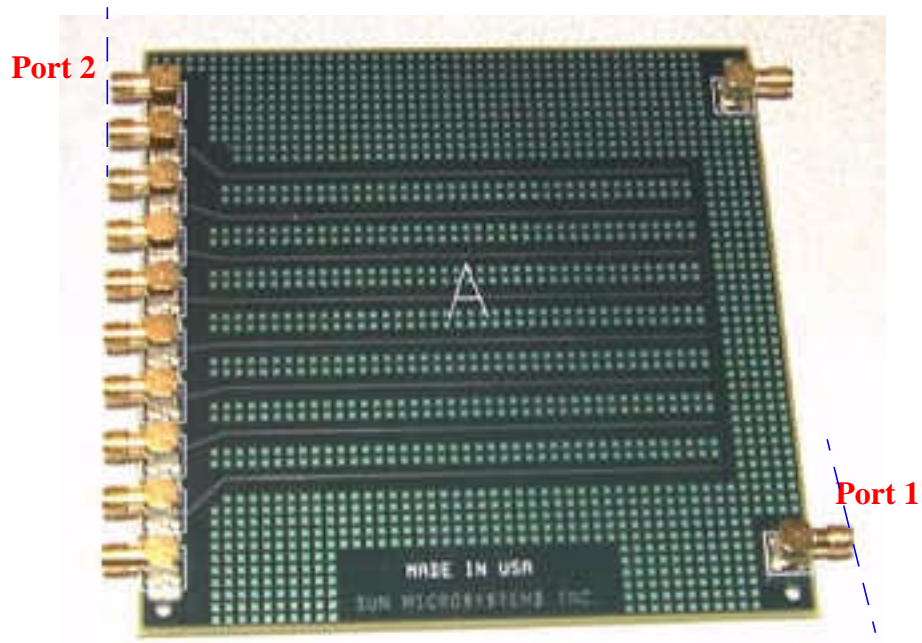


Figure 5.1 The Fabricated Test Vehicle

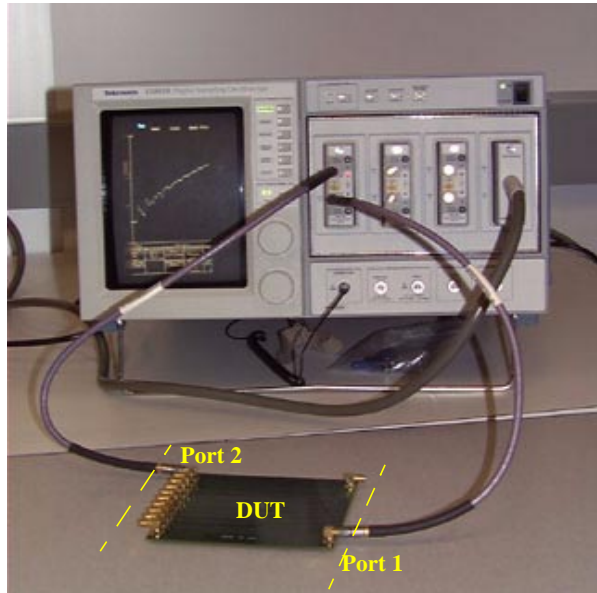


Figure 5.2 Measurement Set-up for S_{21} Device Measurement

5.2 Rise Time Measurement

The rise time determines the bandwidth of the model to be developed and has to be determined first to make sure we are using the correct pulse source. If a long cable is present between the TDR output and the reference plane at which the measurements are to be made, the effective rise time is governed by Eq. 2.3. This incorporates the rise time degradation due to the cable. A short standard is connected to the cable at one end and a TDR measurement in reflection mode is used to measure the rise time of the pulse at the reference plane. The accuracy of this measurement depends on the quality of the short standard. The rise time measured between 5% and 95% is ~ 38.9 ps (Figure 5.3). The approximate bandwidth that can be obtained using this step input is ~ 9 GHz and this is well beyond the 2.5 GHz bandwidth we are interested in.

It can be observed from Figure 5.3 that the rise time (measured between 0 to 100%) is ~60 ps. This is the value of the rise time that has been used for simulations in Chapter IV. It can also be observed from Figure 5.3 and Table 5.1, that the reflection coefficient is ~-0.01 where it should have been 0.0, which shows that there is a small error. This measurement was made taking into account both the internal calibration and the baseline correction. The error could be a combination of the resolution error as well as the effect of the cable and the connection to the short standard.

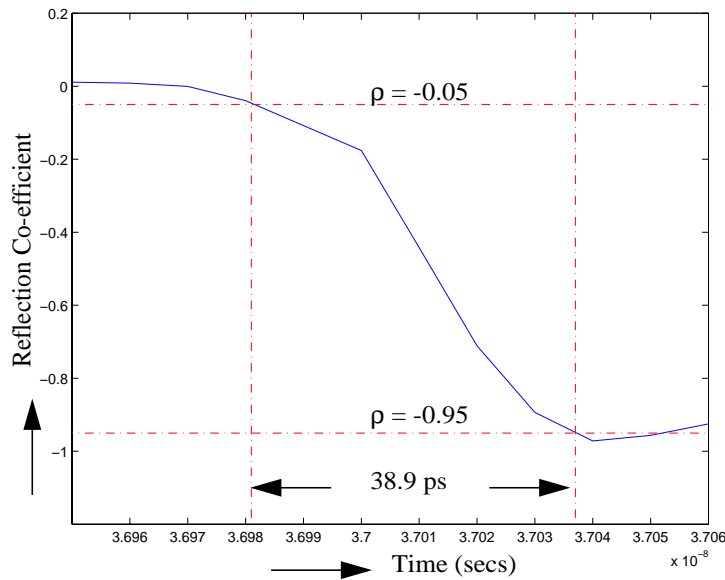


Figure 5.3 Rise Time Determination Using a Short Standard Measurement

5.3 Timing Reference Measurement

The DUT response is demarcated because of the 50 Ω cables used for measurement and is similar to the time windowing referred to in Chapter III. The

reflection co-efficient is close to zero and starts dropping to -1 around 36.97 ns (Figure 5.4). The value of ρ is shown in Table 5.1. The first time step to have a negative value of ρ is taken as the start time for the device response as well as the reference waveform. Since, the reference time depends on the resolution and jitter, the reference waveform needs to be measured each time the measurement parameters are changed.

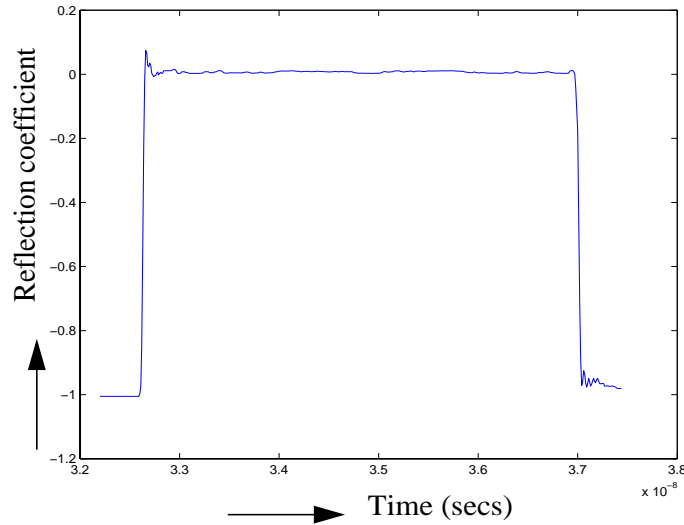


Figure 5.4 Short Standard Measurement

Table 5.1: Reflection Coefficient at the Falling Edge

Time (ns)	Reflection coefficient
36.95	0.0110309
36.96	0.00853088
36.97	-0.000594125
36.98	-0.0395004
36.99	-0.176063

5.4 TDT Measurement

The rational function models for transfer scattering parameters S_{12} and S_{21} are obtained from TDT measurements. The device response is required for the extraction of poles and the reference waveform is used for deconvolution. The measurements required for the extraction of S_{21} and S_{12} models are discussed in this section.

5.4.1 Measurements for S_{21} Model

5.4.1.1 Device Response

The device response is measured at port 2 when port 1 is excited by the 250 mV step input (Figure 5.2). The start time of the response is set by the time reference in Section 5.3. The timing interval is 10 ps which is the minimum possible using the set-up. The end time is taken so that the oscillations die down and a steady state behavior is attained. This approximately translates to a 30 ns time window. The number of averages for each measurement to reduce the effect of drift was taken as 64. All these numbers correspond to the optimum parameters for this measurement and are further discussed in Section 6.2, Section 6.3 and Section 7.2.1. It was best to acquire 512 points each time over a time window of 512 ps/div with a 10 ps time interval. The vertical resolution taken was 30 mV/div so as to get the whole waveform in the assigned DSO vertical scale.

5.4.1.2 Reference Waveform

The DUT was replaced with a thru standard for measuring the reference

waveform. The measurement parameters are the same as the device response. The waveforms are as shown in Figure 5.5.

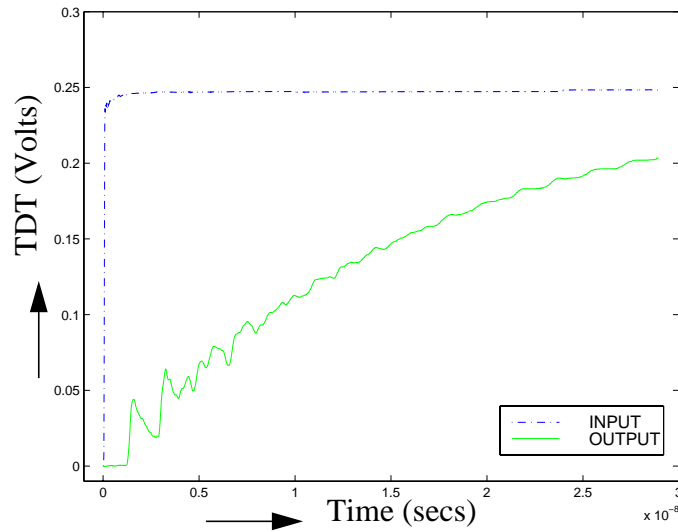


Figure 5.5 Device Response (Output) and the Reference Waveform (Input) Used for Extracting S_{21} Model

The reference waveform has information about the rise time of the input source and hence is used for deconvolution. Ideally the input to the device for the TDT measurement would have rise time degradation only due to one cable. But the response itself would have twice this rise time degradation because of the cable from the output port to the sampling head. This method would work as long as this degradation is minimal and contributes much less than the error due to the jitter and interchannel time variation as listed in Section 7.4. Otherwise a thru measurement with just one cable can be made and a delay due to one cable added to obtain the reference waveform.

As can be seen from the device and reference waveform, it is important to have the correct short reference time. It is not a significant problem if the timing reference is shifted to the left. This would eventually be deconvolved with the reference waveform, so the response will not be affected. If noise exists in this extra time window, more spurious poles could be extracted using GPOF. But if the timing reference is wrongly shifted to the right, the rise time of the step response will not be accounted for. This will lead to error because the correct input waveform is not used for deconvolution.

5.4.2 Measurements for S_{12} Model

The device is not symmetric in the sense that there are a row of SMA connectors on one side and only two on the other side (Figure 5.1). Hence, the S_{12} response will be different from S_{21} and needs to be extracted to get a complete two-port scattering parameter model. For extracting the S_{12} model, measurements for the device and reference waveforms were made with ports 1 & 2 switched. The device response and reference waveforms were measured at port 1 when port 2 is excited by the 250 mV step input used for extracting S_{12} . The criteria for choosing the reference time, timing interval, and time window is same as S_{21} .

5.5 TDR Measurements for S_{11} & S_{22} Model

Scattering parameters (S_{11} and S_{22}) can be extracted from TDR measurements.

The same channel of the SD-24 sampling head is used for launching the 250 mV pulse and measuring the reflected waveform. For S_{11} extraction, Port 1 is used for measurement and port 2 is terminated in a 50Ω load. The approximate propagation time from port 1 to port 2 is 8.27 ns (dielectric constant = 4.5, effective distance between the ports = $5.3'' \times \sqrt{2}$). No reflections due to a imperfect load will appear earlier than 16.54 ns. The response does not reach steady state in this period of time. A time window of 30 ns with a 10 ps time interval is optimum as discussed in Section 5.4.1.1. So care should be taken to use a properly calibrated load.

The TDR waveform is the sum of incident and reflected waveforms. The measured waveform has its DC level at 250 mV. A matched load waveform would also be at 250 mV beyond one delay (the TDR waveform actually has two way delay). In the time window of interest, the reflected waveform ($V_r = V_{TDR} - V_{matched}$) is nothing but the TDR waveform shifted by the -250 mV level. This is how the reflected waveform has been considered in this work. This should not be a problem as long as a cable (constant impedance path) is inserted between the TDR channel and the device port. The same waveform can be obtained by subtracting the reflected waveform and the matched waveform on the scope. This involves the use of adjacent channels and this would lead to an inter-channel drift of ~ 10 ps. The matched waveform would also be noisy. The error due to this subtraction can be double in the worst case and does not relate to the error in the actual reflected waveform.

The reference waveform taken is the same as in Section 5.4.1.2. The device and reference waveform for extracting S_{11} are shown in Figure 5.6. For the S_{22}

measurements, a pulse is propagated onto port 2 and the reflection measurement is made on the same channel with Port 1 terminated in a 50Ω load. The measurement parameters are similar to S_{11} .

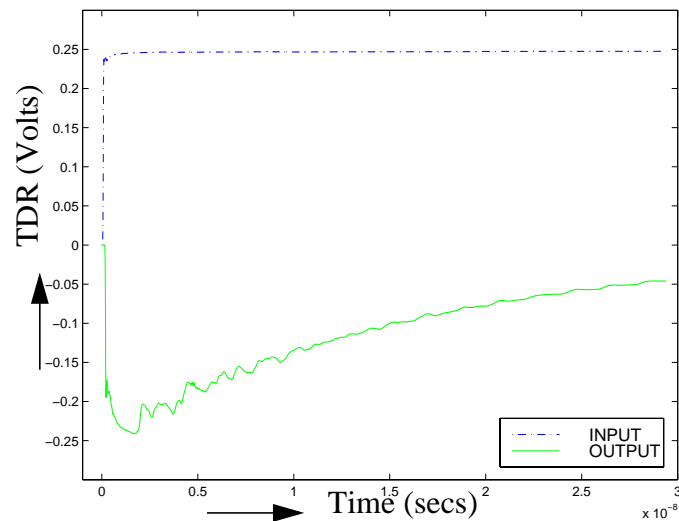


Figure 5.6 Device Response (Output) and the Reference Waveform (Input) Used for Extracting S_{11} Model

5.6 Extraction of Poles

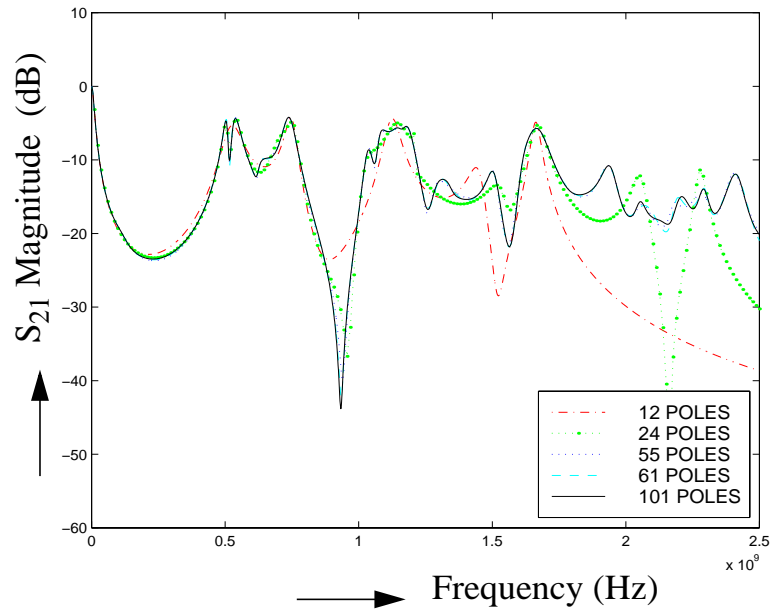
For high SNR simulated data, there is a clear demarcation between the signal and noise components as discussed in Section 4.4. But for actual measured data, additional information such as allowable error and an upper estimate of the poles is used. The singular values of the D matrix (Eq. 4.5) are filtered using the ratio of the maximum singular value and the cut-off value. In this investigation, a ratio of $D(1)/10000$ was found to be optimum. Beyond that the number of poles increases drastically for a small

variation in the cut-off value. It can be seen from Table 5.2 that the poles have increased from 77 to 372 for a decrease in the singular value ratio from $D(1)/10000$ to $D(1)/50000$. This indicates that we have hit the noise margin. The frequency response of the S_{21} rational function model of different orders is shown in Figure 5.7.

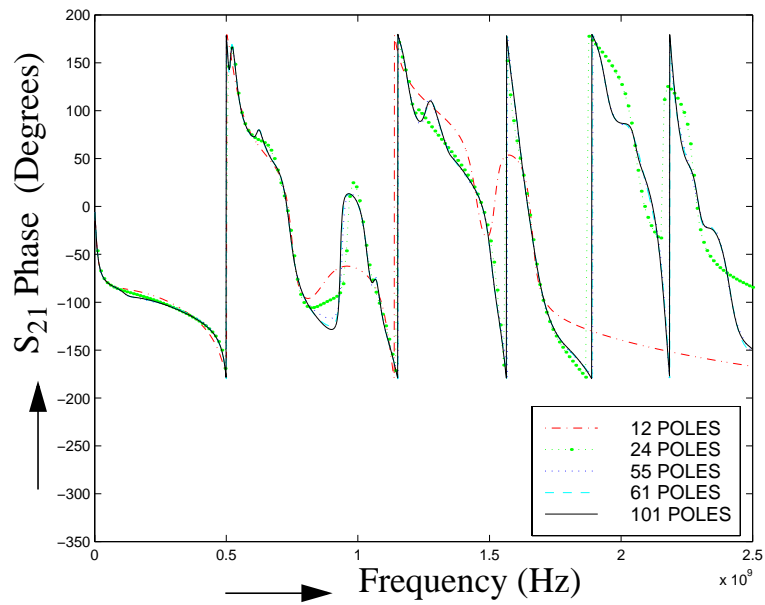
Another criterion used was the rms error between the measured transient waveform and the waveform reconstructed using GPOF. An rms error of 0.01% and a maximum error of 0.1% has been considered sufficient. There is further elimination of poles during the extraction of residues depending on the magnitude as discussed in the next section. All the values chosen are dependent on the DUT and need to be iterated to find the optimum solution. There is no necessity to have the S_{21} measurement to generate this model. The rms error in S_{21} was calculated just for demonstration purposes.

Table 5.2: Extraction Procedure Parameters

Cut-off value used for extracting the poles	RMS error for GPOF	No. of poles extracted from GPOF	Cut-off value for the residues	RMS error in S_{21}	No. of Poles used for the model
$D(1)/100$	0.4%	3	-	-	-
$D(1)/500$	0.15%	14	0.0001	10.53%	12
$D(1)/1000$	0.07%	24	0.0001	6.08%	23
$D(1)/5000$	0.02%	57	0.0001	1.78%	55
$D(1)/10000$	0.01%	77	0.0001	1.67%	61
$D(1)/50000$	0.006%	372	0.0001	1.67%	101



(a)



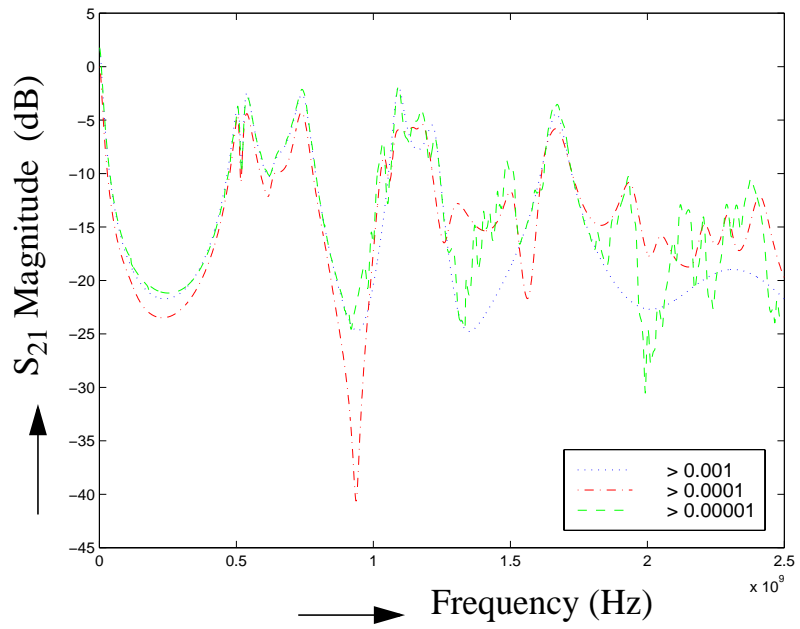
(b)

Figure 5.7 S_{21} Response due to Different Orders of the Rational Function Model
(a) Magnitude (b) Phase

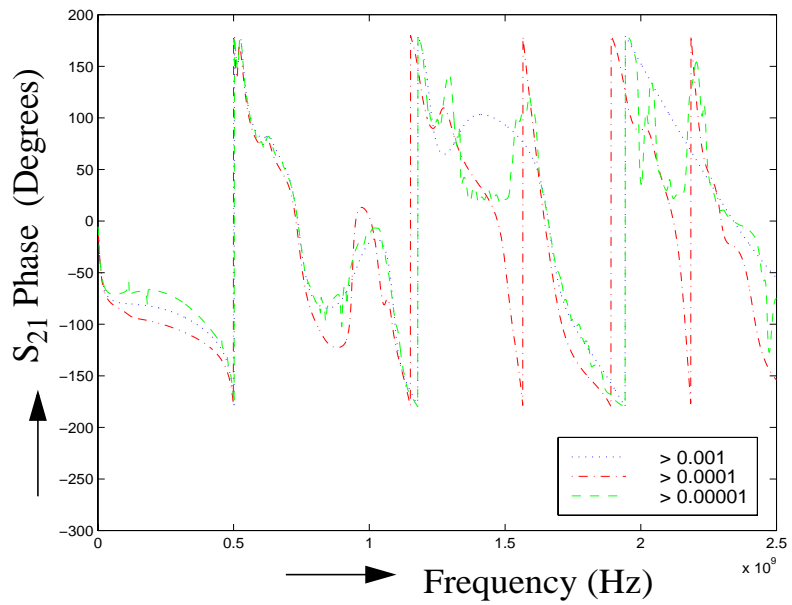
5.7 Extraction of Residues

The values of residues are calculated using recursive deconvolution. Again, this is slightly different from the simulated data. Because the poles due to signal and noise effects are not demarcated, a limit is placed on the absolute value of the residue when the pole-residue pairs are used for constructing the matrix in Section 4.3 (Eq. 4.12). This is justifiable because, for high SNR, the residues of the dominant poles need to be large compared to the non-dominant poles. In our case, only a few iterations are used and the cut-off value is determined by the amount of noise introduced. An estimate is usually made with reference to the maximum value of the residue in the given set of pole-residue pairs.

The cut-off value for the residues is varied from 0.001 to 0.00001 and the resulting S_{21} magnitude and phase are plotted in Figure 5.8. Too large a value for the cut-off does not track the response properly, while too small a value introduces noise. A cut-off value of 0.0001 was found to be optimum and this is not difficult to estimate, because of the noise introduced. The cut-off value set for the magnitude of the residues does not eliminate any poles extracted as long as we do not hit the noise margin as shown in Table 5.2. For the five cases of cut-off value considered in Table 5.2, elimination of pole-residue pairs based on the residue value, is most prominent in the fifth case where we have hit the noise margin.



(a)



(b)

Figure 5.8 S_{21} Response for Different Cut-off Values for the Residues
(a) Magnitude (b) Phase

5.8 Extracted Rational Functions

The main objective of this thesis is to develop wide band models which are accurate. As discussed in Section 5.6 and Section 5.7, the cut-off number for the singular value and magnitude of the residues is based on the corresponding maximum values in the given set of data. A very coarse range has been used here and the solution need not be the optimum. The number of poles could be further eliminated, if a narrow search is done near the chosen cut-off values. That is to say, a value of $D(1)/9000$ and $D(1)/11000$ could yield an improved confidence value. This is a compromise between computation time and acceptable error.

To obtain a optimum value for the number of poles (Table 5.2), a further elimination was done based on the magnitude of the frequencies corresponding to the imaginary part of the poles (Table 6.3, Chapter VI). The poles with higher frequencies located far away from the imaginary axis were eliminated. Each step leads to the elimination of one pair of complex conjugate poles. The rms error was calculated each time and the process was stopped when the error increased beyond 1.67 %. This led to an optimum value of 39 poles from the set of 61 poles. The poles and residues are listed in Table 5.3. A similar procedure was used to extract the rational function model for S_{11} consisting of 129 poles. More poles were required to capture the S_{11} response compared to the S_{21} response over a 2.5 GHz bandwidth. This could be due to more resonances observed.

Table 5.3: Poles and Residues of the Extracted S_{21} Model from TDT Measurement

	Real(pole)	Imag(pole)	Real(residue)	Imag(residue)
1	-2.3685302e-01	1.5163617e+01	-6.9441383e-04	-6.3872100e-02
2	-2.3685302e-01	1.5163617e+01	-6.9441383e-04	6.3872100e-02
3	-1.1921297e-01	1.4434162e+01	1.0663343e-02	-5.5417379e-03
4	-1.1921297e-01	1.4434162e+01	1.0663343e-02	5.5417379e-03
5	-1.4685380e-01	1.3741209e+01	-4.3524808e-02	-4.6243654e-04
6	-1.4685380e-01	1.3741209e+01	-4.3524808e-02	4.6243654e-04
7	-3.4877542e-01	1.3000738e+01	1.6622763e-02	5.3070643e-02
8	-3.4877542e-01	1.3000738e+01	1.6622763e-02	-5.3070643e-02
9	-2.1548392e-01	1.2197141e+01	-2.1095376e-02	5.1227314e-02
10	-2.1548392e-01	1.2197141e+01	-2.1095376e-02	-5.1227314e-02
11	-2.8443810e-01	1.0518422e+01	6.5703052e-02	-1.5864913e-01
12	-2.8443810e-01	1.0518422e+01	6.5703052e-02	1.5864913e-01
13	-2.1017207e-01	1.0148588e+01	-3.2163171e-02	8.5227537e-02
14	-2.1017207e-01	1.0148588e+01	-3.2163171e-02	-8.5227537e-02
15	-1.7049859e-01	9.4693141e+00	1.5400550e-02	-4.4870530e-02
16	-1.7049859e-01	9.4693141e+00	1.5400550e-02	4.4870530e-02
17	-2.4143839e-01	8.1429411e+00	-3.4568628e-02	3.0954746e-02
18	-2.4143839e-01	8.1429411e+00	-3.4568628e-02	-3.0954746e-02
19	-2.0389589e-01	7.4477825e+00	-7.0077053e-02	8.5458656e-02
20	-2.0389589e-01	7.4477825e+00	-7.0077053e-02	-8.5458656e-02
21	-1.4432924e-01	7.2466771e+00	-4.8142971e-03	2.1021143e-02
22	-1.4432924e-01	7.2466771e+00	-4.8142971e-03	-2.1021143e-02
23	-1.3513863e-01	6.7484483e+00	5.0306277e-02	-2.2212728e-02
24	-1.3513863e-01	6.7484483e+00	5.0306277e-02	2.2212728e-02
25	-1.2978883e-01	6.5247998e+00	2.3285896e-02	-4.7185145e-02
26	-1.2978883e-01	6.5247998e+00	2.3285896e-02	4.7185145e-02
27	-4.1439852e-01	4.7028551e+00	-2.1348638e-02	-5.5452500e-02
28	-4.1439852e-01	4.7028551e+00	-2.1348638e-02	5.5452500e-02
29	-1.6332197e-01	4.6390154e+00	9.4563431e-02	-2.4261690e-02
30	-1.6332197e-01	4.6390154e+00	9.4563431e-02	2.4261690e-02
31	-1.0474573e-01	3.9445114e+00	-1.0193496e-02	3.9808460e-03
32	-1.0474573e-01	3.9445114e+00	-1.0193496e-02	-3.9808460e-03

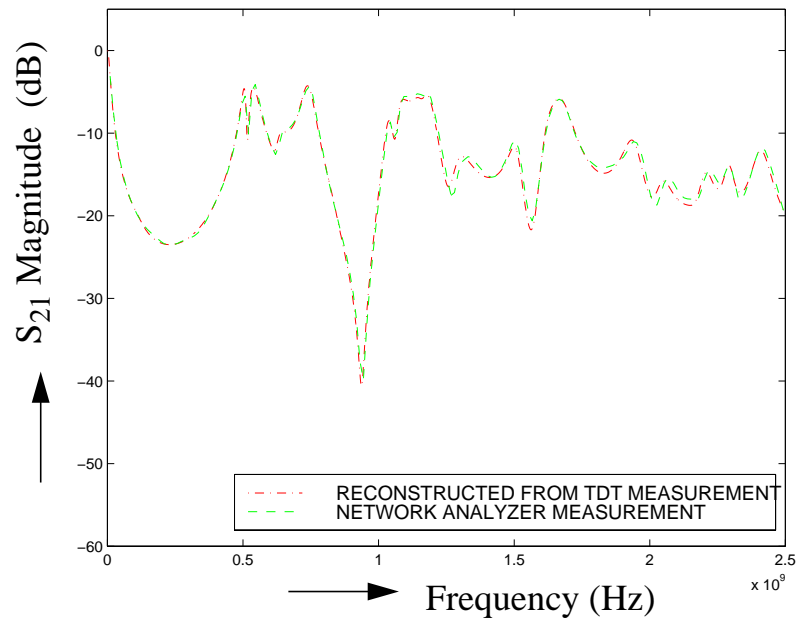
Table 5.3: Poles and Residues of the Extracted S_{21} Model from TDT Measurement

	Real(pole)	Imag(pole)	Real(residue)	Imag(residue)
33	$-6.0066336e-02$	$0.0000000e+00$	$6.0411731e-02$	$9.2455019e-18$
34	$-2.1213354e-01$	$6.9503903e-01$	$-8.1281092e-04$	$-1.4704126e-03$
35	$-2.1213354e-01$	$-6.9503903e-01$	$-8.1281092e-04$	$1.4704126e-03$
36	$-1.4230475e-01$	$3.3366419e+00$	$-1.0693686e-01$	$2.4411528e-02$
37	$-1.4230475e-01$	$3.3366419e+00$	$-1.0693686e-01$	$-2.4411528e-02$
38	$-5.4097342e-02$	$3.1995021e+00$	$1.5932892e-03$	$3.0721921e-02$
39	$-5.4097342e-02$	$3.1995021e+00$	$1.5932892e-03$	$-3.0721921e-02$

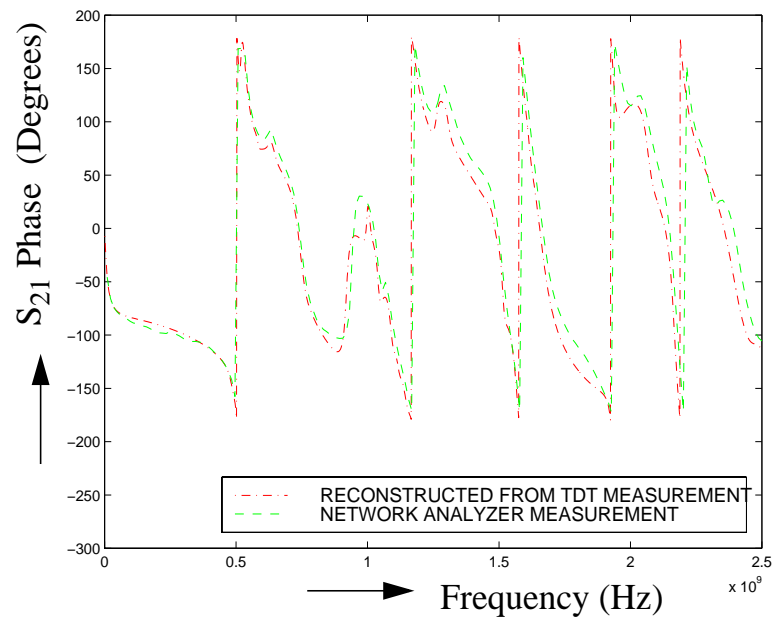
5.9 Extracted Frequency Response vs Network Analyzer Measurements

In this section, the developed rational function models for S_{21} , S_{12} , S_{11} and S_{22} are plotted using Eq. 4.16. Two-port frequency domain measurements have been made on the device using the HP 8714C, 300 KHz - 3000 MHz Network Analyzer. For TDT/TDR measurements short and thru standards were used for calibration. For network analyzer measurements, short, open, load and thru standards were used for calibration.

The reconstructed frequency response from the two-port scattering parameter models is compared with network analyzer measurements. The correlation between the waveforms is good. S_{21} is shown in Figure 5.9 and S_{11} is shown in Figure 5.10. As discussed before, the device is not exactly symmetric. So S_{12} and S_{22} functions are similarly extracted and the frequency response plotted in Figure 5.11 and Figure 5.12. The rms error between the extracted waveforms and the network analyzer measurements is 1.67% for S_{21} , 2.87% for S_{11} , 1.40% for S_{12} and 2.28% for S_{22}

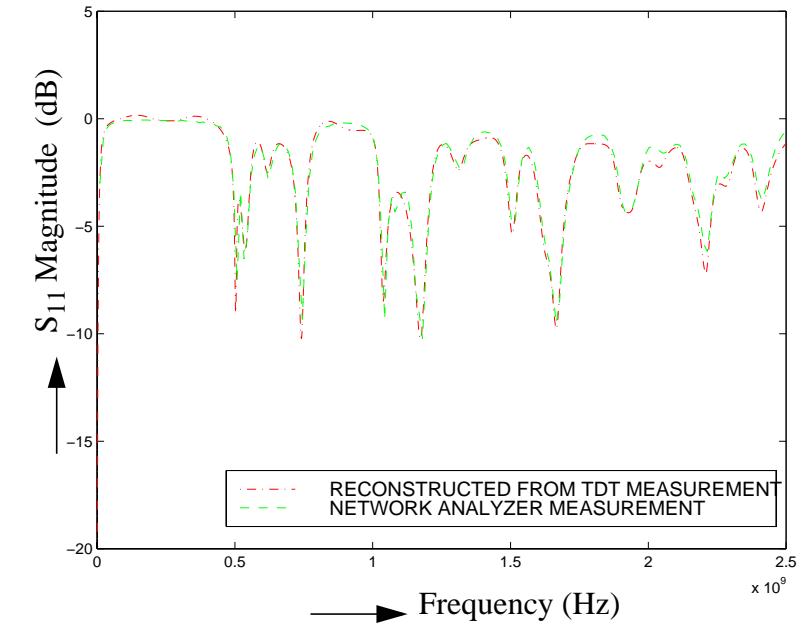


(a)

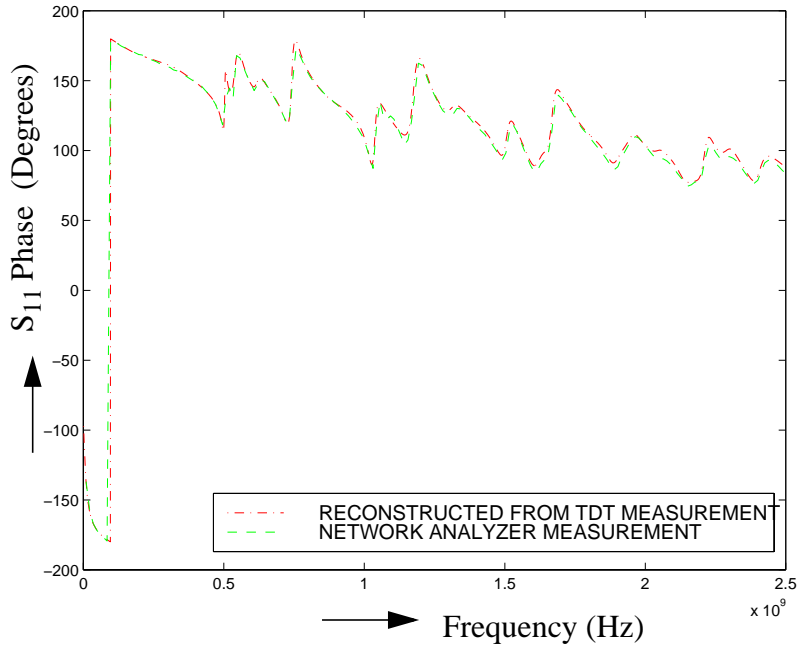


(b)

Figure 5.9 Comparison of Reconstructed S_{21} Rational Function Model Response with Network Analyzer Measurement (a) Magnitude (b) Phase

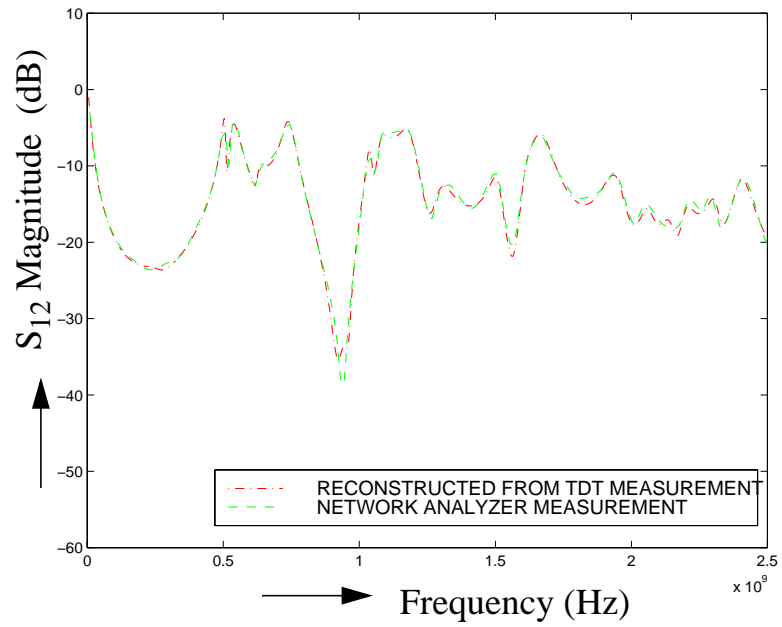


(a)

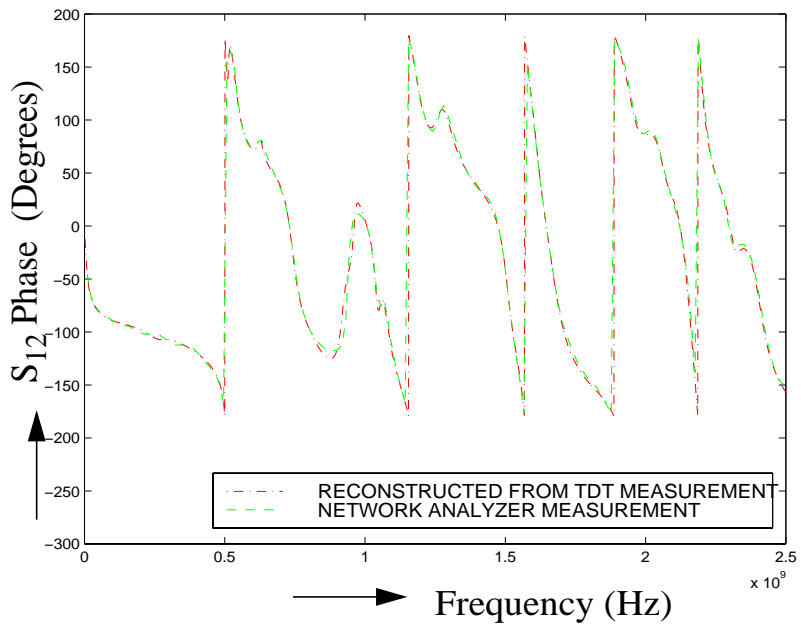


(b)

Figure 5.10 Comparison of Reconstructed S_{11} Rational Function Model Response with Network Analyzer Measurement (a) Magnitude (b) Phase

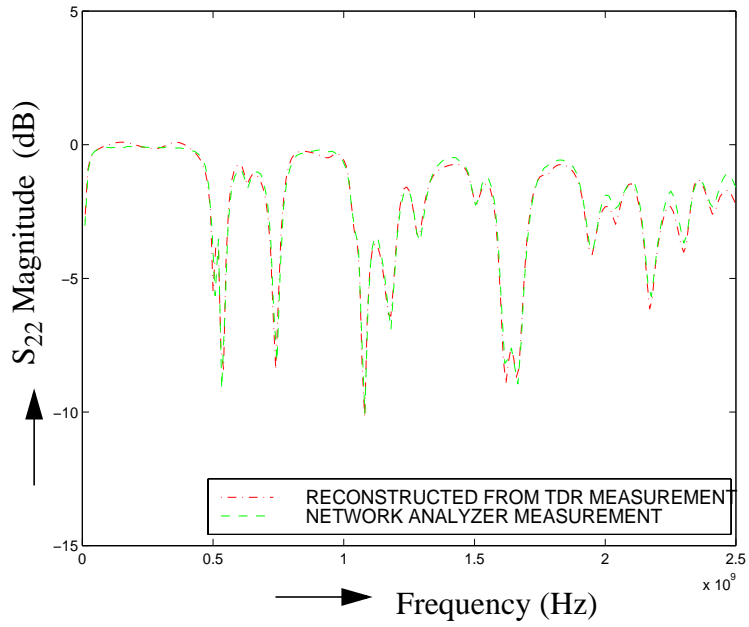


(a)

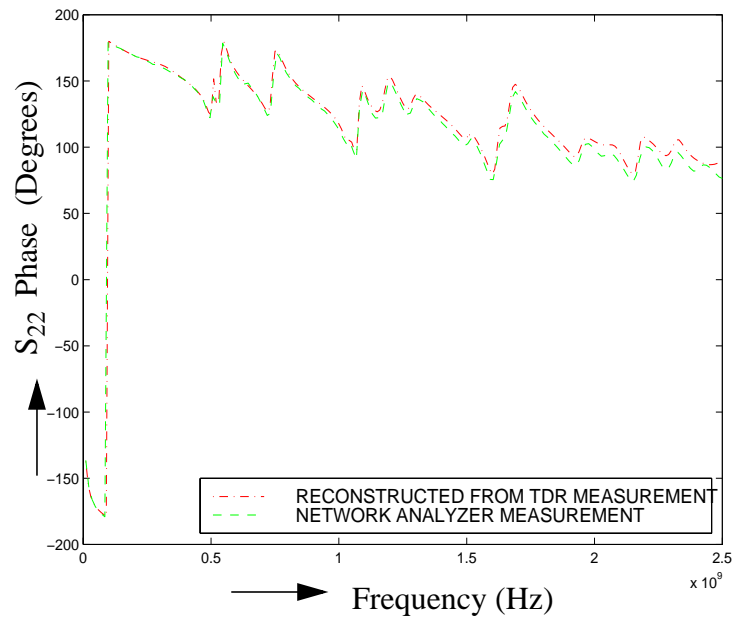


(b)

Figure 5.11 Comparison of Reconstructed S_{12} Rational Function Model Response with Network Analyzer Measurement (a) Magnitude (b) Phase



(a)



(b)

Figure 5.12 Comparison of Reconstructed S_{22} Rational Function Model Response with Network Analyzer Measurement (a) Magnitude (b) Phase

5.10 Reconstruction in Time

The TDT/TDR waveforms are computed using the recursive convolution formulation (Eq. 4.14). The measured reference waveform used as the input waveform was convolved with the developed rational function model to get the transient waveforms. As can be seen in Figure 5.13 and Figure 5.14, the agreement between the measured and simulated response is very good. The results show that the extracted rational function models are accurate both in time domain and frequency domain.

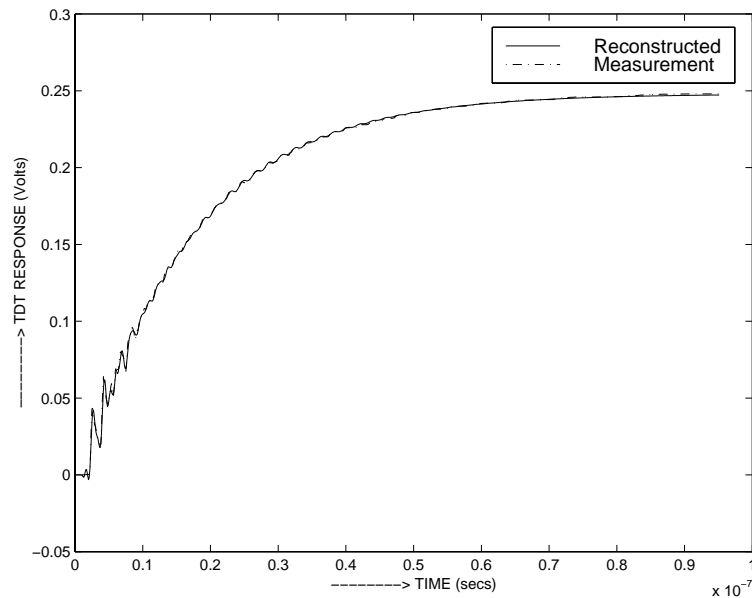


Figure 5.13 Reconstructed TDT Response and the Actual Response

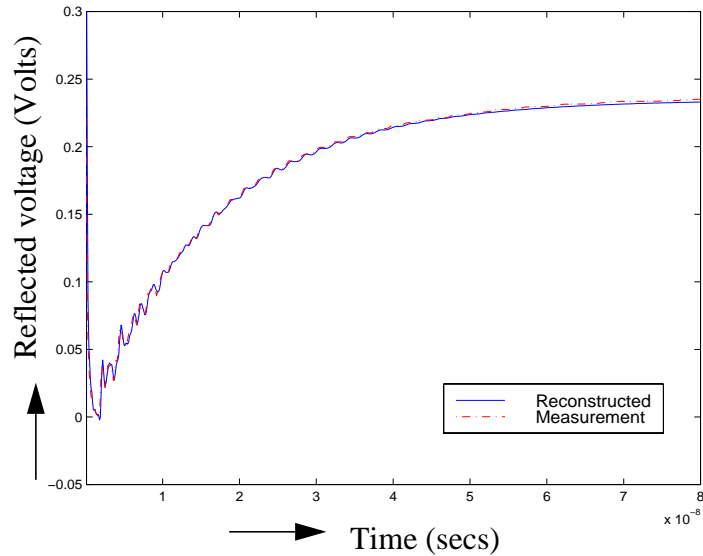


Figure 5.14 Reconstructed TDR Response and the Actual Response

5.11 Calculation of Error

It is not always possible to simulate the response of the device accurately. The DUT considered in this work has a set of transmission lines on the top plane connected to SMA connectors. Because of the difficulty in modeling the structure mounted with the connectors, an analytical model was developed for a set of parallel planes. Then a simple Π network for the SMA connector was used in SPICE to generate the overall circuit response up to 1 GHz [63]. A rational function model from TDT measurements was developed for the same bandwidth. The model had 20 pole-residue pairs and the S_{21} response was reconstructed in frequency. Two-port frequency domain measurements were made using a network analyzer. The three responses including (i) Reconstructed

from TDT measurement, (ii) Network analyzer measurement, and (iii) Simulated using SPICE, have been plotted in Figure 5.15 and Figure 5.16. As can be seen, the simulated response does not capture the two glitches both in magnitude and phase plots. Comparison of the reconstructed measurement with the network analyzer measurement using the same cables and calibration standards is the other available option and has been followed in this work.

It has been observed that the pole-residue pairs for the model developed from the measurements are different from the models developed for simulated data. Hence no attempt has been made to study the error in the pole or residue values. Since our final aim is to characterize the DUT in terms of scattering parameter models, the RMS error is calculated with reference to the network analyzer measurements of S_{11} and S_{21} using Eq. 5.1.

The glitch in the frequency response at ~500 MHz spreads out for ~30 MHz. The number of points was chosen to be 200, over a frequency range of 100 MHz-2.5 GHz, so that the glitch is captured by at least two points. Larger values of N would better capture the finer features, but then the rms value will be on the lower side. Two hundred points in the required frequency range was considered optimum for the measured waveforms. So all the network analyzer measurements involved 200 data points. The frequencies at which the response was measured using network analyzer were used to extract the corresponding scattering parameter response. This is convenient for calculating the rms error between the two, without using any interpolated data. Since the method extracts the poles from the device waveform and the residues using the input waveform, the random

error could be double in the worst case. So the final form using S_{21} response could be used as a measure of the limit of error to be expected. The rms error is calculated using

$$\text{Error}_{\text{rms}} = \sqrt{\frac{\sum [S_{ab}(\text{measured}) - S_{ab}(\text{extracted})]^2}{N}} \quad (5.1)$$

where $S_{ab}(\text{measured})$ is the value obtained from network analyzer measurements, $S_{ab}(\text{extracted})$ is the corresponding value extracted from time domain measurements, and N is the number of data points taken.

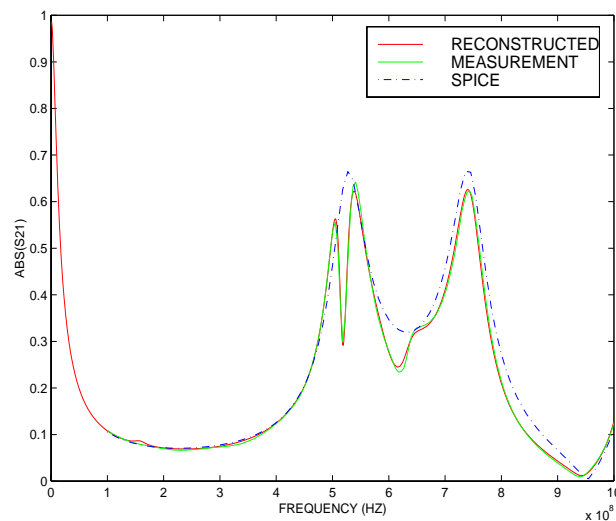


Figure 5.15 Comparison of S_{21} Magnitude from Simulation and Measurements

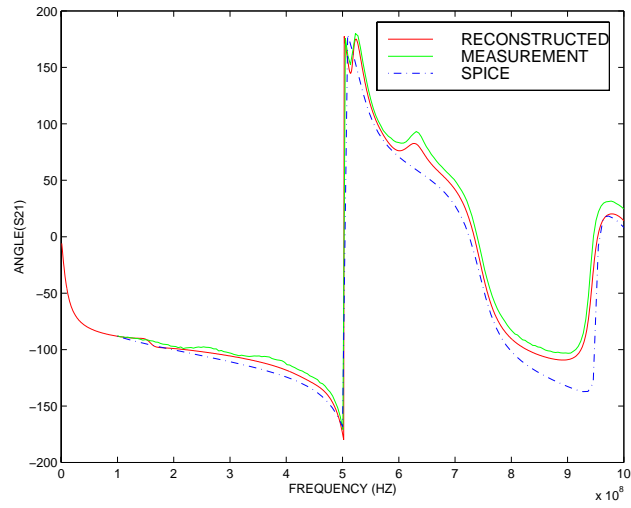


Figure 5.16 Comparison of S_{21} Phase from Simulation and Measurements

CHAPTER VI

MEASUREMENT PARAMETERS

The choice of the model used for parameter estimation is usually based on the physical constraints of the data generation process. In this work, sinusoidal parameter estimation is carried out using Generalized Pencil-of-Function (GPOF) method and recursive deconvolution. For this method, the parameters to be determined are the number of data points and the sampling interval. This sets the window length. The constraints on the number of data points and window length are placed for a large SNR associated with the data. For measured data with an unknown SNR, the optimum conditions depend heavily on the device response and are studied in this section.

Study of the effect of sample density and window length have been reported for TDNA [3]. FFT is used for frequency estimation in TDNA, hence the sample density was explained based on the Nyquist criterion. For a 20 GHz bandwidth, 100 ns^{-1} was considered optimum compared to 200 ns^{-1} and 50 ns^{-1} . For a 20 mm long coplanar waveguide, their optimum window length was 10.24 ns compared to 5.12 ns and 20.48 ns. This window length was based completely on the device response. Windows shorter than the device response time introduce error and window much longer than the response time may add noise [3],[64].

6.1 Number of Data Points Required

Exponential approximations such as in Eq. 4.1 can be solved directly using Prony's method if $N = 2n$ or solved approximately by the method of least squares if $N > 2n$. When it is known that $y(n)$ tends to a finite limit as $\delta t * n \rightarrow \text{infinity}$, the poles are expected to have negative real parts. This is the case for all passive components being studied in this thesis. This modification adds a constant to the approximation and at least $N = 2n + 1$ independent data points are needed for the determination of the poles and residues using modified Prony's method [60].

SVD Prony [55] and GPOF [56] methods have the same constraints on the number of points as Prony's. Ideally, if the data is noiseless, an M th degree polynomial can be used to find the values of a_k and s_k . But if the data is noisy, s_k cannot be estimated accurately using an M th degree polynomial. A value of L greater than M is necessary (Eq. 4.4). This redundancy in the degrees of freedom tends to increase the accuracy in the parameter estimates [55]. For a given value of N , there are upper and lower limits on the value of L , the degree of the polynomial used for approximation. If L satisfies the inequality $M \leq L \leq (N-M)$ (or $N- M/2$ in the case of forward-backward equations), then M of its L values are at e^{s_k} , $k=1,2,\dots,M$ [55]. The same concept has been used in GPOF. The optimum choice of L is around $N/2$ and is generally a function of signal parameters [57].

Looking at the data, there is no way of knowing the number of points required for the parameter extraction. Considering a maximum number for the order of the model, an estimate of the number of data points can be made. For example, if number of poles is

100 (i.e. $M \sim 100$), the minimum number of data points to be considered is at least 200 (i.e. $N = 2 * M$) points.

6.2 Sampling Interval

Both [55] and [56] are based on simulated data for two sinusoids and have worked with a sampling interval of one second not to lose the generality of their methods. Most of the work related to pole and zero estimation has been applied to antenna measurements mainly the direction finding problem, where the targets are huge and seconds is a reasonable time for data collection. Some discussion on the number of data points and sampling for short data records can be found for autoregressive spectral estimation in [65]. They examined several cases and found that sampling at twice the Nyquist rate was sufficient to obtain the minimum mean square error for their autospectral estimate. This estimate is again specific to their test case and their method. The optimum sampling interval would depend on the random process power spectral density, which is unknown.

For the packaging structures, the data length is typically a few nanoseconds and the sampling interval much less. Hence an estimate of the sampling interval has been done on the test case considered here. Because of the uniform sampling in time, the sampling interval is somewhat restrained by the type of waveform. The rise time of the step input of the measurement setup is ~ 60 ps (0% to 100%). If there are not enough points to track the rise time, the correct information about the input source as well as the device response is not captured. Considering that the minimum sampling interval is 10 ps

for this equipment, we can have a maximum of 7 points to track the rise time. The next possible sampling interval could be 20 ps with 4 points to track the rising edge of the step source.

To study the effect of sampling interval, time steps of 200 ps, 100 ps, 50 ps, 20 ps and 10 ps have been considered. The optimum window length of 30 ns has been used. This window length has been kept constant for the different values of sampling interval. This changes the number of data points used and affects the accuracy. The minimum number of points used was 150 for a 200 ps interval. This satisfies the criteria of $2N$ points which is 61×2 . The rest of the cases satisfy the minimum number of points required.

For the extraction of poles using GPOF, the number of poles has been used to set the singular value cut-off. The optimum number of poles required for the S_{21} model is 61 as discussed in Section 5.6. The extracted S_{21} response is compared to the measured S_{21} response (Figure 6.1). The rms errors calculated using Eq. 5.1 are listed in Table 6.1. The measurements with sampling interval of 200 ps produced 47.91% rms error. This is expected since the input waveform does not track the rise time. For a 100 ps time step waveform, the rise time is ~ 100 ps because first two points would have this time difference. As more points are taken to represent the rising edge of the waveform, the error is decreasing as should be. The error is minimum for 10 ps time resolution. Hence, a 10 ps time step is considered optimum for the measurements.

A similar analysis was done for the S_{11} measurements and the extraction procedure. This was necessary because more poles were used to develop the rational function model

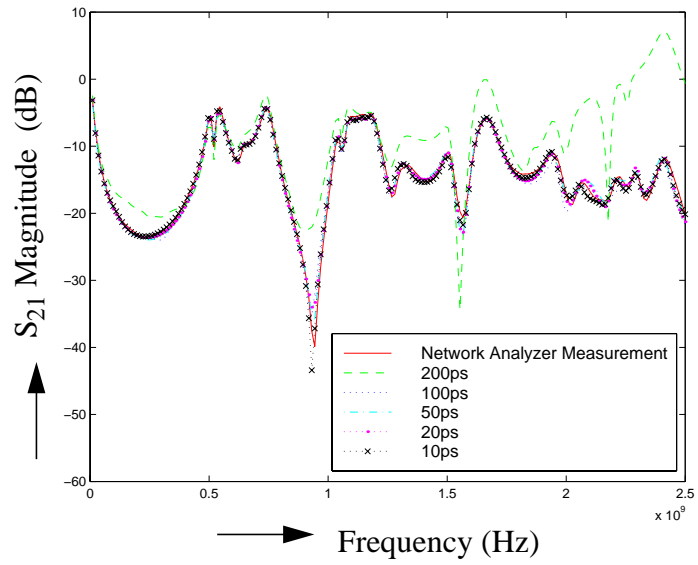
for S_{11} . The extracted S_{11} response is compared to the measured S_{11} response (Figure 6.2). The rms errors calculated using Eq. 5.1 are listed in Table 6.2. The error is comparatively more for S_{11} even with 10 ps sampling interval. Same trend was observed for the simulated case also (Section 4.4). This could be due to the insufficient data to capture the falling edge of the reflected waveform. Better results can be expected for a smaller sampling interval, as was demonstrated for the simulated case.

Table 6.1: Error Due to Resolution Calculated for S_{21}

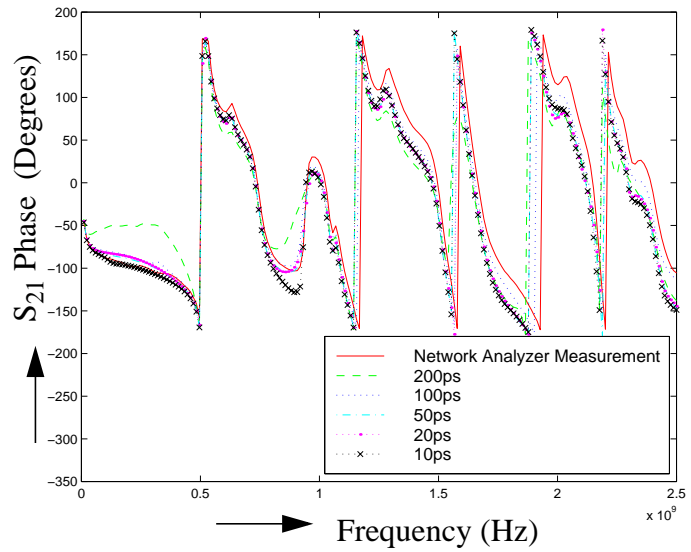
Resolution	RMS error
<i>200 ps</i>	<i>47.91%</i>
<i>100 ps</i>	<i>2.35%</i>
<i>50 ps</i>	<i>1.73%</i>
<i>20 ps</i>	<i>1.69%</i>
<i>10 ps</i>	<i>1.67%</i>

Table 6.2: Error Due to Resolution Calculated for S_{11}

Resolution	RMS error
<i>200 ps</i>	<i>20.38%</i>
<i>100 ps</i>	<i>18.6%</i>
<i>50 ps</i>	<i>3.91%</i>
<i>20 ps</i>	<i>2.90%</i>
<i>10 ps</i>	<i>2.87%</i>

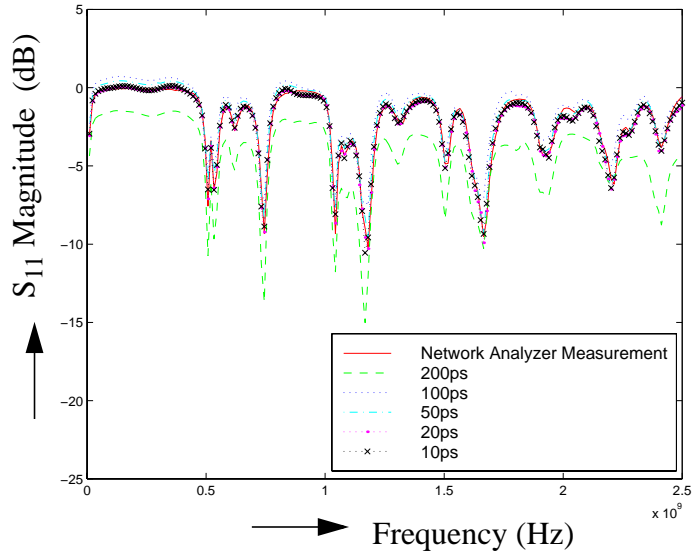


(a)

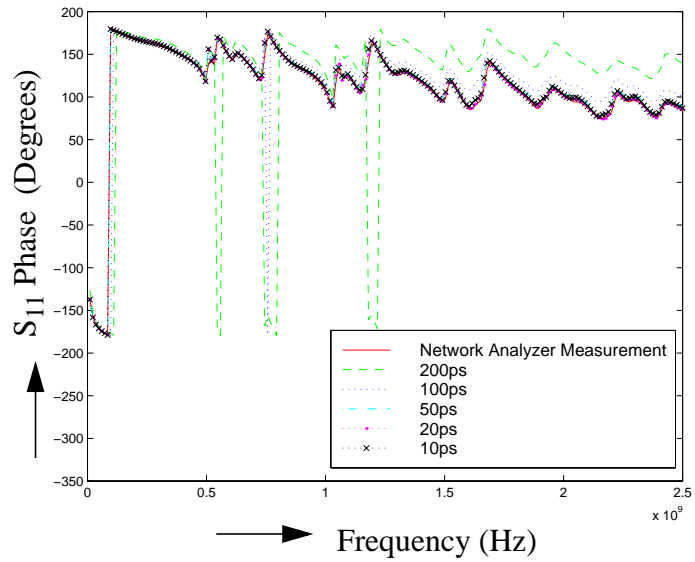


(b)

Figure 6.1 Effect of Resolution on S_{21} (a) Magnitude (b) Phase



(a)



(b)

Figure 6.2 Effect of Resolution on S_{11} (a) Magnitude (b) Phase

The second consideration was the time period of the oscillation due to the poles. The imaginary part of the poles extracted (Table 5.3, Chapter V) was used to calculate the frequency components of the S_{21} rational function model and are listed in Table 6.3. The maximum frequency of 2.41 GHz translates to a time period of 415 ps. To capture this pole, the time step should be less than ~415 ps. This condition is satisfied using the 10 ps sampling interval which was found optimum.

Table 6.3: Extracted Frequency Components

Frequency (GHz)
<i>2.4133646</i>
<i>2.2972682</i>
<i>2.1869813</i>
<i>2.0691317</i>
<i>1.9412353</i>
<i>1.6740589</i>
<i>1.6151979</i>
<i>1.5070881</i>
<i>1.2959893</i>
<i>1.1853514</i>
<i>1.1533445</i>
<i>1.0740489</i>
<i>1.0384541</i>
<i>0.74848264</i>
<i>0.73832223</i>
<i>0.62778849</i>
<i>0.0000000</i>
<i>0.11061890</i>
<i>0.53104305</i>
<i>0.50921657</i>

6.3 Time Window

The problem of interest in this work is estimating multiple sinusoids from a noisy device response using a polynomial of order M . A least squares solution is used while extracting the residues as well as determining the error criteria for pole extraction. A larger time window and consequently more data points for a fixed time step would give a better solution.

If the waveform to be processed does not contain the oscillatory behavior, there is no way of capturing the device poles [48]. Hence the waveform needs to contain the oscillations due to all the poles being extracted. The pole with the largest real value decays in the shortest time compared to the other poles and can be used to determine the effective transient time. It is well known that the pole farthest away from the imaginary axis (i.e the pole with the larger magnitude) contributes much less than the pole closest to the imaginary axis on the negative side. Based on this criteria, the pole-residue pair with the largest real value was masked and the resultant S_{21} calculated. The rms error in the reconstructed value was $\sim 3.8\%$. This pole is dominant and its decay time can be used to set the time window. The time in which this pole pair reduces to 1% of its original value is 11.124 ns. This was calculated using P_m value of 0.14432924 (pole pair 16 & 17, Table 5.3, Chapter V) using Eq. 6.1. There is a scaling factor of 1×10^9 , because the frequency is in GHz range.

$$T_{\text{decay}} = T_{\text{end}} - T_{\text{start}} = \frac{\ln(100)}{P_m} \quad (6.1)$$

where T_{end} is the time at which the effect of the pole reduces to 1% of the value at T_{start} , and P_m is the pole with the maximum real part in the set of dominant poles required for the rational function model.

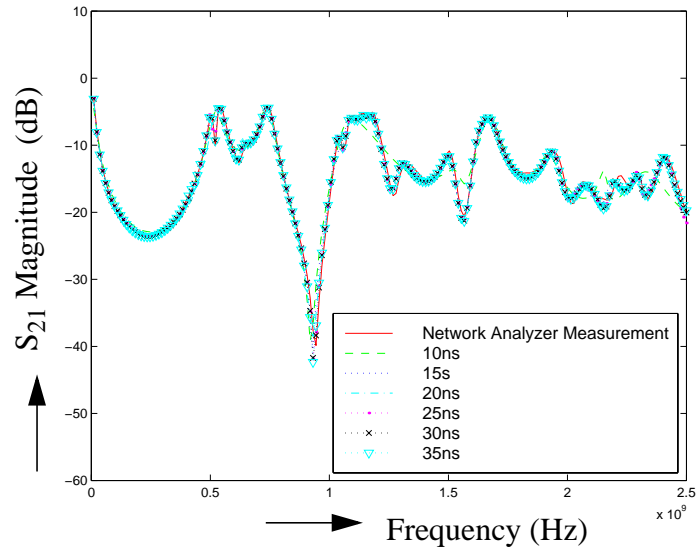
A time window of ~12 ns is the minimum required for extracting the S_{21} model. This is for an ideal situation involving no noise. But the presence of noise changes the scenario and is usually dependent on the device and measurement setup. Similar to the study of the effect of sampling time, time windows of 10 ns, 15 ns, 20 ns, 25 ns, 30 ns and 35 ns have been considered. The optimum sampling interval of 10 ps was used. For the extraction of poles using GPOF, the optimum number of poles (Section 5.6) was used to set the singular value cut-off. The extracted S_{21} response is compared to the measured S_{21} response (Figure 6.3). The rms errors calculated using Eq. 5.1 are listed in Table 6.4. The rms error reduces for increasing length of time window and is minimum for a 30 ns window. Taking 35 ns time window does not reduce the error further and this could be due to noise. Similar analysis was done for S_{11} measurements and extraction procedure and a similar trend is observed. The rms error is listed in Table 6.5 and the frequency response is shown in Figure 6.4. So for all the measurements in this thesis, a time window of 30 ns is considered to be optimum.

Table 6.4: Error Due to Window Length Calculated for S_{21}

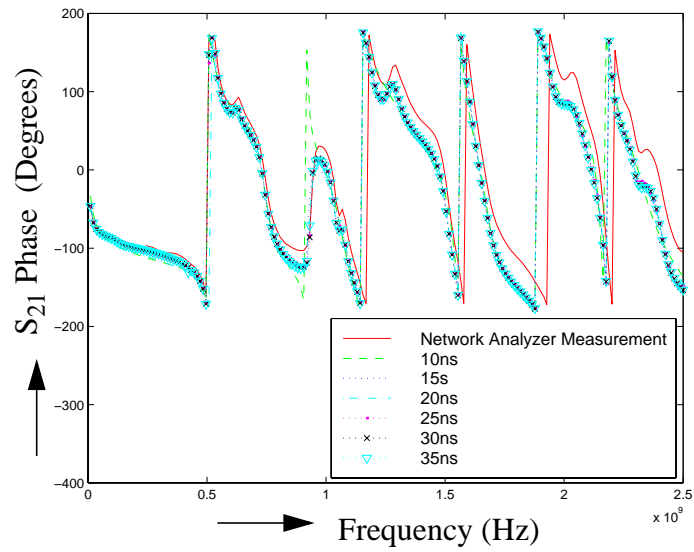
Time window	RMS error
<i>5 ns</i>	<i>26.13%</i>
<i>10 ns</i>	<i>5.01%</i>
<i>15 ns</i>	<i>3.10%</i>
<i>20 ns</i>	<i>3.09%</i>
<i>25 ns</i>	<i>2.15%</i>
<i>30 ns</i>	<i>1.80%</i>
<i>35 ns</i>	<i>1.80%</i>

Table 6.5: Error Due to Window Length Calculated for S_{11}

Time window	RMS error
<i>5 ns</i>	<i>14.4%</i>
<i>10 ns</i>	<i>6.47%</i>
<i>15 ns</i>	<i>4.78%</i>
<i>20 ns</i>	<i>3.81%</i>
<i>25 ns</i>	<i>3.68%</i>
<i>30 ns</i>	<i>2.87%</i>
<i>35 ns</i>	<i>2.92%</i>

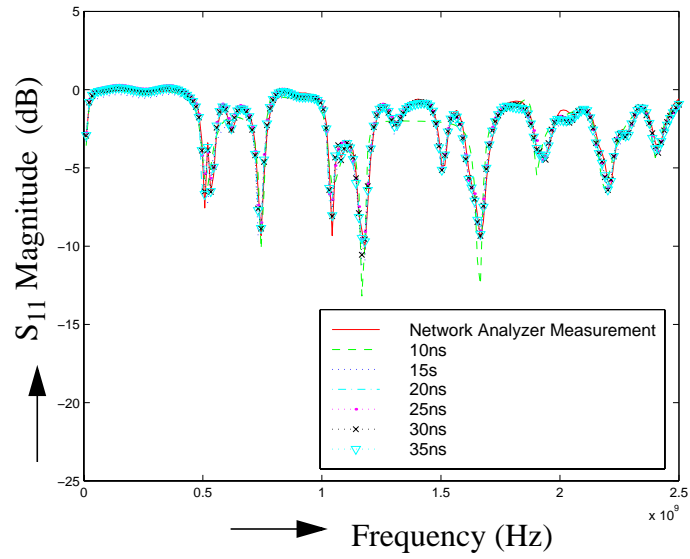


(a)

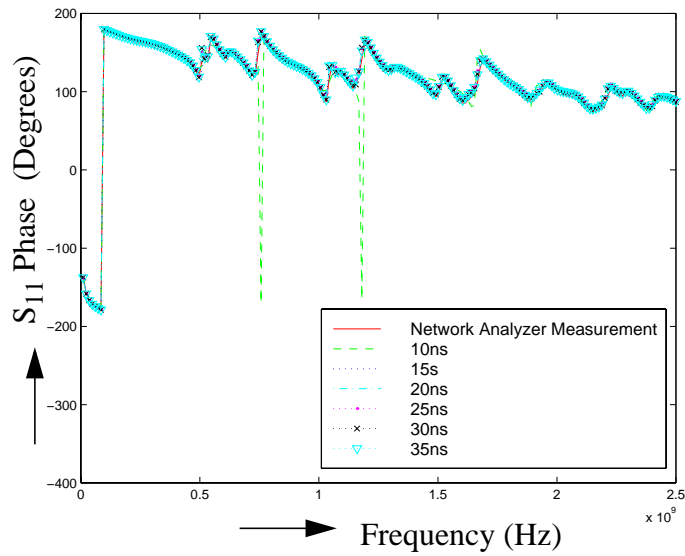


(b)

Figure 6.3 Effect of Time Window on S_{21} (a) Magnitude (b) Phase



(a)



(b)

Figure 6.4 Effect of Time Window on S_{11} (a) Magnitude (b) Phase

CHAPTER VII

ERROR SOURCES

The non-idealities associated with TDR/TDT measurements sometimes mask the features trying to be identified. The finite bandwidth and non-zero rise time of the source, the impedance deviation of the source from the nominal 50 Ω , and the measurement structure and cabling between the source and the actual device to be measured will perturb the measurement. Network analysis measurement errors can be separated into random and systematic errors and are discussed in the following sections.

7.1 Random and Drift Errors

Random errors are measurement variations due to noise in oscilloscope amplifiers and generators and due to connector repeatability, and cannot be completely removed from the measured data. Noise is vertical or voltage uncertainty and is primarily determined by sampling head design. Timing uncertainty errors are due to jitter and drift. Jitter is the short term random fluctuation in the time base caused by the imperfect trigger and time base circuits. Drift is the long term systematic fluctuation in the time base. These errors affect both the reflection and transmission measurements.

The average values for a state-of-the-art scope and sampling head are 1.2 mV vertical noise (rms) and timing jitter (rms) of 2.5 ps. Noise and jitter cannot be completely corrected, even by the use of statistical models, because the generator time shifts are not linear with time. An estimate for data variances and probabilities for the differences between measured and mean values has been provided in [66]. The overall accuracy of a TDNA system is limited by the oscilloscope's ability to repeat measurements in short time. The maximum errors due to TDNA system repeatability are small and acceptable for many applications, but in comparison to FDNA results, TDNA repeatability errors are significantly larger [64].

7.2 Error Limits

The equipment specifications (Section 7.4) place a limit on what we can achieve in the vertical as well as horizontal resolution and provide some insight into the errors involved. Random errors introduced by the non-linearity of the oscilloscopes horizontal and vertical scales cannot be easily removed. One can, however, determine the amount of error being introduced in the measurement. A comparison of the extracted frequency response from time domain measurements with frequency domain network analyzer measurements using the same cables and calibration standards is used for estimation as discussed in Section 5.11.

7.2.1 Vertical Noise

The first issue is voltage noise present in the sampling oscilloscope vertical channel. Vertical noise is nearly Gaussian, stationary, and possesses a zero mean value about the time voltage value of the measured pulse waveform. Hence, additive signal averaging is routinely used to reduce the effects of vertical channel noise [67]. If the vertical axis noise process is stationary with a zero mean value about the voltage value of the measured pulse waveform, then the additive averaging of a large number of samples at each sampling point will eventually permit convergence to the true value of the measured pulse waveform. That is,

$$\lim_{N \rightarrow \infty} \left\{ \frac{1}{N} \sum_{j=1}^N [v(t) + v_j(t)] \right\} = v(t) \quad (7.1)$$

where $v(t)$ is the true voltage at time t , $v_j(t)$ is the added vertical noise component and N is the total number of samples.

The effect of averaging has been studied in the evaluation of S_{21} using TDNA [3]. TDNA accuracy was shown to improve for increasing number of averages, though this comes at the expense of increasing measurement time. As the number of averages increases, the rate of decrease in the rms values was observed to diminish. Part of the improvement at a low number of averages may be due to increase in time stability. The smaller changes at high numbers of averages may indicate the TDNA accuracy is

approaching an intrinsic instrumentation limit [3]. Thus, the error is minimized by an optimal averaging that corresponds to a compromise between the decrease of random error effects and increase of the system nonstationarity effects.

In this section, we tried to evaluate the rms error for different averages to find the number of averages that need to be used to get an optimum solution. Again the optimum value of 30 ns for the time window and 10 ps for the sampling interval was used. The measurements were made using 2, 4, 16, 64, 256 and 1024 averages. The effect of averaging to reduce noise is shown in Figure 7.1.

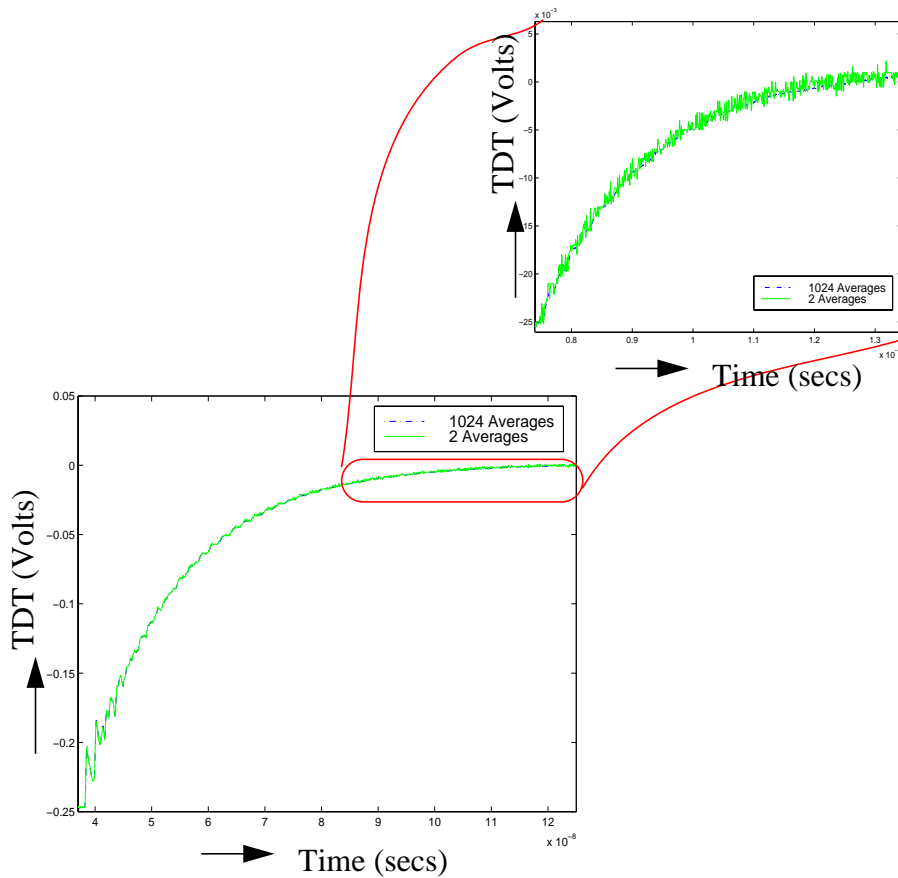
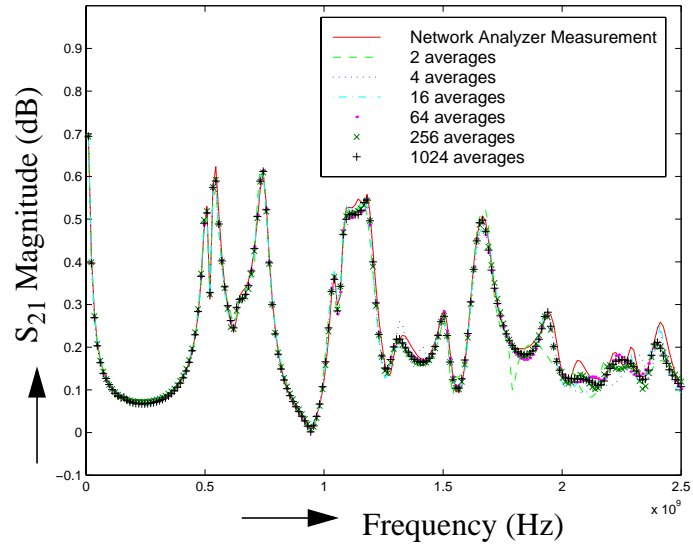


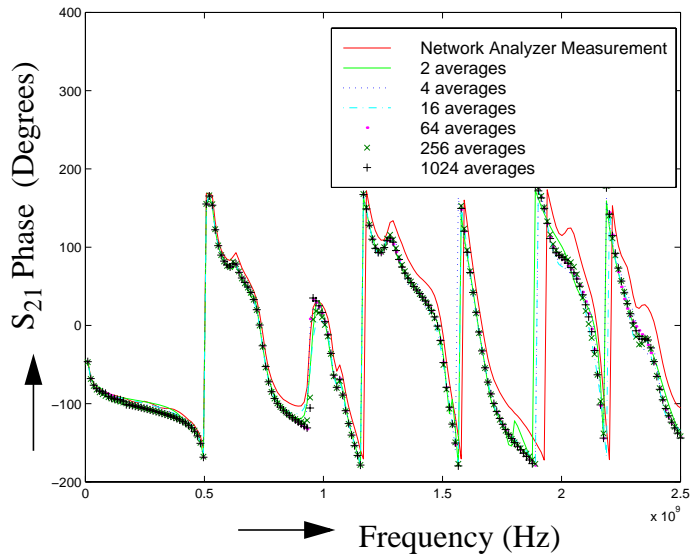
Figure 7.1 Effect of Averaging

For the processing itself, the number of poles was estimated using the waveform with two averages. This waveform has the worst noise level compared to the rest of the waveforms, as shown in Figure 7.1 with reference to 1024 waveforms. Due to noise, more poles with small residues will be extracted for two averages than 1024 averages. If a singular value was chosen as the reference singular value for all the waveforms, about ~150 poles were extracted for waveform with 2 averages and ~ 40 poles were extracted for waveform with 1024 averages. Hence, the number of poles was chosen as a base criteria to evaluate the error. As discussed in Section 5.6 and Section 5.7, 61 poles and a residue cutoff value of 0.001 have been used for the waveforms with different averages to compare the rms error values.

The rms error, as described in Section 5.11, is tabulated along with the time taken for the averaging. This time does not include the data acquisition from the DSO to the computer. As seen in Table 7.1, the rms error keeps decreasing for increasing number of averages, but the rate of decrease from 64 averages to 256 averages is about 0.06% whereas the required measurement time has increased by a factor of three. The corresponding plots are shown in Figure 7.2. Depending on the acceptable error an optimum number of averages has to be chosen. For all the measurements in this work, 64 averages have been chosen as a compromise between error level and the time taken for averaging.



(a)



(b)

Figure 7.2 Effect of Averaging (a) S_{21} Magnitude (b) S_{21} Phase

Table 7.1: Error Due to Averaging

Averages	RMS error (%)	Time taken (secs)
<i>2</i>	<i>3.13</i>	<i>~1</i>
<i>4</i>	<i>2.34</i>	<i>~2</i>
<i>16</i>	<i>1.97</i>	<i>~3</i>
<i>64</i>	<i>1.87</i>	<i>~5</i>
<i>256</i>	<i>1.81</i>	<i>~15</i>
<i>1024</i>	<i>1.77</i>	<i>~50</i>

7.2.2 Timing Jitter

The second major source of noise resides in the sampling oscilloscope horizontal (time) channel in the form of sampling time jitter. If the scanning voltage is held fixed, corresponding to a fixed point on the waveform being measured, the measured voltage will fluctuate because of imprecise triggering as the gate moves around over a small time segment about its mean position [67]. This is called timing jitter.

7.2.2.1 Short reference

Since a short waveform is used for setting the time reference to window the device response, any error in this waveform will affect the extraction of the rational function model. The timing error due to jitter in the measurements has been quantified by repeating over a period of 1 hour, 1 day, 2 days, 3 days and 1 week. The rise time

calculation itself did not vary, but there is a change in timing reference of ~ 4 ps (Figure 7.3). Hence, it is advisable to make both the reference and device measurements in a short time to avoid this error.

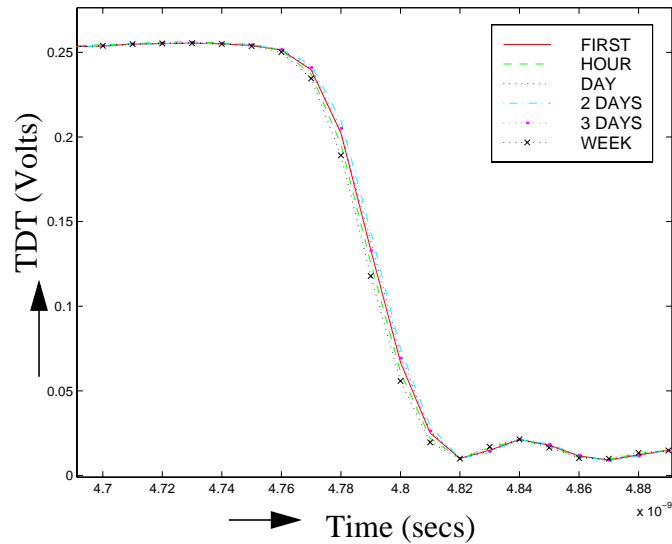
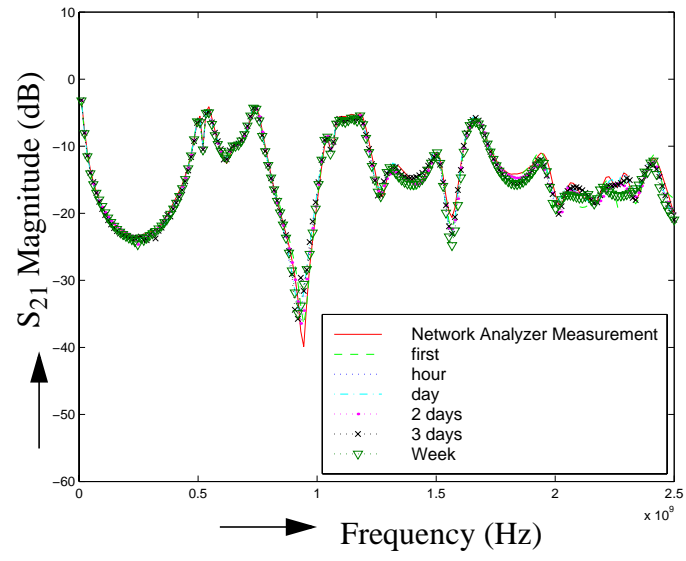


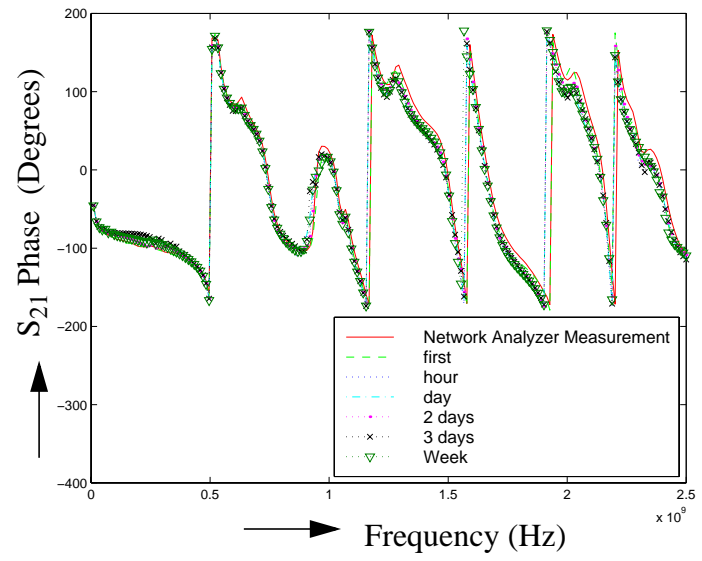
Figure 7.3 Effect of Jitter on Time Reference Waveform

7.2.2.2 Device Model

The error caused by jitter has been quantified by repeating the measurements over a period of 1 hour, 1 day, 2 days, 3 days and 1 week. The reference waveform was measured each time. For pole extraction using GPOF, the cut-off singular value and the value of the residues for extraction of the pole-residue pairs was kept constant for the extraction procedure for all the waveforms as discussed in Section 5.6 and Section 5.7. The frequency response is shown in Figure 7.4. The rms error was calculated using Eq. 5.1 and the maximum error was $\sim 3\%$ (Table 7.2).



(a)



(b)

Figure 7.4 Effect of Jitter (a) S_{21} Magnitude (b) S_{21} Phase

Table 7.2: Error Due to Jitter - Different Reference Waveforms

Measurements repeated in	RMS error
<i>First</i>	<i>1.76%</i>
<i>1 Hour</i>	<i>1.80%</i>
<i>1 Day</i>	<i>1.84%</i>
<i>2 Days</i>	<i>1.96%</i>
<i>3 Days</i>	<i>2.04%</i>
<i>1 Week</i>	<i>2.58%</i>

A second case was considered wherein the device measurement was made at different times but the reference measurement was made only at the beginning. The rms error is slightly lower for measurement made in days (Table 7.3). This could be because of the randomness in the error due to jitter. The results are relatively consistent as far as the error range is concerned. It can be concluded the error due to jitter is quite random and a worst case error is ~3%.

Table 7.3: Error Due to Jitter - Same Reference Waveform

Measurements repeated in	RMS error
<i>First</i>	<i>1.76%</i>
<i>1 Hour</i>	<i>1.89%</i>
<i>1 Day</i>	<i>1.86%</i>
<i>2 Days</i>	<i>1.68%</i>
<i>3 Days</i>	<i>1.85%</i>
<i>1 Week</i>	<i>2.27%</i>

7.3 Systematic Errors

Correctable systematic errors are the repeatable errors that the system can measure. These errors are caused by line mismatch, deflection nonlinearities and inaccurate time window widths [66]. The assumption made in this characterization method is that the systematic errors cause the same error in the reference waveform and the device waveform. These are eliminated in the deconvolution process.

7.4 Equipment Specifications and Related Limitations

For the measurement set-up, a Tektronix 11801B DSO with an SD-24 TDR/Sampling Head was used. The SD-24 is a part of the DSO and its functions are controlled automatically by the mainframe instrument [68]-[69]. These include such things as vertical scaling and horizontal sampling rate. But the bandwidth and rise time are dependent on the sampling head. Tektronix 11801B & SD-24 specifications of interest are

(1) Bandwidth and rise time are dependent on SD-24 sampling head

* Bandwidth is typically 20 GHz and is sufficient for the characterization methods and the DUTs considered in this thesis

* Rise time for the incident pulse is typically 28 ps (10% to 90%) and is 35 ps or less for the reflected pulse. We are interested in the rise time at the end of the cable, at the input port of the device. The effective rise time is calculated for each measurement setup as in Section 2.4.1 and Section 5.2.

* Aberrations in the step are +/- 3% or less until about 100 ns after the step, which is the region of our interest.

* Displayed noise with smoothing is typically $600 \mu\text{V}_{\text{rms}}$.

* Time coincidence between channels is 10 ps. If we are making measurements on multiple channels for device and reference, this will cause error.

(2) Voltage measurement accuracy

* Measurement level accuracy is +/- 2 mV. The offset adjusts the DC voltage accuracy by setting the reference level to zero and its accuracy is +/- 2 mV. The worst case error in vertical scale is ~ +/- 4 mV. Since the final computation requires two measurements (device and reference), the worst case error could be 1.6% in the voltage level.

(3) Time interval measurement accuracy

* $8 \text{ ps} + 0.01\% \times (\text{interval}) + 0.001\% \times (\text{position})$ accuracy is guaranteed. With this accuracy and the data acquisition card used for the setup, the minimum time interval being saved was 10ps. This is the limit on the sampling interval for the measurement setup.

CHAPTER VIII

RATIONAL FUNCTION MODELS FOR LOSSY THIN FILM PLANES

Rational function models have been developed from TDR/TDT measurements for low loss Printed Circuit Board (PCB) planes in Chapter V. Similar models are developed for lossy thin film planes in this section. Due to DC losses in the structure, thin film planes attenuate electromagnetic energy which translates into a reduction in the quality factor (Q) at resonance. This produces a damped ground bounce waveform that decays in a very short time period as compared to low loss structures such as PCB planes. The damped ground bounce could be an advantage for low voltage and mixed signal systems.

Power/ground plane structures have been characterized using TDR measurements based on a non uniform transmission line model in [70], but the plane structure discussed in this section provides some unique challenges. Since the impedance of the thin film planes is $\sim 0.2 \Omega$ and the TDT equipment is a 50Ω system, modifications in the measurement setup are required to couple sufficient energy onto the planes. This problem is magnified due to the large frequency bandwidth requirements of the planes requiring the generation and propagation of high speed pulses [48].

8.1 Pulse Propagation on a Low Impedance Thin Film Plane Structure

The schematic of the thin film plane structure is shown in Figure 8.1 which measures 1 cm x 1 cm with two planes separated by a 6.5 μm thick dielectric. The dielectric used was photodefinable epoxy resin (relative dielectric constant of 3.4) without the filler contents [75]. The bottom plane is solid metal and vias have been used to make contact to the bottom plane with 150 μm x 150 μm via pads on the top surface allowing access to the bottom plane. As shown in the figure, the test structure contains a two dimensional array of vias which allows the propagation of the pulses through various via positions. The fabricated thin film plane structure is shown in Figure 8.2.

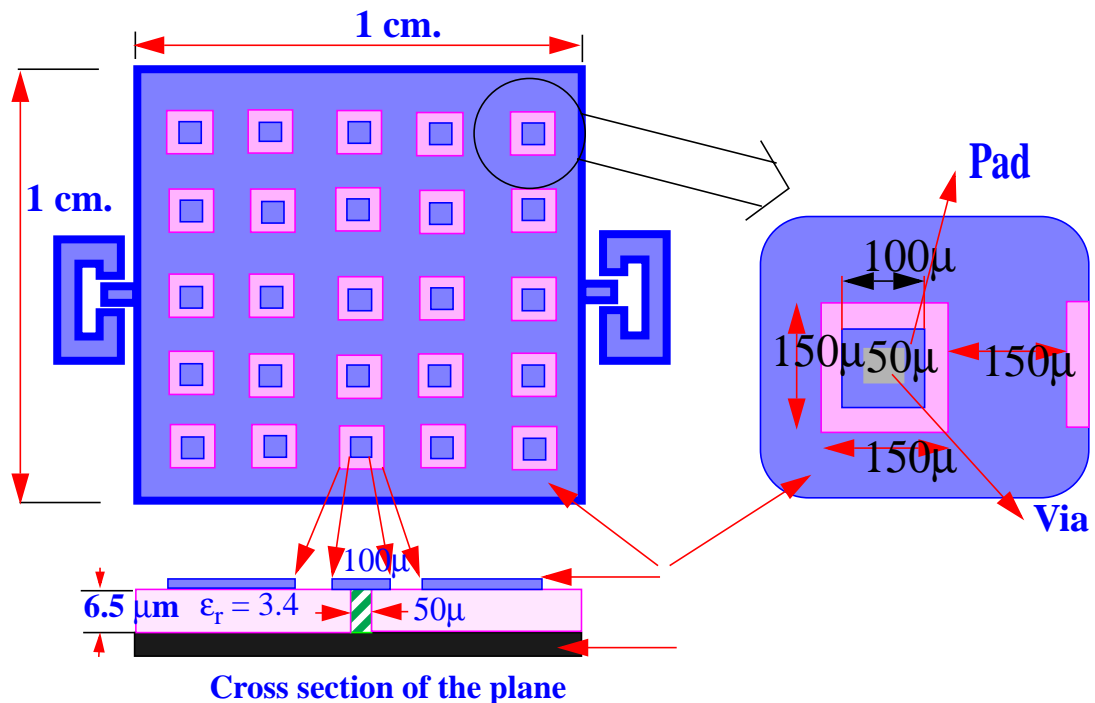


Figure 8.1 Physical Dimensions and Cross Section of the Thin Film Plane

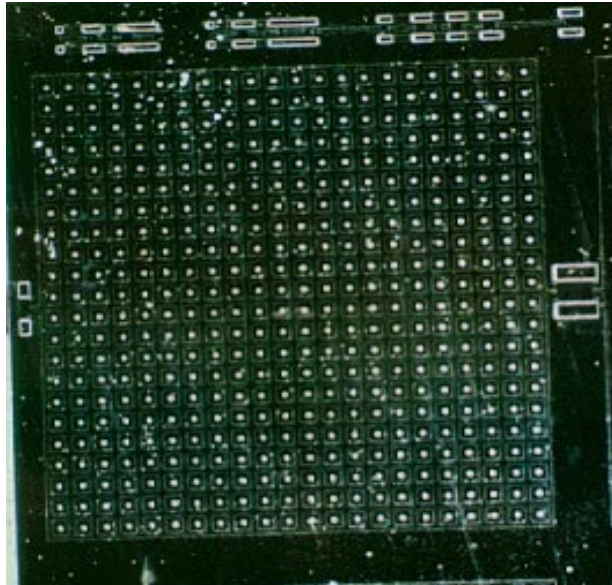


Figure 8.2 1 cm x 1 cm Fabricated Meshed Plane Structure



Figure 8.3 Measurement Using Probes

150 μm pitch Cascade Microtech probes with a frequency bandwidth of 40 GHz were used for making the TDR/TDT measurements (Figure 8.3). Using the internal source of 250 mV, and a 35 ps rise time step, the TDR and TDT measurements are as shown in Figure 8.5 and Figure 8.6. A TDR measurement on a short calibration standard was used for time windowing the plane response. The waveforms clearly show the charging of the capacitor formed by the two parallel plates. But this set-up would produce a transient pulse on the planes of the order of 3 mV which is error prone.

Since the plane structure in Figure 8.2 is a low impedance structure ($\sim 0.2 \Omega$), launching a transient pulse onto the planes using a 50Ω TDR/TDT system is a serious problem. Hence the TDR/TDT setup was modified to include a 9 V, 15 ps rise time source from Pico Second Pulse Labs (PSPL). The receiving sampling head used was the TEK SD-24. However, since the cut-off amplitude of the SD-24 is 3 V, a wideband 20 dB attenuator was used at the receiving head. The original transient behavior was then recreated in the digital sampling oscilloscope. The experimental set-up is shown in Figure 8.4. The initial period (~ 50 ps) of the transient response is shown in Figure 8.7 using a 9 V, 15 ps risetime input which represents the ground bounce on the structure.

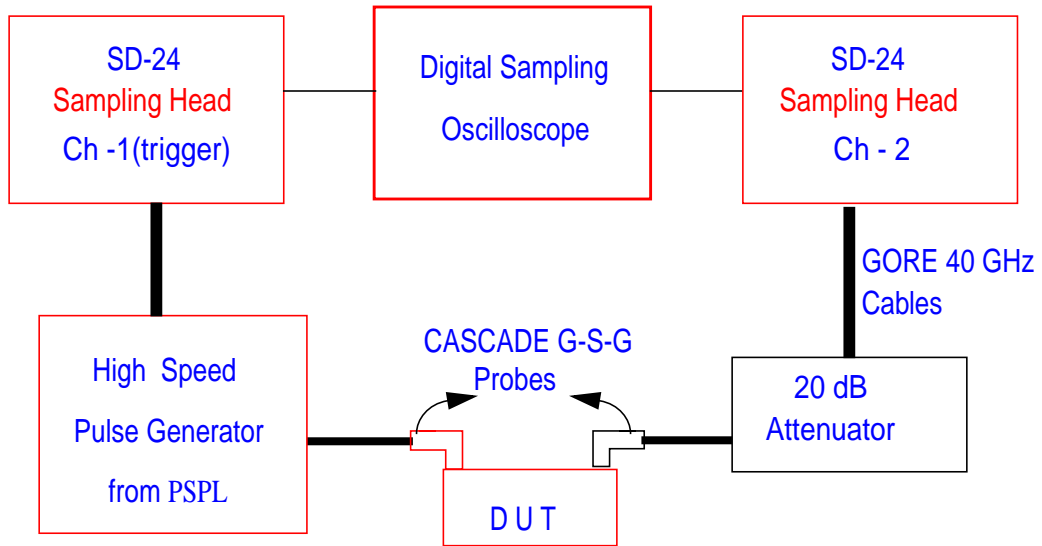


Figure 8.4 Block Diagram of TDR/TDT Measurement Set-up

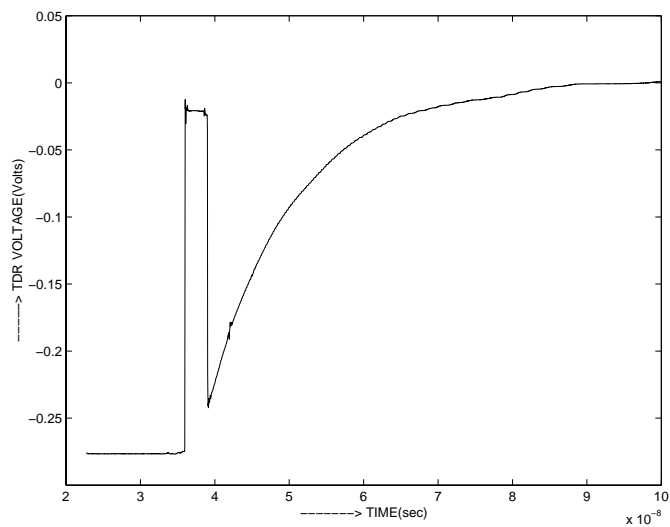


Figure 8.5 TDR Response

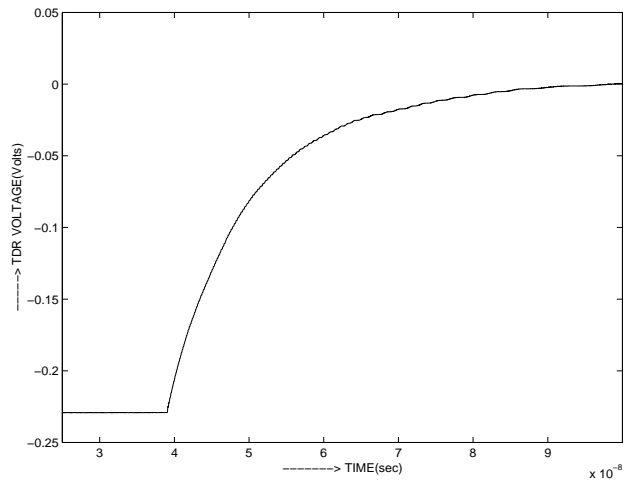


Figure 8.6 TDT Response

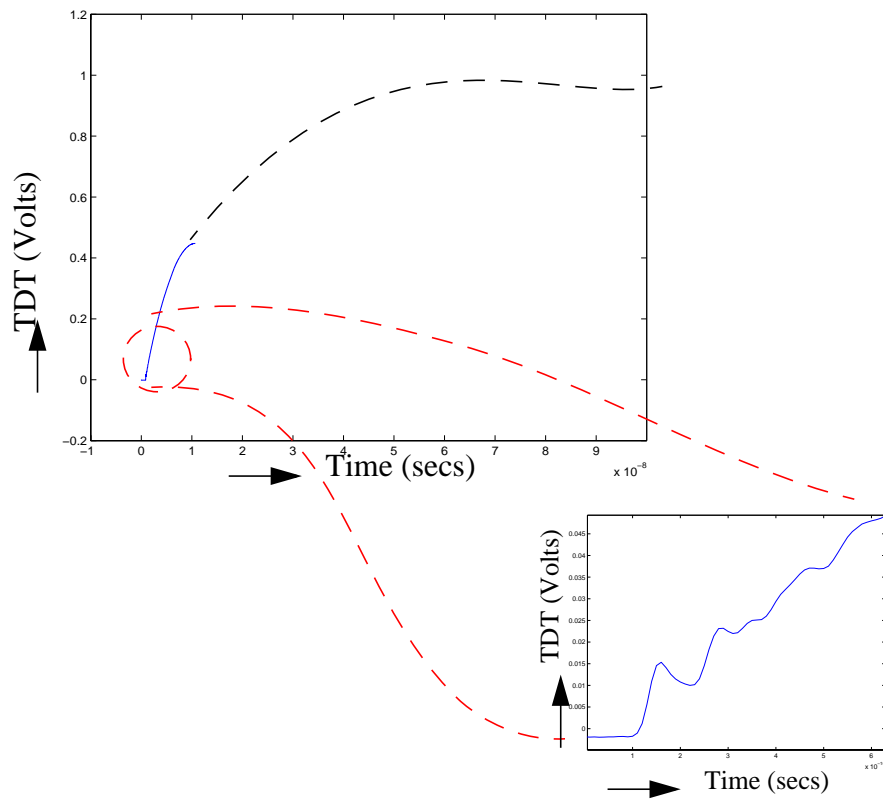


Figure 8.7 Initial Transient Waveform

8.2 Extraction of Rational Function Model

Similar to the extraction of S_{21} model for the PCB plane in Chapter V, a rational function model was extracted for the thin film plane over a 12 GHz bandwidth. The 15 ps pulse source places limitations on the pulse width. The window length cannot extend beyond 3.5 ns to avoid the rising edge of the pulse. The minimum sampling interval for the set-up is 10 ps. Taking these parameters into account, the device measurement cannot have more than 350 data points. A short measurement was used for the time reference as before. A thru waveform was used for deconvolution. The calibration standards were not available on the device. A Cascade Microtech impedance standard was used for the measurements. Some error in the measurements can be due to these standards. The device and reference waveforms are as shown in Figure 8.8. The waveforms for extraction of poles and residues included the effect of the 20 dB attenuator and hence the maximum amplitude is 0.9 V, both for the device and reference waveforms.

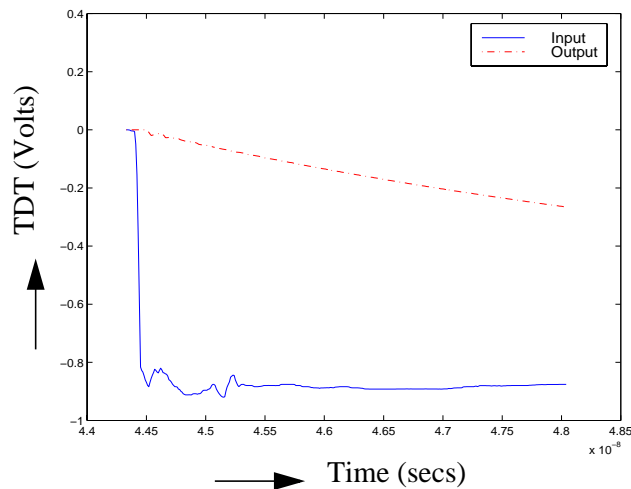
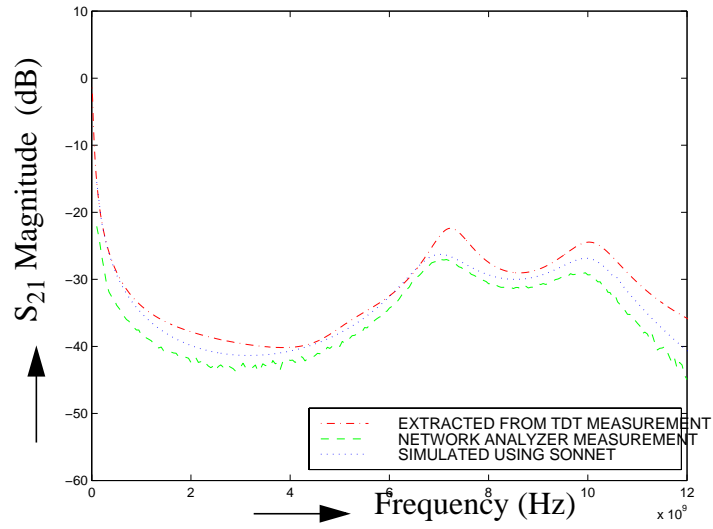


Figure 8.8 The Device and the Reference Waveform

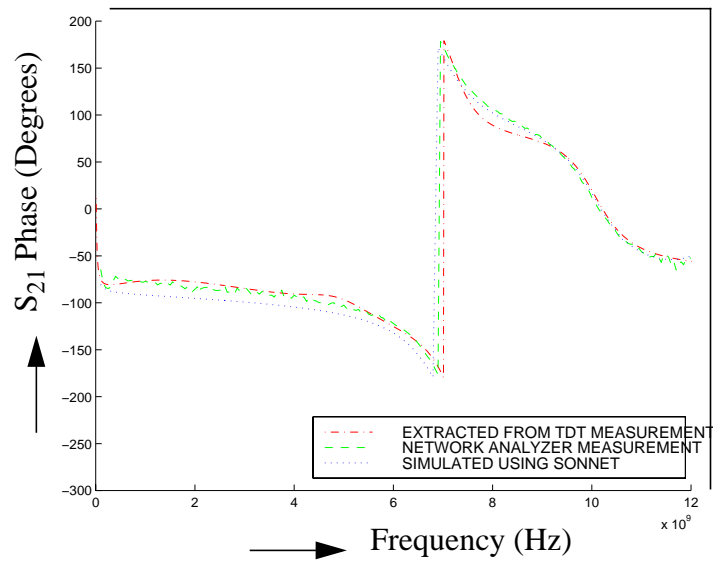
A combination of GPOF and recursive convolution was used for extracting the rational function model as before. The rational function model extracted had 9 poles over a 12 GHz bandwidth. This model is much simpler than the PCB plane in Chapter V. The poles and residues extracted are listed in Table 8.1. The response of S_{21} model is plotted in the frequency domain using Eq. 5.1 and compared to network analyzer measurements. The frequency response was constructed using 250 data points over a 12 GHz bandwidth for which the frequency domain measurements were made. The rms error calculated was 1.48 %. The error is comparable to the models generated for the PCB plane, but is visibly more in the plots (Figure 8.9). The rms value does not reflect this because the error is below -20 dB. This translates to an S_{21} magnitude of less than 0.01. The phase is tracked very well, but there is a shift in the magnitude level. This could be due to insufficient sampling interval. The rise time is 15 ps and the minimum time step for measurement is 10 ps. Hence, only 2 or 3 data points model the rise time. This was shown to produce inaccurate results in Section 6.2 for the PCB plane response. The shift of amplitude can be observed for the waveform in Figure 6.2 for a sampling interval of 200 ps. Better results can be expected if the waveform is sampled with finer resolution for the thin film plane.

Table 8.1: Poles and Residues Extracted for the Thin Film Plane

	Real(pole)	Imag(pole)	Real(residue)	Imag(residue)
1	-3.6984714e+00	6.3288621e+01	2.1865741e-01	8.3448558e-03
2	-3.6984714e+00	-6.3288621e+01	2.1865741e-01	-8.3448558e-03
3	-2.5181845e+00	4.5304968e+01	-1.6835780e-01	6.4561855e-02
4	-2.5181845e+00	-4.5304968e+01	-1.6835780e-01	-6.4561855e-02
5	-5.6301370e+00	3.1710468e+01	1.8084266e-02	-3.7642237e-02
6	-5.6301370e+00	-3.1710468e+01	1.8084266e-02	3.7642237e-02
7	-2.1526218e+01	0.0000000e+00	6.0116107e-02	1.5891881e-17
8	-9.2959786e-02	0.0000000e+00	1.7300827e-01	4.6974672e-17
9	-3.7839541e-02	0.0000000e+00	-7.0870955e-02	-3.9998265e-17



(a)



(b)

Figure 8.9 The S_{21} Rational Function Model Response Compared with Network Analyzer Measurements and SONNET Simulation (a) Magnitude (b) Phase

8.3 Rational Function Model vs. Π Model for the Thin Film Plane

For any finite sized plane structure, the step response can be analyzed using the steady state (low frequency) contribution and an initial transient (high frequency) response. Since the planes behave as a capacitor, the steady state TDT response is similar to the charging of a capacitor and can be easily captured using a simple Π model. The Π model developed to capture the steady state response is shown in Figure 8.10, which consists of an inductor (20 pH), two capacitors (0.23 nF) and a resistor (40 m Ω). In Figure 8.10, the capacitance and resistance value is extracted from measurements using a 30 MHz LCR meter, while the inductance value was extracted using FastHenry [76], a tool for modeling and reducing an inductive network. The correlation between the Π model and the TDT response is shown in Figure 8.11 which shows good agreement. The exponential charging of the capacitance between the planes can be clearly seen in the Figure 8.11. The small discrepancy in the final voltage can be attributed to the effect of cables and probes in the set-up. The waveform using the Π model does not however capture the transient response on the planes due to the parallel plate waveguide modes in the structure, as shown in Figure 8.12. In Figure 8.12, an oscillatory waveform expected from the reflections at the plane edges is not seen during the initial time period. Over the initial transition time, the rational function model shows an oscillatory waveform which is absent in the simple Π model as shown in Figure 8.12.

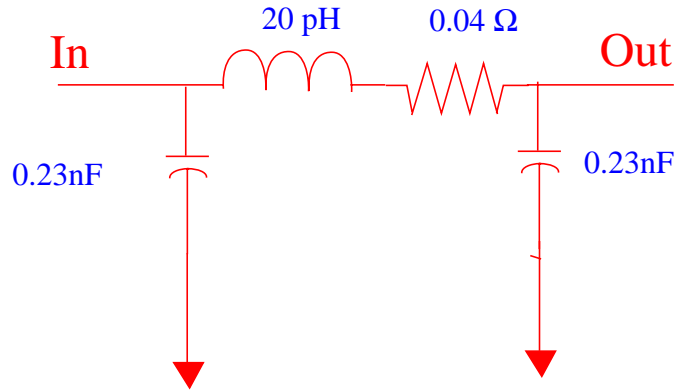


Figure 8.10 Π Model

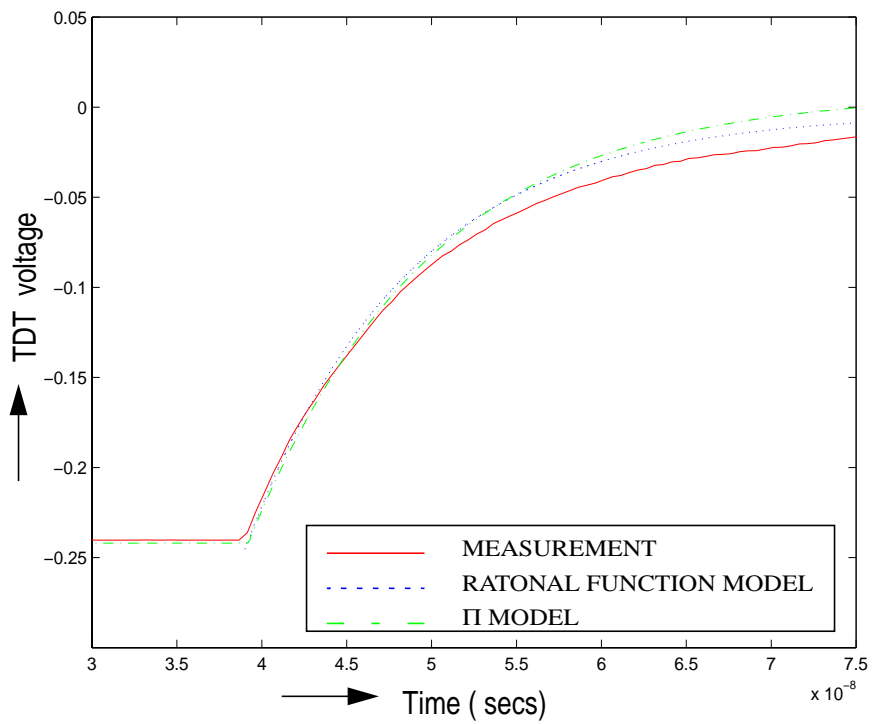


Figure 8.11 Steady State Waveform

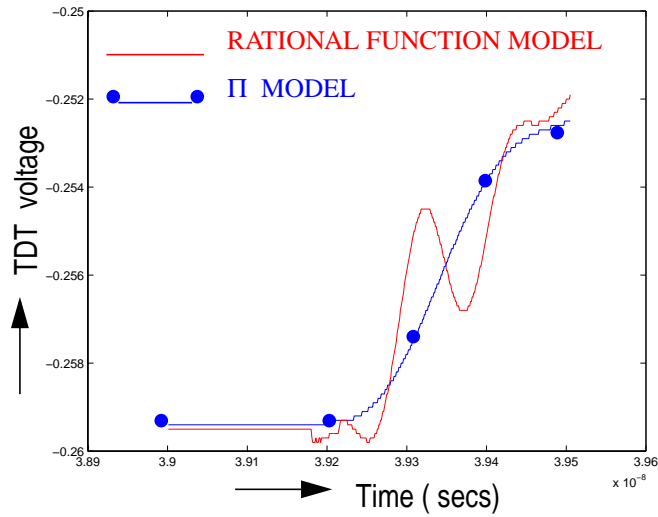


Figure 8.12 Initial Transient

8.4 Measurement to SONNET Based Modeling Correlation

The PCB plane structure analyzed in Chapter IV & Chapter V was quite complex. It had SMA connectors mounted and the exact simulation of this test vehicle was found difficult. The thin film structure in this chapter was designed so that the measurement probes could land directly on the device pads. Hence, the structure did not have any additional connectors and it was possible to analyze the thin film plane in this section using SONNET [72]. The comparison of the measured waveforms and SONNET results are shown in Figure 8.9. There is good correlation and hence this data was used to analyze the rational function models. Compared to the 5.3 " x 5.3 " PCB plane, the 1 cm x 1 cm thin film plane had fewer poles and hence was easier to interpret the behavior.

A macromodel was developed from SONNET data and mapped to the time domain. The method used here to interpolate the response of the device from limited data

in the frequency domain has been discussed in [73]. The method itself is based on the accuracy of the base tool used to generate the required data points for interpolation. However, the macromodeling method is not limited to any particular numerical technique and provides the flexibility of explaining the transient phenomena using the poles and residues of the system. This allows for the easy correlation between the frequency domain response and the time domain response of a system. Analysis of finite sized rectangular planes in both frequency domain and time domain has also been discussed using the radial transmission line approach in [74]. In [74], the time domain response was mapped from the frequency domain results using an inverse fast Fourier transform and was explained by early-time and late-time constituents. The method discussed in this paper uses discrete time convolution on the residues and poles of the system and is hence different from [74].

Using the scattering parameters of the structure, a rational function was developed as follows:

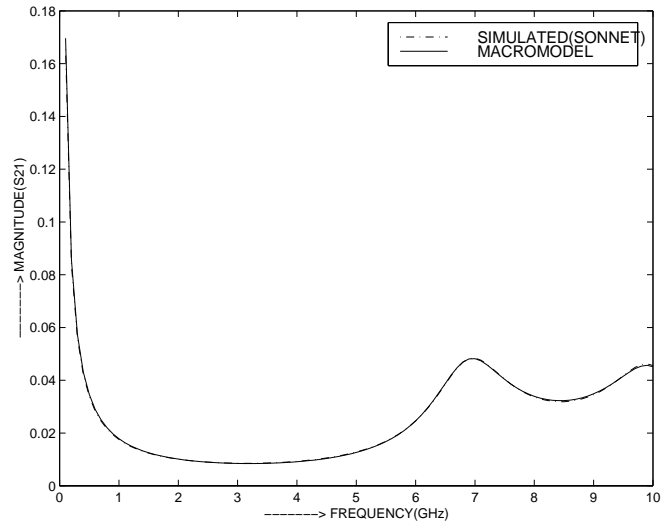
$$\begin{bmatrix} S_{11} & S_{12} \\ S_{21} & S_{22} \end{bmatrix} = \begin{bmatrix} \frac{P_{11} \sum_{m=0}^Q c_m s^m}{\sum_{l=0}^Q b_l s^l} & \frac{P_{12} \sum_{k=0}^Q a_k s^k}{\sum_{l=0}^Q b_l s^l} \\ \frac{P_{21} \sum_{k=0}^Q a_k s^k}{\sum_{l=0}^Q b_l s^l} & \frac{P_{22} \sum_{m=0}^Q c_m s^m}{\sum_{l=0}^Q b_l s^l} \end{bmatrix} \quad (8.1)$$

where a_k, b_l, c_m are real co-efficients, $s = j\omega$, ω is the angular frequency in rad/sec, and P_{ij} ($i, j = 1,2$), and Q are the number of zeros and poles of the system respectively. Through the methods discussed in [73], a macromodel with six dominant poles was generated for the two-port scattering parameters with an error $< 0.1\%$ at each frequency point over the bandwidth of interest. The comparison between the S_{21} macromodel and SONNET is shown Figure 8.13, illustrating the accuracy of the solution. The stability condition was enforced by ensuring that the poles were located in the left half plane. The macromodel for S_{21} is shown Eq. 8.2 for the diagonal port location.

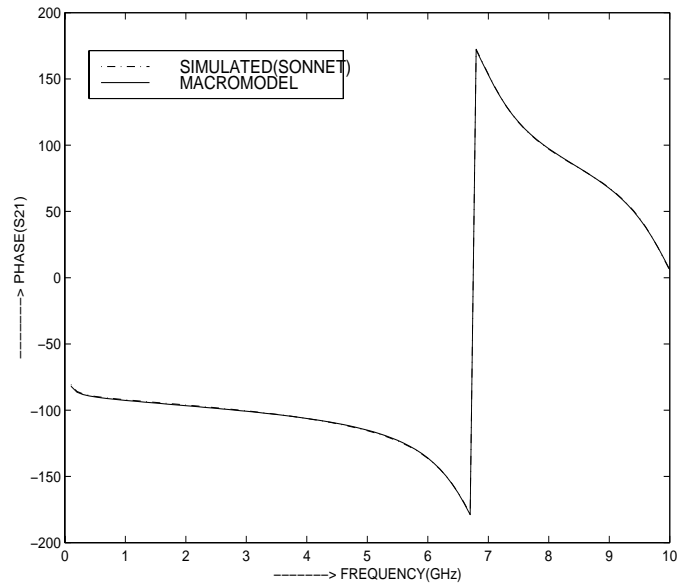
$$S_{21} = \frac{a5.s^5 + a4.s^4 + a3.s^3 + a2.s^2 + a1.s + a0}{b6.s^6 + b5.s^5 + b4.s^4 + b3.s^3 + b2.s^2 + b1.s + b0} \quad (8.2)$$

where the co-efficients are

$a0=-0.00626534108258$	$a1= 0.00020324218090e-10$	$a2= 0.00011305340219e-20$
$a3= 0.00001412270854e-30$	$a4=-0.00001009691451e-40$	$a5= 0.00000064453671e-50$
$b0=-0.00590543473013$	$b1=-0.57706299461047e-10$	$b2=-0.04162416425753e-20$
$b3=-0.04618843424632e-30$	$b4=-0.00159608576925e-40$	$b5=-0.00078450196943e-50$
$b6=-0.00000444070533e-60$		



(a)



(b)

Figure 8.13 S_{21} Macromodel Comparison with SONNET Simulation
 (a) Magnitude (b) Phase

Macromodels for the plane structure shown in Figure 8.2 were developed for two port locations namely

- * Diagonal, where the input and output ports were located along the diagonal corners and
- * Edge, where the input and output ports were located at the corners along the edge.

Then transient waveforms were constructed as outlined in Section 4.4. Figure 8.14 & Figure 8.15 show the correlation between the macromodels using the discrete convolution equation and measurements for both diagonal and edge port locations.

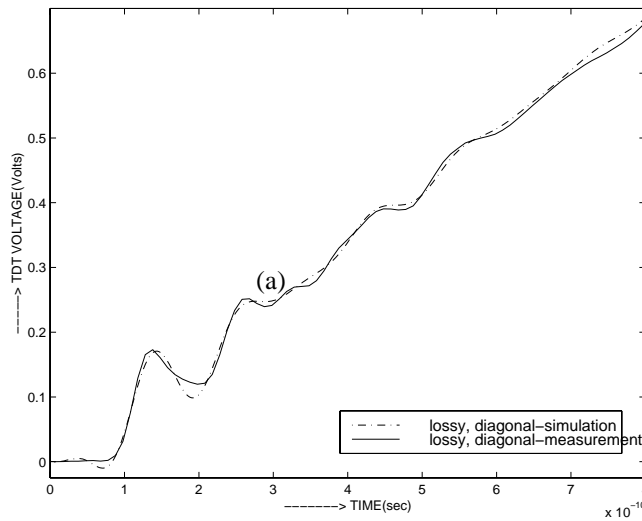


Figure 8.14 TDT Measurement and Simulation Comparison of the Transient Response for the Diagonal Port Location

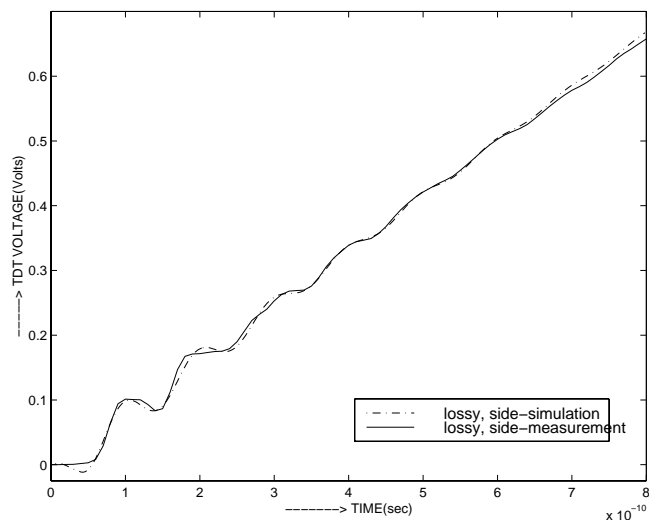


Figure 8.15 TDT Measurement and Simulation Comparison of the Transient Response for the Edge Port Location

As can be seen in the figure, the agreement between the measured and simulated response is very good suggesting that the reflections from the interfaces is minimal. The time period of the oscillation depends on the effective distance between the probe points and the effect of the reflections from the edges of the finite plane structure. In Figure 8.14 and Figure 8.15, the transient response (amplitude & phase) is a function of the position of the probe points suggesting the importance of resonance in the structure. The resonant frequencies for the various test cases have been tabulated in Table 8.2.

Table 8.2: Resonant Frequencies for the Various Test Cases

	Lossy diagonal	Lossy side	Lossless diagonal
Resonant frequency from SONNET	6.8 GHz	9.88 GHz	7.03 GHz
Resonant frequency due to first pole	6.8468 GHz (Dominant)	6.8575 GHz (Not Dominant)	7.0235 GHz (Dominant)
----- Second pole	----- 10.009 GHz (Dominant)	----- 10.057 GHz (Dominant)	----- 10.1955 GHz (Dominant)
Time period from TDT measurement	~ 145 ps	~ 105 ps	-
Resonant frequency from TDT measurement	~ 6.89 GHz	~ 9.53 GHz	-

8.4.1 Analysis Using the System Poles and Residues

An attempt has been made in this section to analyze the pole frequencies in order to explain the transient phenomena on the planes. A pole is the most common type of singularity and its location in the complex plane with respect to other poles of the system can be used to understand the time domain response of the system [77]. The specifications of the PSPL source were 15 ps rise time and 9 V amplitude. A pulse rise time of 30 ps was estimated in the experimental setup by including the effects of the cable, probes and a through calibration standard, which represents a ~11.5 GHz bandwidth. The macromodel developed for the 10 GHz bandwidth was extrapolated to 12 GHz and was found to agree with SONNET scattering parameter data. Hence the

macromodel has the required bandwidth to explain the transient phenomena.

The first test case considers the pulse propagation diagonally across the 1 cm x 1 cm planes. The pole-residue form of the rational function developed is given in Eq. 8.3. The imaginary part of the complex conjugate pairs for poles 2 and 3 correspond to oscillatory expressions in the time domain and the corresponding frequencies are 6.8468 and 10.0099 GHz. The real part of the poles introduce damping in the transient response. Poles 1 and 4 have only an exponential term in the time domain which determines the steady state response. The damping for pole 1 is far greater than pole 4, hence the effect of the latter pole is dominant. The total response corresponding to these poles is found by adding each of the individual components [77].

$$S_{21}(s) = \frac{-1.595}{s + 1749.45} + \frac{0.212 \mp j0.0018}{s + 4.528 \mp j62.894} + \frac{-0.195 \pm j0.00095}{s + 4.001 \mp j43.020} + \frac{0.108}{s + 0.099} \quad (8.3)$$

When analyzing the transient waveform, the input to the system has to be considered. For an ideal impulse case, the poles and residues shown in Eq. 8.3 are sufficient to predict the behavior. To include the ramp input, a transfer function was developed for the input source and convolved with the rational function developed for the structure. The new set of poles and residues were extracted. The poles remained the same as the previous case with the additional poles due to the input. This assumption is valid for no pole cancellation and was checked for this case. The initial time period of the waveform is

therefore a combination of the cosine components corresponding to the complex conjugate pole pairs 2 & 3. This is shown in Table 8.2 where the measured resonance is ~6.89 GHz.

For the second test case, the structure was probed along one side of the structure, the distance between the two ports being ~1 cm. Poles and residues were calculated as before and a macromodel developed. The frequencies corresponding to the complex conjugate poles were 6.8575 GHz and 10.0570 GHz. There was only a slight change in these frequencies compared to the previous case. However, the magnitude of the residues (~0.0008) corresponding to the 6.8575 GHz poles was less than the magnitude of the residues (~0.02) corresponding to the 10.0570 GHz by a factor of 100 as shown in Eq. 8.4. The magnitude of the oscillations is much smaller as the magnitude of the residues is much less than the first test case. Hence the time period of the oscillations is dominated by the 10.0575 GHz component. The TDT measurement showed an initial sinusoidal variation with ~100 ps time period which relates to the ~10 GHz pole corresponding to the resonance at 10.01 GHz.

$$S_{21}(s) = \frac{0.363}{s + 1658.87} + \frac{0.017 \mp j0.0052}{s + 3.862 \mp j63.19} + \frac{-0.0001 \pm j0.00082}{s + 3.825 \mp j43.087} + \frac{0.0099}{s + 0.0078} \quad (8.4)$$

The third case was based on simulation using the macromodel for a lossless structure as in a PCB. The dimensions were maintained as in Figure 8.1 with the only difference that

the structure was assumed to be lossless. The position of the ports were the same as the first test case. Rational function model for this case required seven poles for a good approximation and was developed as before. Poles and residues of such a structure are shown in Eq. 8.5.

$$S_{21}(s) = \frac{-1.125}{s + 1526.98} + \frac{0.201 \mp j0.0080}{s + 0.196 \mp j64.06} + \frac{-0.194 \pm j0.0041}{s + 0.193 \mp j44.13} + \frac{2.262}{s + 310.71} + \frac{0.105}{s + 0.01} \quad (8.5)$$

Comparing equations Eq. 8.3 & Eq. 8.5, the imaginary parts of the corresponding poles and the values of the residues are very close. This means that the time period of the oscillation and the slope of the charge should be similar. The interesting thing to observe in this case is that the real parts of the poles, which correspond to the damping factor for sinusoidal oscillations, are very different. These values were less than the lossy case by a factor of 10 which implies that the amplitude and duration of the ringing is relatively large. There are three real poles, but the damping factor due to poles 1 & 5 is far greater than pole 6 (similar to the lossy case). The lossless structure provides an oscillatory response that does not attenuate with time. The comparison of the oscillatory behavior for the three cases discussed in this section is shown in Figure 8.16. The ground bounce for the lossless case has larger amplitude and sustains for a longer time compared to the lossy cases. This is a bottleneck in low voltage and mixed signal systems, since coupling between distant ports on a plane could exist over a large time period in PCB planes.

Hence a small amount of loss in the structure helps to damp resonance.

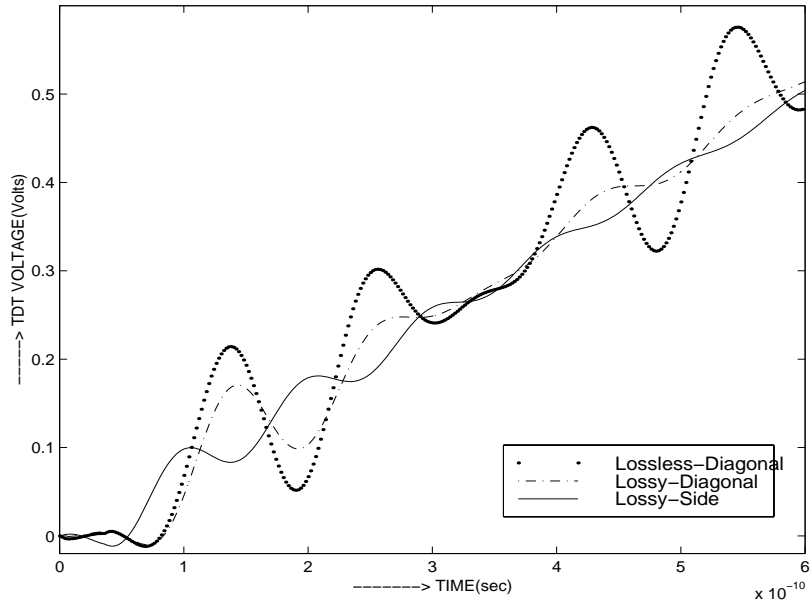


Figure 8.16 Simulation of Ground Bounce for Lossless Test Case Compared with Lossy Test Cases

CHAPTER IX

CONCLUSIONS

The work reported herein was based on characterization of packaging structures using measured data. Two categories of models, namely the low frequency, narrow bandwidth lumped element models and the high frequency, large bandwidth rational function models have been studied. The contributions from the thesis are summarized below:

- (1) The development of a systematic procedure for extracting equivalent circuits for a coupled line system directly from the transient response. These models predict near end and far end crosstalk with less than 10% error.
- (2) A simple method using short-open calibration in time for leaded frame packages has been developed. The originality of this work is the ability to extract electrical models directly from time domain data without the requirement for time-frequency-time transformations.
- (3) The extraction of broad-band frequency domain response from transient data. This method allows the development of rational functions that are compatible with SPICE. Presently, time domain measurements cannot characterize microelectronic devices (in terms of scattering parameters) to the same degree of accuracy as frequency domain measurements. The time domain technique's main handicap is deconvolution. This is due to the ill-conditioning of the deconvolution problem, which allows measurement noise to dominate the solution. A new method for deconvolution has been implemented and this was possible because of the rational function representation of the model.
- (4) The applicability of any method and measurement parameters are dependent on

the test structure. A thorough analysis has been done to quantify error due to the method and the measurement setup.

- (5) A measurement set-up for characterizing the contribution of resonance to ground bounce on lossy thin film planes has been developed. The rational function models developed include the effects of loss in the structure. The ground bounce has been analyzed using macromodels and compared against typical PCB planes. This is a unique contribution as compared to previous work.

9.1 Application of the Rational Function Method

The various methods available for characterizing a device using time domain measurements are discussed in Section 1.6. Each method has been developed to extract different set of parameters and models for a given DUT.

The Short Pulse Technique is the simplest of all and does not involve any type of calibration. Time windowing is used to eliminate any unwanted reflections. This method has been successfully applied to extract propagation constant up to 70 GHz, using a pair of identical lines of different length. This method removes the effect of the measurement accessories like cable, probe contact etc., by using identical lines and is possible because of the form of Eq. 1.3 for the required parameters. Same formulation cannot be used to extract models or scattering parameter data for complex structures such as planes.

The Dynamic Deconvolution method is advantageous for constructing equivalent circuits for electrically small devices. The extraction of the impedance and admittance profile as well as the development of lumped as well as hybrid models can be completely automated. The main disadvantage of this method is that the models do not incorporate any loss. The distributed and hybrid models developed for electrically large devices

become cumbersome and time consuming when integrated into SPICE-like simulators.

Frequency Domain Mapping method has been the most successful of all the characterization methods for modeling the device response in the frequency domain. This is also referred to as time domain network analysis in the literature. Calibration is done in frequency domain using two port error model. The disadvantage of this method is that, at least three standards are required for calibration. The final result is the frequency domain response and does not result in equivalent circuits. If equivalent circuits are needed, the extraction procedure is similar to using the network analyzer measurements.

Exponential approximation method is the closest to the rational function approach used in this thesis. The main advantage of these two methods is that, a model is extracted which can be mapped to either the time domain or frequency domain. The disadvantage of the exponential approximation method discussed in Section 1.6.4 is that, the deconvolution is done in frequency domain, which requires the use of a very device dependent filter. Another disadvantage is the use of time \rightarrow frequency \rightarrow time translation. The poles and residues are extracted from the time domain response using Prony's method, which is unstable compared to GPOF method used in this work.

The main advantage of using the rational function method developed in this work is the use of recursive deconvolution to remove the effect of the step source, without having to transform the data to frequency domain. This does not involve the time \rightarrow frequency \rightarrow time translation of the data, which reduces the conversion errors. The main advantages and disadvantages of the available time domain characterization methods and the rational function method outlined in this thesis are listed in Table 9.1.

Table 9.1: Comparison of the Time Domain Characterization Methods

Method	Parameters Extracted and Other Details	Calibration	Bandwidth	Effect of noise	Automation
Short Pulse Technique	* Propagation constant	* Not required * Two identical lines of varying length required	* Broad band	* Stable. Dependent on sampling interval. * Nyquist criterion used for calculating FFT	Possible
Dynamic Deconvolution Procedure	* Lumped, distributed and hybrid models * Cannot model loss * Can be used for transient simulation in SPICE	* TDNA two-port calibration * Requires at least three calibration standards * Requires time-> frequency -> time conversion	* Narrow band	* Stable. Dependent on sampling interval. * Nyquist criterion used for calculating FFT	* Possible * Time consuming for electrically large structures
Frequency Domain Mapping	* Scattering parameter data in frequency domain.	* TDNA two-port calibration * Requires at least three calibration standards	* Broad band	* Stable. Dependent on sampling interval. * Nyquist criterion used for calculating FFT	Possible

Method	Parameters Extracted and Other Details	Calibration	Bandwidth	Effect of noise	Automation
Exponential Approximation	<ul style="list-style-type: none"> * Pole-residue model * Can be used for obtaining frequency domain response or transient response 	<ul style="list-style-type: none"> * Deconvolution in frequency domain to remove the effect of source * Requires only one calibration standard * Requires time-> frequency -> time conversion 	* Broad band	* Prony's method used is very sensitive to noise.	<ul style="list-style-type: none"> * Possible * Need to know the filter function in advance
Model Optimization	<ul style="list-style-type: none"> * Lumped, distributed or hybrid models 	* Not required	<ul style="list-style-type: none"> * Narrow band. * Difficult to extract broad band models, but not impossible 	* Stable	<ul style="list-style-type: none"> * Not possible, need an approximate model. * Can be optimized, when the appropriate model is chosen
Rational Function Method	<ul style="list-style-type: none"> * Pole-residue models. * R, L, C models can be developed from the set of poles and residues 	<ul style="list-style-type: none"> * Recursive deconvolution used to remove the effect of source * Requires two calibration standards * Does not require time-> frequency -> time conversion 	Broad band	<ul style="list-style-type: none"> * Sensitive * GPOF method more stable than Prony's method 	Possible

8.5 Future Work

The algorithm developed for extracting the rational function models from TDT/TDR measurements gave accurate results for the low loss PCB planes as well as the lossy thin film plane. These structures had many resonances and were electrically large and are very good test cases. There is a need to characterize other packaging structures such as integrated resistors, inductors and capacitors. This will help quantify the types of devices that can be characterized using the method outlined in this research.

The measurement parameters for the PCB plane were determined in Chapter VI and Chapter VII. Optimum values for time resolution, time window and number of averages were found to be dependent on the DUT. In this work, they were determined for the particular DUT. Some work needs to be done to determine the conditions to be met for classes of structures such as planes, capacitors, inductors, resistors etc. Also sampling interval was limited by the measurement set-up in this research. Some effort in developing the state-of-art equipment for making TDR/TDT measurements is necessary. This will help in characterizing small devices such as embedded passives.

One of the major application of the pole-residue extraction procedure is foreseen in the fault diagnosis area. Testing embedded MCM RF-passives is important for identifying manufacturing process related problems to help process debugging and repair. S-Parameter based methods using rational function models were used in the fault diagnosis method and sensitivity analysis in [78]. In [78], it was assumed that the rational function models for S_{11} were available and the test procedure outlined in Figure 8.17 was

verified using simulated data.

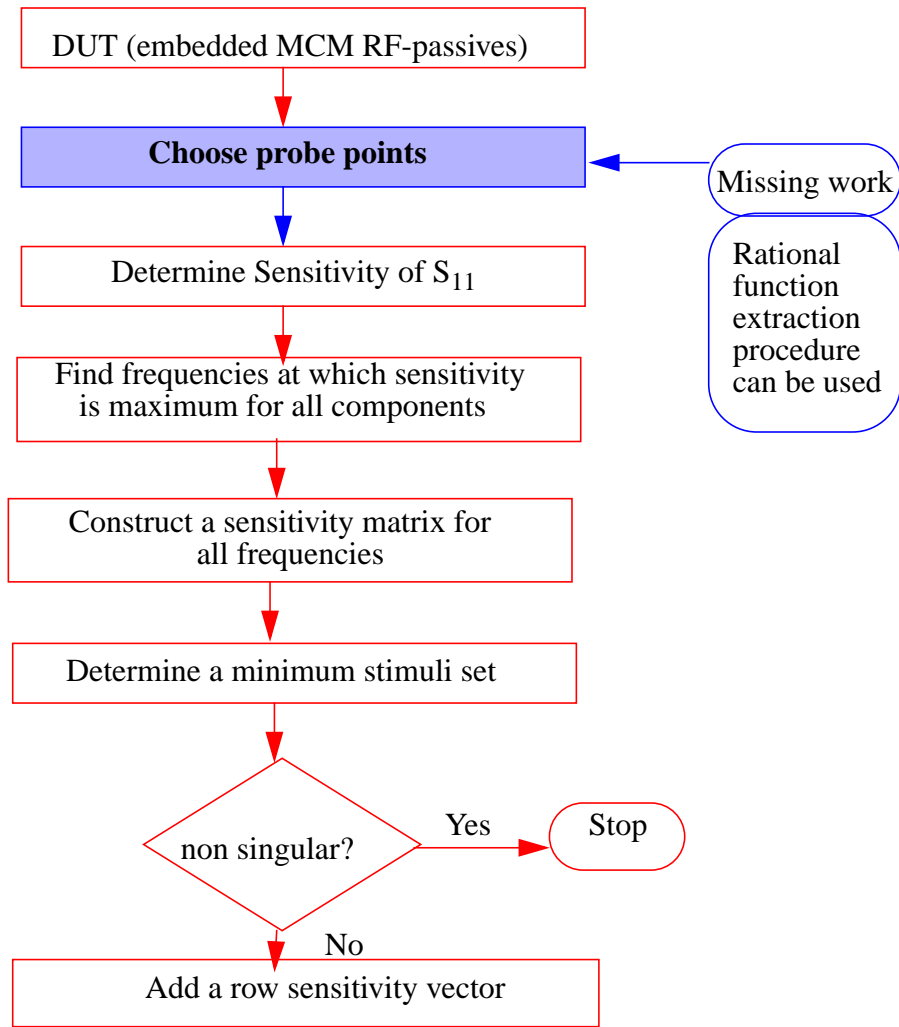


Figure 8.17 Methodology for Parametric Fault Diagnosis [78]

The algorithm outlined in Chapter V can be used to complete the test procedure shown in Figure 8.17. The method outlined in [78] for S-Parameter based fault diagnosis can be combined with the work in this thesis to study the testing procedure using experimental data.

REFERENCES

- [1] R. B. Marks, D. C. DeGroot, and J. A. Jargon, "High-Speed Interconnection Characterization using Time Domain Network Analysis", *Advancing Microelectronics*, Vol. 22, No. 6, Nov/Dec. 1995.
- [2] L. A. Hayden and V. K. Tripathi, "Calibration Methods for time Domain Network Analysis", *IEEE Trans. on Microwave Theory and Techniques*, Vol. 41, No. 3, pp. 415-420, Mar. 1993.
- [3] D. C. Degroot and R. B. Marks, "Optimizing Time-Domain Network Analysis", 46th ARFTG Conference Digest, Nov. 1995, pp. 19-28.
- [4] L. Martens, "High-Frequency Characterization of Electronic Packaging", Kluwer Academic Publishers, 1998.
- [5] A. M. Nicolson, "Broad-Band Microwave Transmission Characteristics from a Single Measurement of the Transient Response", *IEEE Trans. on Instrumentation and Measurement*, Vol. IM-17, No. 4, pp. 395-402, Dec. 1968.
- [6] A. E. Bailey, "Microwave Measurements", Peter peregrinus Ltd., 1989.
- [7] Zhi-Yuan Shen, "New Time Domain Reflectometry Techniques suitable for Testing Microwave and Millimeter Wave Circuits", *IEEE Microwave Theory and Techniques Symposium Digest*, 1990, pp. 1045-1048.
- [8] R. Y. Yu, M. Kamegawa, M. Case, M. Rodwell, and J. Franklin, "A 2.3-ps Time Domain Reflectometer for Millimeter-Wave Network Analysis", *IEEE Microwave and Guided Wave Letters*, Vol.1, No. 11, pp. 334-336, Nov. 1991.
- [9] E. K. Miller, *Time Domain Measurements in Electromagnetics*, Van Nostrand Reinhold press, 1986.
- [10] J. M. Jong, V.K. Tripathi and B. Janko, "Equivalent Circuit Modeling of Interconnects from the Time Domain Measurements", *IEEE Trans. on Components, Hybrids, and Manufacturing Technology*, Vol. 16, No. 1, pp. 119-126, Feb. 1993.
- [11] A. Deutsch, G. Arjavalingham, G. V. Kopcsay, and M. J. Degerstrom, "Short-Pulse Propagation Technique for Characterizing Resistive Package Interconnections", *IEEE Trans. on Components, Packaging, and Manufacturing Technology*, Vol. 15, No. 6, pp. 1034-1037, Dec. 1992.

- [12] A. Deutsch, M. R. Scheuermann, G. Arjavalingam, L. Kneller, J. K. Tam, and C. W. Surovic, "Characterization of Resistive Transmission Lines to 70 GHz with Ultrafast Optoelectronics", *IEEE Microwave and Guided Wave Letters*, Vol. 3, No. 3, pp. 75-77, Mar. 1993.
- [13] A. Tripathi, and V. K. Tripathi, "Characterization of Multiconductor Coupled Lines from Multiport TDR Measurements", *IEEE MTT-S Digest*, 1997, pp. 1777-1780.
- [14] Jyh-Ming Jong, B. Janko and V. K. Tripathi, "Time-Domain Characterization and Circuit Modeling of a Multilayer Ceramic Package", *IEEE Trans. on Components, Packaging, and Manufacturing Technology - Part B*, Vol. 19, No1, Feb. 1996.
- [15] L. A. Hayden, R. B. Marks and J. B. Rettig, "Accuracy and Repeatability in Time Domain Network Analysis", *44th ARFTG Conference Digest*, pp. 39-46, Dec. 1994.
- [16] P. Ferrari, G. Angenieux, B. Flechet, "A Complete Calibration Procedure for Time Domain Network Analyzers", *IEEE MTT-S Digest*, 1992, pp. 1451-1454.
- [17] T. Dhaene, L. Martens, and D. De Zutter, "Calibration and Normalization of Time Domain Network Analyzer Measurements", *IEEE Trans. on Microwave Theory and Techniques*, Vol. 42, No. 4, pp. 580-589, Apr 1994.
- [18] M. Sipila, K. Lehtinen, and V. Porra, "High-Frequency Periodic Time-Domain Waveform Measurement System", *IEEE Trans. on Microwave Theory and Techniques*, Vol. 36, No. 10, pp. 1397-1405, Oct 1988.
- [19] R. B. Marks, L. A. Hayden, J. A. Jargon, and F. Williams, "Time Domain Network Analysis using the Multiline TRL Calibration", *Automatic RF Techniques Group conference*, Dec. 1994, pp. 47-55.
- [20] W. Su, and S. M. Riad, "Calibration of Time Domain Network Analyzers", *IEEE Trans. on Instrumentation and Measurement*, Vol. 42, No. 2, pp. 157-161, Apr 1993.
- [21] W. R. Scott, Jr., and G. S. Smith, "Error Corrections for an Automated Time-Domain Network Analyzer", *IEEE Trans. on Instrumentation and Measurement*, Vol. IM-35, No. 3, pp. 300-304, Sept. 1986.
- [22] D. Rytting, "Overview of Component and Device Characterization", *Materials Research Society Symposium Proceedings*, Vol. 430, 1996, pp. 219-228.
- [23] Hermann-Josef Eul, and B. Scheik, "A Generalized Theory and New Calibration Procedures for Network Analyzer Self-Calibration", *IEEE Trans. on Microwave Theory and Techniques*, Vol. 39, No. 4, pp. 724-731, Apr 1991.

- [24] A. J. Estin, J.R. Juroshek, R. B. Marks, F. R. Clague and J. Wayde Allen, "Basic RF and Microwave Measurements: a Review of Selected Programs", *Metrologia*, Vol. 29, pp. 135-151, 1992.
- [25] R. B. Marks and D. F. Williams, "Electrical Characterization Methods for High-Speed Interconnections", *The International Journal of Microcircuits and Electronic Packaging*, Vol. 18, No. 3, pp. 207-216, 1995.
- [26] M. B. Steer, S. B. Goldberg, G. Rinne, P. D. Franzon, I. Turlik and J. S. Kasten, "Introducing the Through-Line Deembedding Procedure", *IEEE MTT-S Digest*, Vol. 3, 1992, pp. 1455-1458.
- [27] S. D. Corey and A. T. Yang, "Interconnect Characterization Using Time Domain Reflectometry", *IEEE Trans. on Microwave Theory and Techniques*, Vol. 43, No. 9, pp. 2151-2156, Sept. 1995.
- [28] S. D. Corey, K. J. Kerns and A. T. Yang, "Automatic Measurement-Based Characterization of Lossy MCM Line Using Lumped Elements", *IEEE Topical Meeting on Electrical Performance of Electronic Packaging*, 1996, pp. 144-146.
- [29] A. J. Poggio, M. L. Van Blaricum, E. Miller and R. Mittra, "Evaluation of a Processing Technique for Transient Data", *IEEE Trans. on Antenna and Propagation*, Vol. 26, No. 1, pp. 165-173, Feb. 1978.
- [30] M. L. Van Blaricum and R. Mittra, "Problems and Solutions Associated with Prony's Method for Processing Transient Data", *IEEE Trans. on Antenna and Propagation*, Vol. 26, No. 1, pp. 174-182, Jan. 1978.
- [31] J. C. Toscano, A. E. Riad, S. M. Riad, and A. Y. Al-Mazroo, "Wide-Band Characterization of Multilayer Thick Film Structures Using a Time-Domain Technique", *IEEE Trans. on Instrumentation and Measurement*, Vol. IM-38, No. 2, pp. 515-520, Mar. 1989.
- [32] M. Ahmad, S. M. Riad, Aicha A. R. Riad, and W. A. Davis, "Characterization and Modeling of Thick-Film Components for Hybrid Microwave-Integrated Circuits", *IEEE Trans. on Instrumentation and Measurement*, Vol. IM-34, No. 4, pp. 564-569, Mar. 1985.
- [33] S. Sercu, and L. Martens, "A New Approach for the Experimental Circuit Modeling of Coupled Interconnections Based on Causality", *IEEE Trans. on Microwave Theory and Techniques*, Vol. 45, No. 10, pp. 1977-1981, Oct. 1997.

- [34] S. Pannala, C. Ngyuen and M. Swaminathan, "Extraction of Electrical Parameters of High Density Connectors using Time Domain Measurements", Proceedings of the Electronic Components and Technology Conference, 1997, pp. 936-941.
- [35] S. Pannala, A. Haridass and M. Swaminathan, "Parameter Extraction and Electrical Characterization of High Density Connector using Time Domain Measurements", IEEE Trans. on Components, Packaging and Manufacturing Technology - Advanced Packaging, Vol. 22, No. 1, pp. 32-39, Feb. 1999.
- [36] R. T. Kollipara, J. Williams and V. K. Tripathi, "Characterization of RF-IC Packages by Multiport Excitation", International Microwave Symposium Digest, 1996, pp. 1727-1729.
- [37] H. Katzier, R. Reischl, P. Pagnin, "SPICE-Models for high-pincount board connectors", IEEE Trans. on Components, Packaging & Manufacturing Tech. Part-B: Advanced Packaging, vol. 19, pp. 3-6, Feb. 1996.
- [38] J. M. Jong and V. K. Tripathi, "Time Domain Characterization of Interconnect Discontinuities in High-Speed Circuits", IEEE Trans. on Components, Hybrids, and Manufacturing Technology, Vol. 15, No. 4, pp. 497-504, Aug. 1992.
- [39] J. Mosley, A.L. Garza, "Compass Connector: Bringing Together all of the Important Attributes of a Connector", Panda Project Internal Report.
- [40] A. Haridass, C. Nguyen and M. Swaminathan, "Electrical Characterization of High Speed Connector for High Frequency Applications", Proceedings of INTERPack Conference, EEP-Vol. 19-1, Jun. 1997, pp. 483-488.
- [41] H. Johnson and M. Graham, "High-Speed Digital Design, A handbook of Black Magic", Prentice Hall, 1993.
- [42] J. R. Andrews, "TDR, Step Response & "S" Parameter Measurements in Time Domain", Application Note, AN-4, Picosecond Pulse Labs, May 1989.
- [43] A. Feller, H. R. Kaupp, and J. J. Digiacomia, "Crosstalk and Reflections in High Speed Digital Systems", AFIPS conf. Proc. Fall Jt Computer Conf., 1965, pp. 511-525.
- [44] M. Sengupta, Steve Lipa, Paul Franzon and Michael Steer, "Crosstalk Driven Routing Advice", Proceedings of 47th Electronic Components and Technology Conference, 1994, pp. 687-694.

- [45] R. E. Matick, "Transmission Lines for Digital and Communication Networks", IEEE Press 1995, Ch. 5, pp. 170-172.
- [46] S. Pannala, M. Swaminathan, M. Nachnani, "Characterization of RF-IC Packages Using Time Domain Measurements", Internal Report, Oct. 15, 1998.
- [47] K. L. Choi and M. Swaminathan, "Synthesis of RF Circuits for Embedded Passive Components in Mixed Signal Applications", 48th Electronic Components and Technology Conference, 1998, pp. 1052-1060.
- [48] S. Pannala, J. Bandyopadhyay and M. Swaminathan, M. Torres, L. Smith, X. Yuan and G. Fitzgerald, "Contribution of Resonance to Ground Bounce in Lossy Thin Film Planes", 7th Tropical meeting on Electrical Performance of Electronic Packaging, Oct. 1998, pp. 185-188.
- [49] N. Na, S. Dalmia and M. Swaminathan, "S-parameter based Macromodeling of Resonance in High Speed Packages", Presented at the 16th General Assembly of the International Union of Radio Science, Jan. 14, 1999.
- [50] Tak K. Tang and Michel S. Nakhla, "Analysis of High-Speed VLSI Interconnects Using the Asymptotic Waveform Evaluation Technique", IEEE Trans. on Computer-Aided Design, Vol. II, No. 3, pp 341-352, Mar. 1992.
- [51] M. Celik, O. Ocali, M. A. Tan and A. Atalar, "Pole-Zero Computation in Microwave Circuits Using Multipoint Pade Approximation", IEEE Trans. on Circuits and Systems-I, Vol. 42, No. 1, pp. 6-13, Jan. 1995.
- [52] E. Chiprout and M. S. Nakhla, "Analysis of Interconnect Networks Using Complex Frequency Hopping (CFH)", IEEE Trans. on Computer-aided Design of Integrated circuits and Systems, Vol. 14, No. 2, pp. 186-200, Feb. 1995.
- [53] R. S. Adve, T. K. Sarkar, S. M. Rao, E. K. Miller and D. R. Pflug, "Application of the Cauchy Method for Extrapolating/ Interpolating Narrow-Band System Responses", IEEE Trans. on Microwave Theory and techniques, Vol. 45, No. 5, pp. 837-845, May 1997.
- [54] J. H. McClellan, C. S. Burns, A. V. Oppenheim, T. W. Parks, R. W. Schafer, H. W. Schuessler, "Computer-Based Exercises for Signal Processing using MATLAB", Prentice Hall, 1998.
- [55] R. Kumaresan, "Estimating the Parameters of Exponentially Damped or Undamped Sinusoidal Signals in Noise", Ph. D Dissertation, University of Rhode Island, 1982.

- [56] Y. Yua, "On Techniques for Estimating Parameters of Exponentially Damped/Undamped Sinsusoids in Noise", Ph. D. Dissertation, Syracuse University, 1988.
- [57] Y. Hua and T. K. Sarkar, "Generalised Pencil-of-Function Method for Extracting Poles of an EM System from its Transient Response", IEEE Trans. on Antenna and Propagation, Vol. 37, No. 2, pp. 229-234, Feb. 1989.
- [58] S. Lin and E. S. Kuh, "Transient Simulation of Lossy Interconnects Based on the Recursive Convolution Formulation", IEEE Transaction on Circuits and Systems-I, Vol. 39, No. 11, pp. 879-892, Nov. 1992.
- [59] W. T. Beyene and J. E. Schutt-Aine, "Interconnect Simulation Using Order Reduction and Scattering Parameters", Proc. 48th Electronic Components Tech. Conf., 1998, pp. 627-631.
- [60] F. B. Hilderbrand, "Introduction to Numerical Analysis", Second Edition, Tata McGraw-Hill, 1974.
- [61] J. Rahman and T. K. Sarkar, "Deconvolution and total Least Squares in Finding the Impulse Response of an Electromagnetic system from Measured data", IEEE Trans. on Antennas and Propagation, Vol. 43, No. 4, pp. 416-421, Apr. 1995.
- [62] T. K. Sarkar, F. I. Tseng, S. M. Rao, S. A. Dianat, and B. Z. Hollmann, "Deconvolution of Impulse Response from Time-Limited Input and Output: Theory and Experiment", IEEE Transaction on Instrumentation and Measurement, Vol. IM-34, No. 4, Dec. 1985.
- [63] N. Na and M. Swaminathan, "Modeling and Transient Simulation of Planes in Electronic Packages for GHz Systems", Submitted to 8th Tropical meeting on Electrical Performance of Electronic Packaging, 1999.
- [64] D. C. DeGroot and J.A. Jargon, "Long Term Stability in a Calibrated Time-Domain Network Analyzer", Presented at the Measurement Science Conference, Pasadena, CA, Feb. 4-6, 1998.
- [65] S. M. Kay, "Autoregressive Spectral Analysis of Narrowband Processes in White Noise with Application to Sonar Signals", Ph. D Dissertation, Georgia Tech., 1980.
- [66] H. M. Cronson and P. G. Mitchell, "Time Domain Measurements of Microwave Components", IEEE Trans. on Instrumentation and Measurement, Vol. IM-22, pp. 320-325, 1973.

- [67] W. L. Gans, "Calibration and Error Analysis of a Picosecond Pulse Waveform Measurement System at NBS", Proceedings of the IEEE, Vol. 74, No. 1, pp. 86-90, Jan. 1986.
- [68] Tektronix 11801B Digital Sampling Oscilloscope User Manual, 1993.
- [69] Tektronix SD-24 TDR/ Sampling Head User Manual, 1993.
- [70] J. M. Jong, V. Tripathi, B.Janko, "Modeling and Simulation of Switching Noise with the Associated Package Resonance for High Speed Digital Circuits", 45th Electronic Components and Technology Conference, 1995, pp. 323-328.
- [71] S. Pannala, J. Bandyopadhyay, M. Swaminathan, "Contribution of resonance to ground bounce in lossy thin film planes", IEEE Trans. on Components, Packaging and Manufacturing Technology - Advanced Packaging, Aug. 1999.
- [72] SONNET User's Manual, SONNET Software, Inc., Volume I-III, September 1996.
- [73] K. L. Choi, N. Na and M. Swaminathan, "Characterization of embedded passives using LTCC technology", IEEE Trans. on Components, Packaging, and Manufacturing Technology, Part B: Advanced Packaging, Vol. 21 No. 3, pp. 258-268, Aug 1998.
- [74] J. C. Parker, "Via Coupling within Parallel Rectangular Planes", IEEE Trans. on Electromagnetic Compatibility, Vol. 39, No. 1, pp. 17-23, Feb. 1997.
- [75] P. Chahal, R.R. Tummala, M. G. Allen, and Madhavan Swaminathan, "A Novel Integrated Decoupling Capacitor for MCM-L Technology", Proc. of 46th Electronic Components and Technology Conf., 1996, pp. 125-132.
- [76] FastHenry User's Guide, Version 3, Nov. 1996.
- [77] M. E. Van Valkenburg, "Network Analysis", Third edition, Prentice Hall, 1986.
- [78] H. Yoon, J. Hou, A. Chatterjee, and M. Swaminathan, "Fault Detection and Automated Fault Diagnosis for Embedded Integrated Electrical Passives", IEEE International Conference on Computer Design: VLSI in Computers and Processors, 1998, pp. 588-593.